Anisotropic Potential Energy Surfaces for Atmospheric Gas - Unsaturated Hydrocarbon Molecule Interactions from Differential Scattering Experiments

by

Kip Patrick Stevenson

A dissertation submitted in partial fulfillment of
the requirements for the degree of

Doctor of Philosophy

University of Washington

1997

Approved by 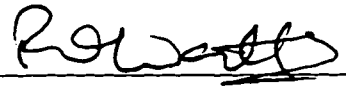

(Chairperson of Supervisory Committee)

Program Authorized
to Offer Degree Department of Chemistry

Date August 15, 1997

In presenting this dissertation in partial fulfillment of the requirements for the Doctoral degree at the University of Washington, I agree that the Library shall make its copies freely available for inspection. I further agree that extensive copying of this dissertation is allowable only for scholarly purposes, consistent with "fair use" as prescribed in the U.S. Copyright Law. Requests for copying or reproduction of this dissertation may be referred to University Microfilms, 1490 Eisenhower Place, P.O. Box 975, Ann Arbor, MI 48106, to whom the author has granted "the right to reproduce and sell (a) copies of the manuscript in microform and/or (b) printed copies of the manuscript made from microform."

Signature Kip Stevenson

Date 8/15/97

University of Washington

Abstract

Anisotropic Potential Energy Surfaces for Atmospheric Gas - Unsaturated Hydrocarbon Molecule Interactions from Differential Scattering Experiments

by Kip Patrick Stevenson

Chairperson of Supervisory Committee

Professor R.O. Watts

Department of Chemistry

The total differential scattering cross sections of several atmospheric gas - unsaturated hydrocarbon molecule systems (He, Ne, Ar, H_2, N_2, CO, and NO with C_2H_2, C_2H_4, C_3H_4, and C_4H_2) were measured using bolometric detection in a crossed-molecular beam apparatus. The observed angular scattering distributions exhibit damped rainbow and diffraction oscillations, providing information on the intermolecular potential energy surface anisotropy of each system. Light reduced-mass systems containing He and H_2 show fast diffraction oscillations, while heavy reduced-mass systems with Ar, N_2, CO, and NO show predominately a single broad rainbow oscillation. The Ne - C_2H_2, C_2H_4, and C_3H_4 systems at high angular resolution show both rainbow and diffraction features.

Anisotropic Lennard-Jones N-6 and Barker model potential energy surfaces were determined for each system by a 'best-fit' comparison between the experimental cross section and a theoretical cross section, calculated using infinite-order-sudden (IOS).

JKWB. and Born approximations. Adjustment of potential parameters ϵ and R_m, expanded in Legendre polynomial functions of the proper molecular rotational symmetry, allowed adequate fits to the experimental data. Barker model potentials provide better descriptions of the collision dynamics due to better estimates of the long-range interactions. In comparision, the Lennard-Jones potentials are consistently more anisotropic in the well region and more steeply repulsive at short-range.

The damped diffraction oscillations were observed to be most sensitive to the potential size anisotropy and rather insensitive to the potential shape anisotropy. The relative size anisotropies for the various systems increase in agreement with the number of $C-C$ bonds along the hydrocarbon's molecular symmetry axis. The damped rainbow oscillations were observed to be sensitive to the potential shape anisotropy and less sensitive to potential size anisotropy. He, Ne, and H_2 - hydrocarbon interactions are found to have isotropic well depths, while the Ar, N_2, NO, and CO - hydrocarbon interactions are anisotropic. The Ar - hydrocarbon systems prefer T-shaped structures. Interestingly, the acetylene-diatom systems have more stable linear configurations, while the ethylene-diatom and allene-diatom systems prefer T-shaped geometries. The IOS results need to be compared with more accurate close-coupled quantum scattering calculations to determine the contributions of rotational inelastic transitions.

TABLE OF CONTENTS

LIST OF FIGURES

LIST OF TABLES

ACKNOWLEDGMENTS

I would like to express my sincere thanks to the many people who provided assistance and support during the tenure of this thesis. First and foremost, much appreciation is extended to Professor R. O. Watts for his guidance and his generosity in allowing me to complete part of this work at the University of Melbourne in Melbourne, Australia.

Many thanks is also offered to the various Watts group members who have engaged in enlightening discussions of science and other intangible subjects that have contributed to the completion of this Ph.D. I would like to thank Dr. John Close, Dr. Pedro Muiño, and Dr. Adi Scheidemann for their scientific mentorship and experimental assistance over the years. Past and present group members: Dr. Aijun Li, Dr. Shao-Hui Tseng, Dr. Jian Wu, Dr. Doug Beck, and Susan Rempe are acknowledged for their support and comradery. A special thanks goes to Dr. Moonbong Yang for his help with the scattering codes.

Finally, much heart-felt gratitude is offered to my family and friends for their continual encouragement and their participation in the many extracurricular events that have enriched my life outside of science. Many thanks is offered to Dr. Pat Heath and Dr. Jeff Delrow for their support. I am especially grateful for the friendship of my brothers, Kern, Kraig, Keith, Brad, and Barry; the love and support of my parents, Sharon and Donn Adams; and the inspiration of my dear grandmother, Mrs. Ruth Forrey.

Chapter 1

INTRODUCTION

1.1 Introduction to Intermolecular Forces

The investigation of intermolecular forces is pervasive throughout physics, chemistry, and biology. Knowledge of the microscopic interactions that occur between molecules is essential for the fundamental understanding of many chemical and physical phenomena such as the macroscopic thermodynamic properties of bulk gases, liquids [59], and solids [103], the kinetic rates of chemical reactions [73] and energy transfer processes [69], and the structure and dynamics of small molecular clusters [84, 89, 37]. The diffusivity, viscosity, and thermal conductivity of bulk phase systems are largely determined by the detailed interactions between molecules under non-equilibrium conditions. The rates of intermolecular energy transfer and relaxation depend primarily on the forces exerted by particles during collision events. Van der Waals cluster complexes are characterized by large amplitude, anharmonic motions which depend sensitively on the size and shape of potential energy barriers and the coupling of bending and stretching motions. The intermolecular forces that occur during the interaction of molecules originate from the combination of short range repulsive and long range attractive forces. The repulsive forces arise from the overlap of molecular wave functions at small distances. Due to the Pauli exclusion principle, the electron density in the overlap region is reduced and the positively charged nuclei are improperly sheilded. Both effects give rise to exponetially decaying replusion at short range.

The long range forces are comprised of electrostatic, induction, and dispersion contributions. Electrostatic forces result from the interaction of the permanent multipole moments of the molecules, which arise from the electrical charge distributions inherent in the molecules. The induction and dispersion forces are due to polarization forces that occur when the electronic cloud distribution of one molecule is distorted by the electric field due to an adjacent molecule. The induction forces result from the ability of the permanent multipole moments of one molecule to induce instantaneous dipole, quadrupole, and higher order moments, while the dispersion forces arise primarily from the mutual polarization of interacting molecules, giving rise to attractive induced dipole-induced dipole and induced dipole-induced quadrupole moment interactions.

For neutral nonpolar molecules in their electronic ground states, dispersion forces are the dominant contribution to the total interaction at long range. Therefore, the electrostatic and induction forces are usually neglected, or included only when highly accurate descriptions are required. At moderate temperatures and pressures the properties of liquids, solids and gases can be explained in great detail from knowledge of the dispersion forces that occur during the interaction of neutral, stable molecules. As a result of the success of this approach in explaining the behavior the real gases, the dispersion forces are commonly referred to as van der Waals forces [74].

Van der Waals forces are conveniently represented in terms of the intermolecular potential, or van der Waals potential energy surface when multiple degrees of freedom are important. For closed-shell atomic interactions, the potential energy is isotropic and depends only upon the relative intermolecular separation between atoms. However, for atom-molecule and molecule-molecule interactions, the potential energy surface is anisotropic and depends not only upon the relative separation but also on the relative orientation of the interacting bodies. In general, the interaction potential for a fixed orientation is repulsive at short intermolecular separations and attractive at large intermolecular distances. Due to the balance of repulsive and at-

tractive forces, a stable equilibrium geometry, r_m, with a minimum potential energy, ϵ, exists at intermediate separations. For anisotropic interaction potentials, the parameters, r_m and ϵ, are orientation dependent, and their relative magnitudes as a function of orientation represent the size and shape anisotropy of the potential energy surface, respectively. The presence of anisotropy in the potential energy surface leads to more complicated structural and dynamical properties of van der Waals interactions. Further, knowledge of the anisotropic contributions to the intermolecular forces plays an important role in understanding properties of large molecular systems found in atmospheric, astrophysical, and biological media.

Van der Waals interaction potentials have been determined from several theoretical and experimental methods. *Ab initio* quantum chemical methods have been applied using only knowledge of the number of electrons and nuclei to calculate the potential over various intermolecular ranges [119, 118]. However, for systems with more than a few electrons, approximations must be imposed to make the calculation tractable, and in many cases, accurate determination of the potential energy surface over the full intermolecular range is precluded. For the larger systems, *ab initio* methods are most accurate at describing the repulsive contributions to the intermolecular potential at short range, where electronic exchange between interacting molecular orbitals leads to significant interaction energies. At intermediate and large intermolecular distances, basis set size, energy corrections, electron correlation effects become important considerations and higher level accuracy is needed to determine relatively small interaction energies.

Perturbation theoretical methods have also been applied to determine the long range part of the potential energy surface [74, 64, 51]. For molecules separated by distances much larger than their molecular dimensions, the potential may be treated as a perturbation to the total energy. Multipolar expansion of the interaction potential allows the determination of the second order energy contributions, which yield the attractive induction and dispersion contributions to the interaction at long range.

From the assumption of combination rules [31, 59] and the application of molecular polarizabilities and ionization potentials, the dispersion series coefficients for a particular interaction may be estimated to a reasonable degree of accuracy.

Experimental measurements of thermophysical properties such as the bulk transport properties of diffusion, thermal conductivity, and viscosity, provide information primarily on the repulsive potential [74, 64]. Since these properties are averaged over broad energy distributions and all intermolecular orientations, they are considered less sensitive methods for determining complete interaction potentials. Second virial coefficients are more sensitive to the form of the interaction potential, but experimental data is usually only obtained over narrow temperature ranges, precluding determination of the full potential. However, thermophysical data can be used as a constraint when determining potentials from more accurate methods, especially if only the isotropic part of the potential is desired.

Intermolecular potentials have been most accurately determined from spectroscopic and scattering methods in combination with molecular beam techniques. Molecular beams when expanded into vacuum allow for the preparation of rotationally and vibrationally cold molecules and clusters that may be investigated under collision-free conditions. Spectroscopic methods usually entail the interrogation of bimolecular clusters with infra-red (IR) or microwave radiation. Near-IR spectroscopic studies [83, 90] probe the dissociation spectra of clusters by excitation of the high frequency modes of the monomer components in the cluster. The determination of rotationally-vibrationally resolved IR spectra provide information on the structural properties of the cluster around the attractive global minimum of the potential energy surface. Further, the IR predissociation linewidths may provide information about the dissociation of clusters under "half-collision" conditions. Far-IR spectroscopic experiments [37, 106] directly probe the van der Waals stretching and bending modes, yielding detailed information about attractive potential energy surface in the well region. For anisotropic systems in particular, far-IR studies probe the rotational-vibrational tun-

neling and the barriers to internal rotation of monomer subunits in the complex [36].

Microwave spectra mostly provide structural information through the determination of dimer rotational constants, although approximate estimates of the bending and stretching force constants of complexes may also be obtained by simple analysis of the distortion constants [45]. Unfortunately, microwave studies are most amenable to investigation of polar molecules or strongly interacting van der Waals molecules, since complexes must have strong transition dipoles in order to yield observable rotational line spectra.

Scattering methods can provide information on even the most weakly interacting systems over the full potential energy surface by tuning the relative collision energy between intersecting molecular beams [101, 44]. The measurement of the total attenuation of one molecular beam due to the presence another crossed beam, provides the integral scattering cross section, which is most sensitive to the attractive or long range part of the potential energy surface. The integral scattering cross section measured as a function of the relative energy can reveal glory oscillations which afford a measure of the product of ϵ and r_m potential parameters. Anisotropy in the potential energy surface leads to damping of the glory oscillations. In some cases, the relative anisotropy in a given potential energy surface can be determined by the measurement of integral scattering cross sections of molecules in various stages of alignment [131, 129, 130].

Total differential scattering measurements can provide more complete information about the potential energy surface over the complete intermolecular range depending on the relative collision energy and the measured angular range of scattering [24]. At low collision energies, small angle scattering is dominated by the attractive part of the potential energy, while at high collision energies, scattering to large angles probes the repulsive contributions. Moderate collision energies, simultaneously probe both the attractive and repulsive contributions of the potential energy surface for small and large deflection angles, respectively.

For measurements with high energy and angular resolution, quantum interference features are resolved in the differential scattering cross section. Light reduced-mass systems exhibit fast diffractive oscillations, where the angular spacing of these high frequency oscillations yields a direct measure of the size parameter r_m. Heavy reduced-mass systems reveal slow rainbow oscillations, where the angular position of this low frequency oscillation provides a measure of the interaction strength, or well depth, ϵ. Medium reduced-mass systems may show both interference features, yielding a more complete determination of the of the size and shape of the potential energy surface. The presence of anisotropy in the potential energy surface leads to damping of the observed oscillatory features in comparison to isotropic systems. The damping of the fast diffractive oscillations primarily provides a measure of the size anisotropy, Δr_m, while the broadening and damping of the slow rainbow oscillation is more sensitive to the shape anisotropy, $\Delta\epsilon$[1].

The most detailed information about anisotropic potentials can be determined from the state resolved scattering experiments. Separation of elastic and inelastic scattering contributions is important for determining the isotropic and anisotropic contributions to the intermolecular potential. Differential energy loss scattering methods can determine the state-to-state scattering cross sections by resolving individual internal state transitions [25]. The observation of rotational rainbows, even when only partially resolved, reveal information about the relative anisotropy in the repulsive part of the potential in particular. The most detailed information is provided by the combination of laser spectroscopic methods and scattering techniques [122, 107, 91] but is only applicable to a few model systems. The preparation and selection of reactant and product state distributions under single collision conditions, makes possible a complete detailed understanding of anisotropic potential energy surfaces of larger

[1] A measure of the relative anisotropy in atom-cylindrical molecule systems can be characterized by the difference between the parallel and perpendicular orientations with respect to the molecular symmetry axis. $\Delta r_m = r_{m,\parallel} - r_{m,\perp}$ and $\Delta\epsilon = \epsilon_\parallel - \epsilon_\perp$.

molecular systems.

Some caution is necessary when considering the determination of potentials from only one set of empirical data. Each experimental method has inherent sensitivities to particular parts of the intermolecular potential, and therefore no one particular data set is convenient for a unique determination of the potential energy surface for a given system. To remove the possibility of any unnecessary bias in fitting experimental data with a given potential model, it is important to consider other experiments which provide complimentary information about the potential energy surface. In the best case scenario, both theoretical calculations and experimental measurements should be combined in the analysis to ensure the uniqueness of the potential energy surface over the full intermolecular range. Nevertheless, it remains useful to choose a particular experimental technique that can be applied to a large class of systems, and with consideration of existing complementary data from other theoretical and experimental sources, accurate van der Waals potential energy surfaces for several important molecular systems may be determined.

1.2 Molecular Systems of Interest

This thesis describes the determination of anisotropic potential energy surfaces primarily from total differential scattering experiments. Where relevant, existing experimental and theoretical data for each system is also considered in the analysis of the scattering. In particular, we are interested in the interactions of rare gas atoms (He, Ne, and Ar) and small diatomic molecules (H_2, N_2, CO, and NO) with unsaturated hydrocarbon molecules such as acetylene, C_2H_2, ethylene, C_2H_4, allene, C_3H_4, and diacetylene, C_4H_2.

Investigation of these systems is important for several general and fundamental scientific reasons. Collisions of He and H_2 with small organic molecules are important for understanding the astrophysical observations of interstellar and interplanetary me-

dia [43]. He and H_2 are the most abundant astrophysical gases and their interactions with other molecules cause line broadening, disequilibrium rotational and vibrational state populations, and in some cases, the pumping of maser emissions. Acetylene, ethylene, and diacetylene are important interstellar carbon-based molecules and are commonly found in interplanetary bodies such as Jupiter and Titan [58]. An understanding of the interactions these molecules may be important for modeling the chemical and physical properties of less directly accessible environments.

The interactions of common diatomic gases such as N_2, NO, and CO with hydrocarbon molecules are important for understanding kinetic processes like the rates translational, rotational and vibrational energy transfer, as well as the effects caused by anthropogenic pollutants. Acetylene, ethylene, allene are the abundant feedstocks used in the synthesis of large organic molecules and polymeric materials [110, 113], and their affect when released into the atmosphere are potentially hazardous to the balance of complex environmental conditions. Understanding the collisions of small atmospherically abundant molecules, such as CO, NO, and N_2 with simple organic molecules may also provide a basis for determining important atmospheric chemical reactions and heat transfer processes.

Previous spectroscopic investigations of van der Waals complexes have indicated that systems containing unsaturated bonds have interesting lewis-acid base properties [89], large-amplitude bending and stretching motions [62], and possibly, uniquely shaped potential energy surfaces with several equivalent configurations. The anisotropy in the potential energy surface can lead to difficulties in assigning the observed transition frequencies with "good" quantum numbers, since a complex may range from rigid to free internal rotor dynamics depending on the magnitude of the potential anisotropy in relation to the size of the monomer rotational constant [60]. The coupling of van der Waals stretching and bending modes is due to the detailed shape and size anisotropy and the determination of structural constants in many cases requires averages over boundstate wavefunctions. The presence of equivalent potential

minima with various barriers heights gives rise to internal rotations of molecular subunits and leads to observable tunnel splittings in high resolution spectra [106]. In some cases analyses of spectroscopic data may be aided by considering data from scattering studies, especially for most weakly bound systems such as those containing He, Ne and H_2[86].

The primary motivation for the study of the atmospheric gas - unsaturated hydrocarbon interactions investigated in this thesis is to build on previous work that considered the interaction potentials of larger atom-molecule systems. Yang and coworkers have investigated the scattering of He, H_2, N_2, and Ar from acetylene and were able to developed improved potential energy surfaces by considering complementary data from differential energy loss and high resolution spectroscopic experiments [126, 26, 124]. For the He-C_2H_2 system, the authors showed using IOS and CS quantum analysis of differential scattering and differential energy loss measurements that the He-C_2H_2 potential energy surface is weakly anisotropic and essentially spindle shaped due to presence of the π electrons of the acetylene molecule. Further, Yang also developed reasonable interaction potentials for H_2, N_2, and Ar - C_2H_2 systems using IOS analysis of total differential scattering measurements.

In additional work, Yang was able to develop an improved Barker model potential energy surface for the Ar- C_2H_2 system using more accurate close-coupled quantum calculations and by considering existing spectroscopic data [127]. Not only did the improved potential predict the observed scattering data, it also agreed quite well with the spectroscopic results of the Ar-C_2H_2 complex. Interestingly, Yang showed that long cylindrical molecules might give rise to strong inelastic features at small scattering angles in the total differential scattering cross section: structures corresponding to large Δj rotational transitions as a result of large impact parameter collisions. To test this theoretical prediction, we chose to increase the overall molecular bond length of the hydrocarbon from acetylene to allene to diacetylene, in hopes of observing sharp inelastic features in the total differential scattering cross sections. Further,

to examine the role of the attractive, long-range potential in promoting such rotational transitions, the probes, He, Ne, H_2, N_2, CO, and NO were also selected. Since the polarizability of this series increases from He through NO, we expect to observe an increase in the interaction strength for these systems and possibly changes in the inelastic features if they are indeed caused by large impact parameter collisions.

While the initial aim of the experiments presented in this thesis is to investigate a novel scattering feature, this study also represents the most extensive investigation of intermolecular forces for unsaturated hydrocarbons and their interactions with atmospherically important gases via scattering methods. It is hoped the results found here will provide a complementary set of experimental data that may help in the analysis of spectroscopic investigations of weakly-bound complexes, and aid in the development of theoretical models for larger van der Waals molecules and clusters.

1.3 Structure of Thesis

Figure 1.1 shows the general procedure for obtaining anisotropic potential energy surfaces from crossed-molecular beam experiments. In general, the total differential scattering cross sections exhibit diffraction or rainbow oscillations which provide sensitive measures of the potential energy surface for each system. An experimental scattering cross section for each system of interest is measured and compared to a theoretical scattering cross section that is calculated using quantum scattering theory and an analytic potential energy surface. Potential parameters are initially chosen, taking into account any existing complementary data, and adjusted until a statistically determined "best-fit" is obtained. Once an agreeable potential has been determined, more advanced calculations maybe carried out if desired.

Chapter 2 reports the various experimental methods and the measured total differential scattering cross sections of the several rare gas and small molecule interactions with unsaturated hydrocarbon molecules. Chapter 3 presents the classical, quantal

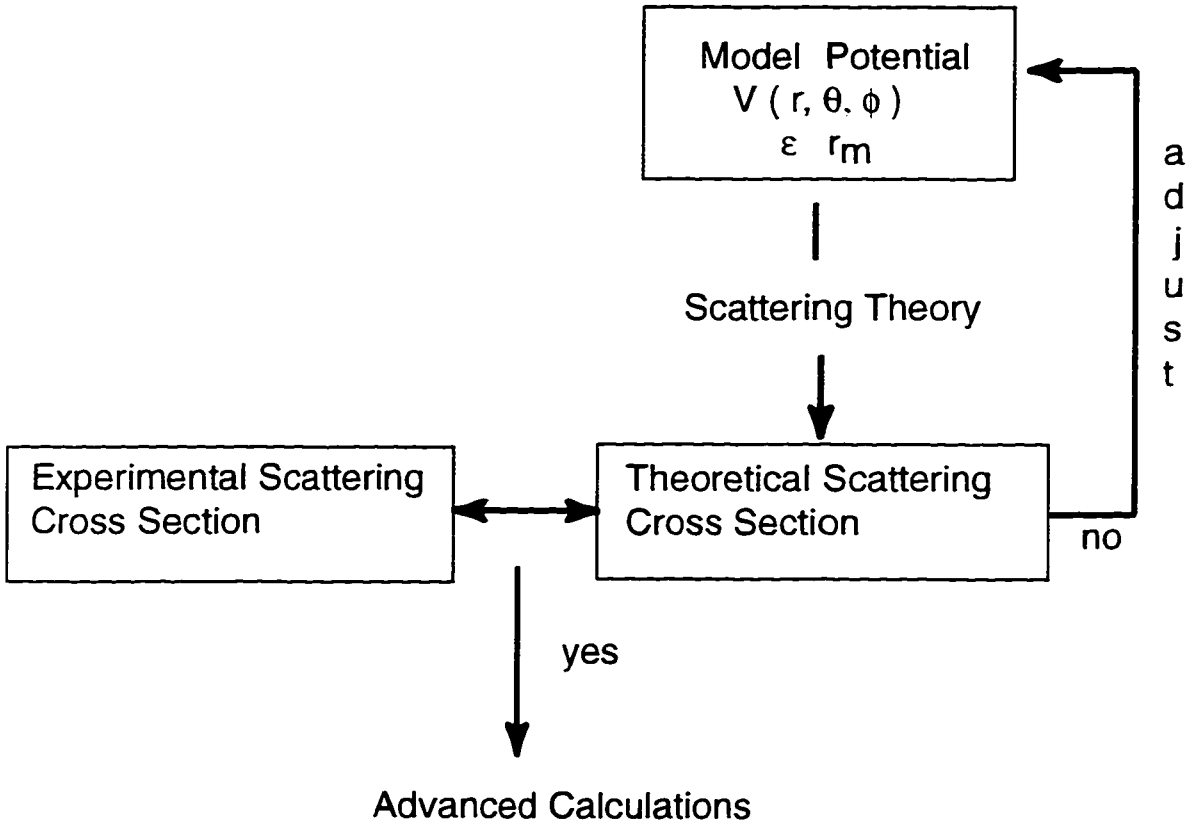

Figure 1.1: Flow diagram for the determination of potential energy surfaces from crossed-molecular beam experiments.

and semi-classical scattering theory necessary for interpreting the scattering results. The orientation dependent model potential energy surfaces used in fitting the experimental cross sections are presented in Chapter 4. The analysis procedures for energy and angular averaging and statistical comparison of cross sections is reported in Chapter 5. Chapter 6 discusses the results of the fitted potential energy surfaces. Finally, Chapter 7 gives some conclusions about the experimental findings as well as suggestions for future work.

Chapter 2

EXPERIMENTAL METHODS

The determination of anisotropic intermolecular potentials via scattering experiments with resolved diffraction and rainbow oscillations, requires special reagent preparation, sophisticated high resolution instrumentation, and the application of sensitive detection techniques. Supersonic jet sources produce well-directed beams of molecules with cold internal state distributions and narrow translational velocity distributions. The intersection of molecular beams in high vacuum ensures well-defined scattering dynamics under single collision conditions, and with the addition of differential pumping stages, background scattering contributions may be significantly reduced. Bolometric detection coupled with phase sensitive lock-in techniques allows for measurement of small scattered fluxes, while mass spectrometric detection of the source gases enables characterization of the supersonic expansions and the determination of the collision energy resolution by time-of-flight (TOF) spectroscopy.

The crossed molecular beam apparatus is explained in Section 2.1. The experimental procedures and the measured total differential scattering cross sections for rare gas (He, Ne, and Ar) and diatomic molecule (H_2, N_2, CO and NO) scattering from unsaturated hydrocarbon molecules (C_2H_2, C_2H_4, C_3H_4, C_4H_2) are presented in Section 2.2. Finally, the TOF analysis of the molecular beams and the determined velocity distributions are given in Section 2.3.

2.1 Molecular Beam Scattering Apparatus

The total differential scattering cross sections were measured using the crossed molecular beam scattering apparatus shown in Figure 2.1. The molecular beam scattering apparatus consists of two molecular beam source chambers located inside a cylindrical stainless steel vacuum chamber with a rotatable base plate and removable top cover plate. The division of source chambers and additional stages of differential pumping reduce the background gas contributions inside the main scattering chamber, where the skimmed molecular beams intersect at 90 degrees on the rotational center of the apparatus. The in-plane angular scattering is detected by rotation of the internal components with respect to the fixed liquid-N_2, liquid-He cooled bolometric detector, which may be placed in one of two positions (A or B) depending on the required angular resolution. A calibrated vernier etched into the top of the base plate allows for angular measurements to be taken at 0.1 degree intervals through a range -3 to 95 degrees. A mass spectrometer allows for source gas characterization and TOF measurements when a rotatable chopper wheel is placed in the bolometer position B. The cylindrical vacuum chamber has dimensions of 475 mm. × 800 mm. × 10 mm. for the height, internal diameter, and wall thickness respectively. The rotatable base plate is 50 mm. thick and contains a 3 mm. high lip which fits inside the inner vacuum chamber. Machined grooves in the base plate allow for a viton o-ring seal between the base plate and the vacuum chamber, as well as a ball bearing trace enabling the rotation of the internal components with respect to the chamber and top plate. Rotation is performed by an electric motor with a chain attached to the outside edge of the base plate.

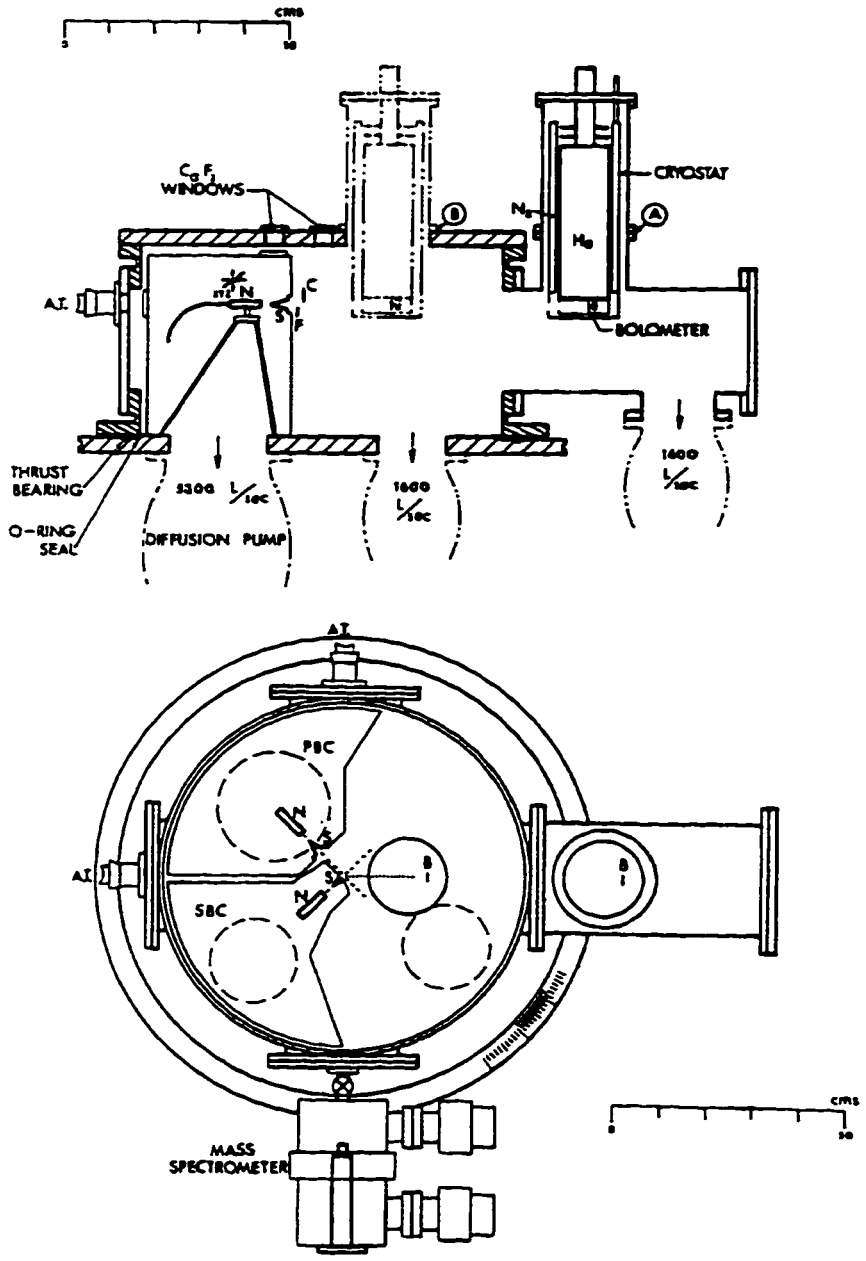

Figure 2.1: In-plane crossed molecular beam apparatus. Bolometer or chopper assembly placed in position B allows for low resolution differential scattering measurements or TOF analysis, respectively. Bolometer placed in position A allows for high resolution scattering measurements and IR spectroscopy.

2.1.1 *High-Vacuum System*

To obtain high vacuum conditions, diffusion pumps are attached via the base plate to the primary, secondary, main and auxiliary internal chambers. The primary source chamber with the higher inlet gas pressures is pumped by a 5300 l/s Varian VHS-10 diffusion pump, while the secondary source chamber with a much lower gas load is pumped with 2400 l/s Varian VHS-6 diffusion pump. The main and auxiliary regions are each pumped with baffled 1600 l/s Varian VHS-6 diffusion pumps. All four diffusion pumps are backed by a mechanical Roots booster pump (Edwards EH-500) in conjunction with a two-stage rotary vacuum pump (Edwards E2M175). The mass spectrometer, which is conveniently separated from the main scattering apparatus by a resealable UHV valve, is pumped by two turbomolecular pumps (Pfieffer TCP300) of 300 l/s and 175 l/s and a small Edwards rotary pump.

All operating pressures were measured using Bayard-Alpert ionization gauges with Perkin Elmer (DGC-III) and Granville-Phillips (GP270) gauge controllers. The mechanical foreline press is monitored with a Varian thermocouple gauge. Typical working pressures for the various chambers were 10^{-4} Torr for the two source chambers, $10^{-7} - 10^{-6}$ Torr for the main scattering chamber, and 50-100 mTorr for the vacuum foreline. The mass spectrometer is usually kept under ultrahigh-vacuum conditions, except when monitoring source gases.

2.1.2 *Supersonic Molecular Beams*

Molecular beams are a common, essential component in the investigation of gas-phase collision dynamics and spectroscopy [82]. A directional beam of molecules is usually created by expanding gas at an equilibrium pressure, P_0, and temperature, T_0, into vacuum via a small, thin aperture or nozzle. The flow properties of the expansion depend on the initial source conditions and the Knudsen number, K_n, or the ratio of the mean-free-path, λ, of the molecules in the nozzle to the nozzle diameter, d [44].

For $K_n > 1$, free molecular flow produces a low flux, effusive beam of molecules with a velocity profile of an equilibrium Maxwell-Boltzmann distribution. However, for $K_n < 1$, hydrodynamic flow produces a supersonic, high flux beam of molecules with a narrowed translational velocity distribution and relaxed internal degrees of freedom. Supersonic sources are more suitable for scattering experiments, since they allow for larger scattering signals, increased directionality, and higher energy resolutions.

The theory of supersonic expansions is well developed in the literature [82, 5, 55, 39]. Molecules emanating from a supersonic nozzle undergo many two and three body collisions which allows conversion of stagnation enthalpy into directed kinetic mass flow. Along a stream line, enthalpy, H_0, is conserved and the general condition for a nonlinear, polyatomic gas [39] is:

$$\begin{aligned} H_0 &= \left(\frac{3}{2} + \frac{3}{2} + 1\right) kT_0 + \int_0^{T_0} C_v(vib)\, dT \\ &= \left(\frac{2}{2} + 1\right) kT_s + \frac{3}{2} kT_{rot} + \int_0^{T_{vib}} C_v(vib)\, dT + \frac{1}{2} mv^2 \end{aligned} \tag{2.1}$$

where the top set of terms is the initial stagnation enthalphy at T_0, and the bottom set of terms represent the expanded, relaxed gas with kinetic energy of the directed mass flow, $1/2\ mv^2$. The final translational, rotational, and vibrational temperatures are T_s, T_{rot}, and T_{vib} respectively and $C_v(vib)$ is the vibrational heat capacity. The actual relaxation of gas depends on the rates of energy transfer between the translational, rotational, and vibrational degrees of freedom during the expansion. Generally, the translational, rotational, and vibrational temperatures follow the order $T_s \leq T_{rot} \leq T_{vib}$,[39] indicating vibrational modes are the least relaxed degrees of freedom. The true internal energy partitioning in the expanded beam must be determined from experimental methods. However, as a rough approximation, it may be assumed that the translational temperature provides a lower bound ($T_s = T_{rot}$) for the rotational temperature of molecules in the expanded molecular beam. This information is important in the analysis of scattering experiments where inelastic features

may be observed, since the total scattering cross sections usually involve an average over initial states in non-state selected experiments.

If an equilibrium between the degrees of freedom is assumed, Equation 2.1 can be rewritten using total heat capacity , C_p [82] to give:

$$C_p(T_0 - T_s) = \frac{1}{2}mv^2 . \tag{2.2}$$

which essentially relates the stream velocity to the stagnation enthalpy of the gas as before, indicating that the terminal velocity depends primarily on the heat capacity of the gas prior to expansion.

The supersonic velocity distribution [5, 82, 44] is usually expressed:

$$f(v)\,dv = Nv^3 \exp\left[\frac{-(v - v_s)^2}{v_w^2}\right] dv \tag{2.3}$$

where N is a normalization factor, v_s is the stream velocity, and v_w is the velocity width. v_s and v_w are more conveniently expressed in terms of the experimental parameters by:

$$v_s = \sqrt{\frac{2kT_0\gamma}{m(\gamma - 1)}} \quad \text{and} \quad v_w = \sqrt{\frac{2kT_s}{m}} \tag{2.4}$$

where k is Boltzmann constant, m mass, and $\gamma = C_p/C_v$ is the heat capacity ratio.

A simple analysis of Equation 2.3 yields the most probable velocity v_{mp} :

$$v_{mp} = \frac{1}{2}\left(v_s + \sqrt{v_s^2 + 6v_w^2}\right) . \tag{2.5}$$

The most probable velocity is convenient for calculating relative collision energies and associated wave vectors for the scattering experiments.

For supersonic beams, the local mach number, M, or the ratio of the stream velocity to the local speed of sound, provides a measure of the beam quality [17, 82]. The Mach number is given by:

$$M = \frac{v_s}{\sqrt{\gamma kT_s/m}} = \left(\frac{2}{\gamma}\right)^{\frac{1}{2}} \frac{v_s}{v_w} . \tag{2.6}$$

Typically mach numbers greater than 10. indicate a good quality beam of high directionality. sufficiently cooled internal states. and narrow velocity distributions.

Using equation 2.2. an estimate of the degree of cooling after the expansion can be expressed as [82]:

$$\frac{T_s}{T_0} = \left[1 + \frac{1}{2}(\gamma - 1) M^2\right]^{-1} . \tag{2.7}$$

For $M > 10$. translational temperatures T_s are on the order of a few Kelvin for room temperature expansions using normal stagnation pressures of approximately 5-10 atmospheres. The high degree of translational cooling from supersonic expansions leads to high energy resolution. which is necessary for resolving interference structure in differential scattering measurements. By control of source stagnation temperatures and pressures. the relative collision energy may be varied considerably (50 meV to 1 eV). providing a powerful tool for studying collision dynamics over the full intermolecular range of the potential energy surface.

The studies in this thesis involve intersection of rare gas and diatomic probe molecules with unsaturated hydrocarbon target at thermal collision energies of approximately 100 meV. In this energy regime. the collsions are mostly elastic at small scattering angles. The colliding molecules are considered to be in their ground electronic and vibrational states with only a few initially populated rigid-rotor states. Rotationally inelastic collisions should be also considered. since the long hydrocarbon molecules have small rotational constants thereby increasing the number of accessible inelastic channels.

2.1.3 Detection

The measurement of scattered intensities requires sensitive detectors and techniques in order to determine small signals above the background gas collisions. Mass spectrometers and cryogenic bolometers are two common detection methods generally used

in differential scattering measurements. Mass spectrometers require many stages of differential pumping in order to increase the sensitivity for detecting small scattered fluxes. Since differential pumping causes space restrictions, mass spectrometers must be placed further from the scattering volume, a condition which affects the signal-to-noise ratio and the angular resolution in an experiment. At the sacrifice of signal, it is sometimes beneficial to position the detector at greater distances to improve the angular resolution in order to resolve high frequency diffraction features in the differential scattering cross section. The positioning of the detector at larger distances from the scattering center also allows for improved time resolution in the detection on inelastic features by energy loss experiments [25]. For the experiments in this thesis, the mass spectrometer serves only as a means to determine the beam quality, concentration of clusters, and the measurement of velocity distributions by TOF analysis.

Cryogenic bolometers [68] have some advantages over mass spectrometers. They are compact, require less differential pumping, and are relatively simple electronically, which allows the bolometer to be placed much closer to the scattering volume. A bolometer is a energy-flux sensitive device which has a negative coefficient of resistance, α, which is defined by:

$$\alpha = \frac{1}{R}\frac{dT}{dR} . \tag{2.8}$$

When cooled to low temperatures, the bolometer resistance increases exponentially and the responsivity of the device becomes very high. Small incident fluxes impinging on the bolometer surface deposit translational energy[1] thereby warming the bolometer and decreasing its resistance. If the bolometer is placed in series with a load resistance and biased with a battery, changes the changes in resistance of the bolometer can be monitored as changes in voltage. Figure 2.2 shows the equivalent electrical schematic of the bolometer circuit.

[1] For non-sticking molecules. For adsorbed molecules, the heat of condensation per molecule also needs to be considered.

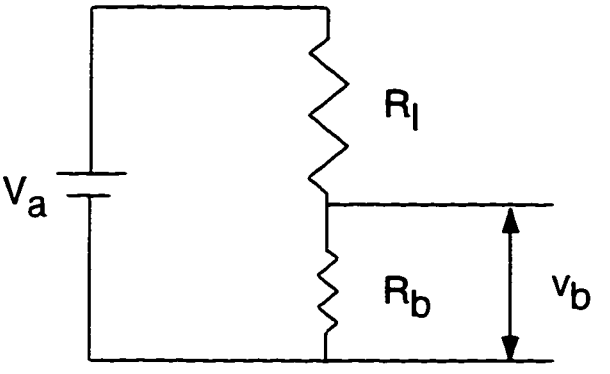

Figure 2.2: Bolometer electrical circuit. V_a is bias voltage. R_l is the load resistance. R_b is the bolometer resistance, and V_b the output signal voltage.

The bolometer output voltage, V_b, due to the applied bias voltage, V_a, is given by:

$$V_b = \frac{R_b}{R_b(T) + R_l} V_a \tag{2.9}$$

where $R_b(T)$ and R_l are the bolometer and load resistances, respectively.

Figure 2.1 shows the actual liquid-He, liquid-N_2 cryostat that provides the low temperature heat bath for sensitive operation of the bolometer. The bolometer is mounted onto a copper block in thermal contact with the liquid-He dewar and protected from background radiation by a series of shields and apertures. Operating temperatures of approximately 1.7 K are obtained by pumping on liquid-He through its λ point transition with a two-stage rotary pump. For a 9 V. bias battery voltage and 10 MΩ load resistor, 1-2 microamps of current corresponds to a few volts of output signal at constant beam flux.

The bolometer responsivity and noise characteristics can be determined by measuring the current-voltage (I-V) response curve[2]. The responsivity, $S(0)$, at the operating point was determined to be 3.1×10^5 V/W. The defining noise characteristic

[2]For a description see references [21, 121, 68]

of the bolometer is given by the noise-equivalent power, NEP, which is the lowest signal voltage equivalent to the voltage noise to give a signal to noise ratio of unity at unity bandwidth [85]. The NEP is defined by :

$$NEP = \frac{V_{noise}}{S(0)} \tag{2.10}$$

where V_{noise} is the voltage noise and $S(0)$ is the responsivity. For $V_{noise} = 5.0$ nV at 1.7 K, the NEP of the bolometer was determined to be 1.6×10^{-14} W / $\sqrt{Hz}$, which corresponds to a lower limit detection sensitivity of approximately 10^5 to 10^6 molecules/s under typical beam flux and operating conditions.

A tremendous improvement in the signal-to-noise ratio is gained by modulation of the molecular beams and application of phase-sensitive lock-in detection techniques [85, 116]. AC signals are easier to amplify and the use of a modulated reference signal in combination with low-pass filtering has the advantage of decreasing the noise bandwidth considerably. Phase-sensitive lock-in detection essentially multiplies the bolometer signal voltage with a reference signal generated from modulation of the secondary beam with a 50% chopper. The bolometer voltage is given by $V_b \sin(\omega_b t + \theta_{sig})$ and the reference signal is $V_r \sin(\omega_r + \theta_{ref})$. The multiplication of the two AC voltages by the phase sensitive detection [116] gives:

$$\begin{aligned} V_{psd} &= V_b V_r \sin(\omega_b t + \theta_{sig}) \sin(\omega_r t + \theta_{ref}) \\ &= \frac{1}{2} V_b V_r \cos([\omega_b - \omega_r] t + \theta_{sig} - \theta_{ref}) \\ &\quad - \frac{1}{2} V_b V_r \cos([\omega_b + \omega_r] t + \theta_{sig} + \theta_{ref}) \ . \end{aligned} \tag{2.11}$$

The phase sensitive detection gives two signals at the difference and sum frequencies, respectively. The sum frequency signal is removed by low-pass filtering, and the difference signal yields a DC voltage proportional the amplitude of the bolometer voltage. Since bolometer and references are at the same frequency, $\omega_b = \omega_r$. Equation

2.11 can be expressed as:

$$V_{psd} = \frac{1}{2} V_b V_r \cos(\theta_{sig} - \theta_{ref}) \ . \qquad (2.12)$$

A matching of the signal and reference phases, θ_{sig} and θ_{ref}, repectively, gives an optimal DC signal which can be integrated using standard data acquisition techniques.

2.2 Total Differential Scattering Experiments

2.2.1 Procedure

The total differential scattering cross sections of the rare gases and diatomic molecules with acetylene, ethylene, allene, diacetylene were measured using the experimental setup shown in Figure 2.3. Primary-probe and secondary-target molecular beams are generated in separate differentially pumped source chambers, skimmed, and intersect at 90 degrees on the rotational axis of the scattering apparatus. Fifty-percent modulation of the secondary target gas provides a reference signal for the phase sensitive lock-in detection of the scattered probe flux. The angular position of the detector, or lab angle, is determined from the primary probe beam direction, which has a second collimating skimmer to allow for improved angular resolution. The He cooled bolometer collects the scattered flux and the signal is amplified near the source and differentially supplied to the lock-in. The demodulated analog DC signal is then digitally converted and integrated using a small personal computer to give sufficient signal-to-noise. A controllable beam flag is used to block the probe beam to correct for changing background gas contributions to the detected scattered flux. Modulation of the target beam inside the secondary chamber changes the background gas loading in the main scattering chamber at the reference frequency and thus contributes to the measured signal. The signal intensity at a chosen reference angle is periodically remeasured and used to renormalize the scattered signal to correct for changes in detector sensitivity and beam conditions over the course of the experiment.

The experimental procedure for measuring the total differential scattering cross sections therefore requires the determination of four quantities for each angular data point. The signal intensity at a given position of the detector, $I(\theta)$ may be expressed as:

$$I(\theta) = \frac{I_{sig}(\theta) - I_{bg}(\theta)}{I_{sig}(\theta_{ref}) - I_{bg}(\theta_{ref})} \tag{2.13}$$

where $I_{sig}(\theta)$ is the measured scattered flux at a given angle. $I_{bg}(\theta)$ is the background contribution to the scattered flux at the same lab angle. $I_{sig}(\theta_{ref})$ is the scattered signal intensity at the reference angle, and $I_{bg}(\theta_{ref})$ is the background contribution to the scattered signal at the reference angle.

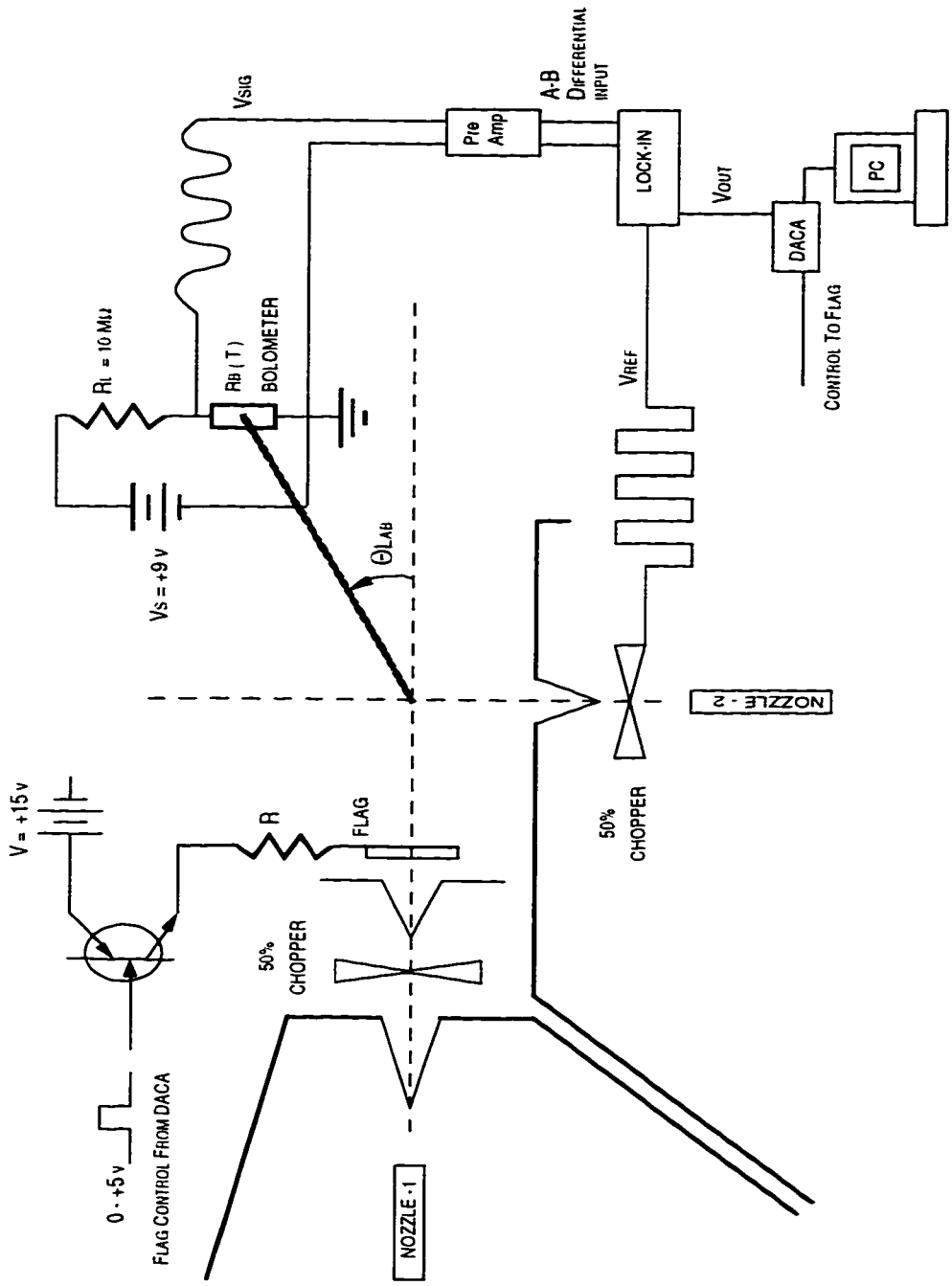

Figure 2.3: Experimental setup for total differential scattering measurements.

2.2.2 *Source Gas Preparation and Diacetylene Synthesis*

Source gases He, Ne, Ar, H_2, N_2, NO, CO, C_2H_2, and C_2H_4 of at least 99% purity were obtained commercially from various vendors. The less common hydrocarbon gas, allene, was purchased from PCR, Inc. at 97% purity. Diacetylene gas was synthesized according to procedure outlined by Armitage et. al[7] as follows. Small gram quantities of C_4H_2 were synthesized by the dropwise addition of 40% sodium hydroxide to 1-4 dichcloro-2-butyne (Aldrich) dissolved in research grade ethanol. Evolved C_4H_2 gas was captured in stream of flowing He gas, bubbled through a 13% NaOH solution, dried with $CaCl_2$, and finally, condensed in a glass trap at liquid-N_2 temperatures.

Purification of the diacetylene was carried out by vacuum distillation using various organic solvent-dry ice baths and several pump-freeze cycles. Observed vapor pressures at the distillation temperatures, measured using a crude thermocouple gauge, agreed roughly with published thermophysical data [115]. The isolation of the diacetylene gas was confirmed using FTIR analysis of low gas pressure samples (10-30 Torr) in a NaCl cell. The FTIR spectrum of a isolated diacetylene is shown in Figure 2.1. The observed transition frequencies at $\tilde{\nu} = 3330,\ 2020,\ 1240$, and 630 cm^{-1} agree well with previously published IR spectra [63, 112]. Mass spectrometric analysis using electron impact ionization showed predominate mass peaks at 50, 49, and 25 amu, respectively. The relative MS intensities were accordance with published mass spectral reference data [1]. From these analyses, the overall purity of the diacetylene gas was estimated at about 90%. Diacetylene is unstable and known to decompose violently [113], therefore samples were stored at dry-ice temperatures until experiments were performed.

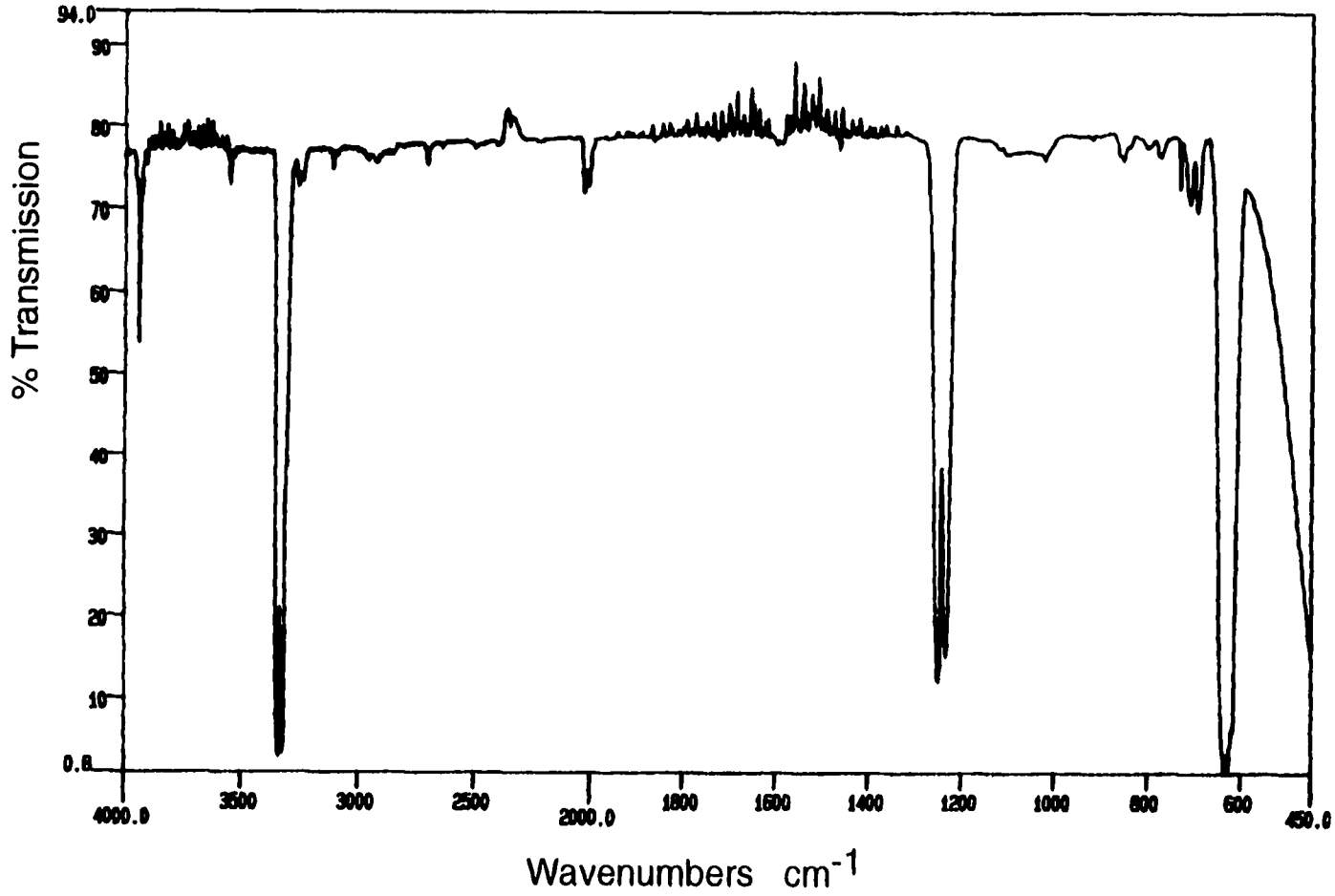

Figure 2.4: FTIR spectrum of C_4H_2 gas sample at 18 Torr in NaCl cell. Transitions at $\tilde{\nu} = 3330$ and $2020\ cm^{-1}$ are the $C-H$ stretch and the triple $C-C$ bond stretch, respectively. $\tilde{\nu} = 630\ cm^{-1}$ is the low frequency $C-H$ bend transition. The other transitions correspond to combination bands.

2.2.3 *Scattering Systems*

This section reports the total differential scattering cross sections of twenty-one systems. The He and H_2 scattering results are presented in Tables 2.1-2.3 and Tables 2.4-2.6. Tables 2.7-2.13 show the results for Ne scattering at both low and high angular resolutions. The Ar results are presented in Tables 2.14-2.16. The results for N_2, CO, and NO scattering are given in Tables 2.17-2.18, 2.19-2.21, and 2.22-2.24, respectively. For each experiment an almost identical procedure was followed:

1. Stable high vacuum conditions were established and the bolometer was cooled to approximately 2 K. After about 2 hours of pumping, the bolometer was allowed to reach an equilibrium voltage condition under no gas load.

2. The primary and secondary beam stagnation pressures were adjusted to give sufficient signal while taking care to prevent both the overloading of diffusion pumps and the condensation of the molecular beams. The vacuum conditions were allowed to reach a steady-state as monitored by stabilization of the working background pressures in each of the differentially pumped chambers.

3. The detector angle was adjusted to the reference lab angle and the lock-in signal was optimized by matching the phases of the chopper reference and scattering signals. The voltage noise was minimized by adjusting the reference frequency (approximately $37Hz$), the lock-in time constant (1-3 s.), and the pre-, post-, and line-filters. For most experiments approximately $50\mu V$ of signal and $100nV$ of noise were measured at the reference angle.

4. The sensitivity of the lock-in was chosen to maximize the DC output on the DACA board over the range of lab angles measured. At the beginning of the experiment, the signal at the reference angle was continuously remeasured until three consecutive measurements agreed to within one standard deviation.

5. The detector was positioned at a given scattering angle and the unflagged, $I_{sig}(\theta)$, and flagged, $I_{bg}(\theta)$, signals were recorded. Each data point involved approx. 2-8 minutes of averaging depending on the scattering angle. In general, angular points were determined from 2 - 30 degrees in various degree intervals. Anywhere from 30 to 60 experimental data points were measured for each scattering cross section.

6. Every fourth data point, the detector was repositioned at the reference angle and the renormalization signal in the unflagged, $I_{sig}(\theta_{ref})$, and flagged, $I_{bg}(\theta_{ref})$, configurations were measured to correct for changes in beam intensities and bolometer sensitivity. A linear interpolation procedure was used to correct the angular data points that were measured between reference points. In general, the renormalization signal varied by no more than 5-10% over the 10-12 hour duration of an experimental run. In experiments with the more condensible gases, the bolometer sensitivity seemed to change most significantly at large angles, probably as a result of the coating of the bolometer surface by probe and target particles.

To determine the operating parameters of the molecular beam apparatus and to test the experimental procedures, the He-Ar differential scattering cross section was measured. The He-Ar results are an essential component of our analysis procedure and will be discussed later in Chapter 5. Further, to check the consistency of our methods, the total differential scattering cross sections of He-C_2H_2 and Ar-C_2H_2 were reproduced in accordance with previous experiments performed in our lab by Yang [126, 127]. Many other experimental tests were performed to check the sensitivity of the bolometer, the effects of background gas loading, the signal averaging techniques, and the overall stability of experimental conditions. We estimate the uncertainties in cross sections to be around 5 and 10 percent at small and large angles, respectively.

Table 2.1: Helium - Ethylene scattering data.

θ	$I(\theta)$	θ	$I(\theta)$	θ	$I(\theta)$	θ	$I(\theta)$
2.8	1450.0	6.8	140.3	11.3	39.1	16.8	16.3
3.3	942.4	7.3	137.1	11.8	30.0	17.3	16.9
3.8	654.1	7.8	106.4	12.3	23.0	17.8	16.9
4.3	446.7	8.3	67.1	12.8	19.3	18.3	16.9
4.8	243.4	8.8	39.4	13.3	18.8	18.8	17.1
5.3	134.4	9.2	28.0	13.8	20.0	19.8	16.9
5.6	103.3	9.3	27.4	14.3	21.1	20.8	16.2
5.7	99.7	9.4	28.0	14.8	21.1	21.8	15.4
5.8	100.0	9.8	30.5	15.3	19.4	22.8	15.8
5.9	101.1	10.3	39.4	15.8	18.3	23.8	15.6
6.3	118.6	10.8	43.3	16.3	17.4	24.8	14.6

Table 2.2: Helium - Allene scattering data.

θ	$I(\theta)$	θ	$I(\theta)$	θ	$I(\theta)$	θ	$I(\theta)$
4.0	363.2	9.8	24.0	13.8	11.1	18.8	10.6
4.3	301.3	10.3	21.3	14.1	10.7	19.3	10.4
4.8	195.7	10.5	20.8	14.3	10.6	19.8	10.8
5.3	131.3	10.7	20.5	14.5	11.1	20.3	11.0
5.8	100.0	10.8	20.6	14.8	11.9	20.8	10.5
6.3	92.2	11.0	20.7	15.3	12.7	21.3	10.5
6.8	87.4	11.3	20.4	15.8	12.4	21.8	10.3
7.3	77.5	11.8	20.6	16.3	11.7	22.3	10.5
7.8	61.8	12.3	19.5	16.8	10.9	22.8	10.1
8.3	48.4	12.8	16.3	17.3	10.6	23.8	9.6
8.8	37.0	13.3	13.1	17.8	10.2	24.8	9.4
9.3	29.2	13.6	11.9	18.3	10.2		

Table 2.3: Helium - Diacetylene scattering data.

θ	$I(\theta)$	θ	$I(\theta)$	θ	$I(\theta)$	θ	$I(\theta)$
3.9	353.5	8.9	44.2	13.9	12.0	18.9	10.5
4.4	282.9	9.4	31.3	14.4	11.3	19.4	10.6
4.9	202.7	9.9	22.8	14.9	11.1	19.9	10.7
5.4	141.2	10.4	19.8	15.4	12.1	20.9	10.2
5.9	100.0	10.9	20.7	15.9	12.1	21.9	9.4
6.4	80.8	11.4	21.7	16.4	12.1	22.9	9.7
6.9	73.7	11.9	21.9	16.9	11.6	23.9	9.5
7.4	70.7	12.4	20.4	17.4	11.1	24.9	9.5
7.9	65.8	12.9	17.0	17.9	10.5		
8.4	56.7	13.4	13.8	18.4	10.0		

Table 2.4: Hydrogen - Ethylene scattering data.

θ	$I(\theta)$	θ	$I(\theta)$	θ	$I(\theta)$	θ	$I(\theta)$
2.8	5196.3	8.8	192.4	15.3	66.9	22.8	19.9
3.3	2878.1	9.3	215.3	15.8	60.8	23.3	18.1
3.6	2113.2	9.8	234.9	16.3	51.4	23.8	18.2
3.8	1624.0	10.3	232.0	16.8	40.0	24.3	18.5
4.3	1176.4	10.8	204.7	17.3	31.3	24.8	18.8
4.8	1082.0	11.3	160.9	17.8	24.7	25.3	19.1
5.3	1076.4	11.8	115.2	18.3	25.6	25.8	21.4
5.8	1000.0	12.3	75.2	18.8	27.2	26.3	16.8
6.3	829.7	12.8	54.1	19.3	28.6	26.8	17.6
6.8	606.6	13.0	47.7	19.8	30.1	27.3	15.6
7.3	413.0	13.1	47.5	20.3	29.1	27.8	18.5
7.8	269.4	13.3	48.4	20.8	28.6	28.3	13.0
8.3	196.1	13.8	55.6	21.3	25.7	28.8	15.0
8.5	182.9	14.3	61.9	21.8	23.9		
8.6	181.7	14.8	68.7	22.3	21.5		

Table 2.5: Hydrogen - Allene scattering data.

θ	$I(\theta)$	θ	$I(\theta)$	θ	$I(\theta)$	θ	$I(\theta)$
2.8	5531.1	9.6	267.4	17.3	62.7	24.8	24.2
3.3	2966.7	10.1	243.0	17.8	53.9	25.3	23.4
3.8	1711.4	10.6	213.2	18.3	45.2	25.8	24.3
4.1	1371.0	11.1	190.0	18.8	38.7	26.3	24.2
4.4	1236.7	11.6	166.3	19.3	32.9	26.8	22.0
5.1	1142.1	12.1	147.3	19.8	35.4	27.3	20.4
5.6	1055.1	12.6	129.9	20.3	35.6	27.8	23.2
5.8	1000.0	13.1	112.9	20.8	39.1	28.3	19.1
6.1	901.5	13.6	96.0	21.3	40.2	28.8	18.1
6.6	698.4	14.1	82.2	21.8	37.5	29.3	17.9
7.1	536.3	14.6	72.4	22.3	36.2	29.8	18.1
7.6	411.0	15.1	67.8	22.8	31.2	30.3	15.1
8.1	340.9	15.6	70.2	23.3	28.2		
8.6	307.5	16.3	70.5	23.8	24.1		
9.1	286.5	16.8	69.6	24.3	23.8		

Table 2.6: Hydrogen - Diacetylene scattering data.

θ	$I(\theta)$	θ	$I(\theta)$	θ	$I(\theta)$	θ	$I(\theta)$
4.5	1143.0	10.0	242.9	15.5	81.7	21.0	40.9
5.0	1055.3	10.5	226.2	16.0	81.4	21.5	41.2
6.0	878.1	11.0	216.1	16.5	78.8	21.0	40.2
6.5	747.7	11.5	202.8	17.0	75.1	22.0	39.8
5.5	1000.0	12.0	183.1	17.5	70.1	22.5	39.9
7.0	620.1	12.5	158.5	18.0	63.7	23.0	33.7
7.5	512.4	13.0	136.8	18.5	56.5	23.5	32.2
8.0	425.9	13.5	114.0	19.0	48.6	24.0	31.2
8.5	359.0	14.0	96.6	19.5	44.5	24.5	28.4
9.0	303.8	14.5	87.3	20.0	40.4	25.0	28.1
9.5	268.5	15.0	81.4	20.5	38.0	25.5	27.4

Table 2.7: Neon - Acetylene scattering data.

θ	$I(\theta)$	θ	$I(\theta)$	θ	$I(\theta)$	θ	$I(\theta)$
1.9	1613.6	4.3	252.0	10.3	19.1	16.3	15.0
2.0	1491.5	4.8	180.9	10.8	17.8	16.8	15.1
2.2	1230.0	5.3	131.1	11.3	16.6	17.3	15.0
2.4	1015.7	5.8	100.0	11.8	16.3	17.8	14.8
2.6	829.5	6.3	73.7	12.3	16.1	18.3	15.0
2.8	718.1	6.8	57.1	12.8	15.3	18.8	15.2
3.0	619.5	7.3	46.0	13.3	15.0	19.3	13.9
3.2	545.5	7.8	37.3	13.8	15.3	19.8	15.3
3.4	471.1	8.3	31.4	14.3	14.8	20.8	13.6
3.6	403.9	8.8	26.6	14.8	14.9	21.8	14.7
3.8	347.5	9.3	23.4	15.3	15.0	22.8	14.8
4.0	298.3	9.8	21.0	15.8	15.1	23.8	16.0

Table 2.8: Neon - Ethylene scattering data.

θ	$I(\theta)$	θ	$I(\theta)$	θ	$I(\theta)$	θ	$I(\theta)$
2.0	1493.3	7.0	59.8	13.0	12.9	19.0	12.1
2.5	978.9	7.5	47.3	13.5	12.6	19.5	12.2
3.0	655.4	8.0	38.2	14.0	12.5	20.0	12.3
3.5	468.7	8.5	31.6	14.5	12.2	21.0	11.6
4.0	328.5	9.0	26.6	15.0	12.1	22.0	12.0
4.2	289.0	9.5	23.0	15.5	12.0	23.0	12.1
4.5	243.4	10.0	20.1	16.0	12.0	24.0	12.2
4.5	241.3	10.5	18.2	16.5	11.8	25.0	11.6
5.0	177.1	11.0	16.4	17.0	11.9	26.0	11.9
5.5	131.3	11.5	15.5	17.5	12.0	27.0	12.1
6.0	100.0	12.0	14.4	18.0	12.0	28.0	12.2
6.5	76.6	12.5	13.6	18.5	11.9		

Table 2.9: Neon - Allene scattering data.

θ	$I(\theta)$	θ	$I(\theta)$	θ	$I(\theta)$	θ	$I(\theta)$
1.7	1377.1	7.0	63.1	13.0	9.1	19.0	6.6
2.0	997.0	7.5	50.2	13.5	8.3	19.5	6.7
2.5	659.5	8.0	40.6	14.0	8.0	20.0	6.9
3.0	479.1	8.5	32.5	14.5	7.5	21.0	6.7
3.5	357.8	9.0	26.9	15.0	7.4	22.0	6.9
4.0	272.4	9.5	22.4	15.5	7.1	23.0	6.9
4.2	243.5	10.0	18.8	16.0	7.0	24.0	7.0
4.5	210.7	10.5	15.7	16.5	6.8	25.0	6.7
5.0	162.6	11.0	13.9	17.0	6.9	26.0	6.9
5.5	128.2	11.5	12.3	17.5	6.6	27.0	7.1
6.0	100.0	12.0	10.9	18.0	6.8	28.0	7.6
6.5	79.7	12.5	9.7	18.5	6.9		

Table 2.10: Neon - Diacetylene scattering data.

θ	$I(\theta)$	θ	$I(\theta)$	θ	$I(\theta)$	θ	$I(\theta)$
2.0	845.6	7.5	52.5	13.0	8.5	18.5	5.3
2.5	560.2	8.0	42.4	13.5	7.6	19.0	5.4
3.0	405.5	8.5	33.8	14.0	6.9	19.5	5.4
3.5	308.0	9.0	28.2	14.5	6.5	20.0	5.3
4.0	244.1	9.5	23.0	15.0	6.0	21.0	5.3
4.5	192.3	10.0	19.5	15.5	5.8	22.0	5.3
5.0	154.7	10.5	16.0	16.0	5.7	23.0	5.3
5.5	125.4	11.0	13.9	16.5	5.5	24.0	5.0
6.0	100.0	11.5	11.9	17.0	5.4	25.0	5.2
6.5	81.0	12.0	10.4	17.5	5.5		
7.0	65.3	12.5	9.3	18.0	5.4		

Table 2.11: Neon - Acetylene scattering data at high resolution.

θ	$I(\theta)$	θ	$I(\theta)$	θ	$I(\theta)$	θ	$I(\theta)$
1.8	3404.1	3.6	666.4	5.6	195.6	7.8	62.2
2.0	2733.9	3.8	578.9	5.8	171.1	8.0	59.2
2.2	2114.4	4.0	523.3	6.0	153.2	8.2	54.9
2.4	1719.4	4.2	482.0	6.2	132.0	8.4	52.8
6.8	100.0	4.4	423.3	6.4	121.7	8.6	52.0
2.6	1497.8	4.6	356.8	6.6	110.8	8.8	46.5
2.8	1329.3	4.8	297.3	7.0	91.3	9.0	43.5
3.0	1156.5	5.0	260.6	7.2	83.1		
3.2	984.0	5.2	236.1	7.4	74.0		
3.4	808.0	5.4	219.4	7.6	66.7		

Table 2.12: Neon - Ethylene scattering data at high resolution.

θ	$I(\theta)$	θ	$I(\theta)$	θ	$I(\theta)$	θ	$I(\theta)$
1.8	2771.4	3.4	755.8	5.2	234.9	7.2	82.1
2.0	2253.2	3.6	649.5	5.4	212.0	7.4	76.1
2.2	1824.0	3.8	572.2	5.6	181.8	7.6	69.6
2.4	1503.4	4.0	520.2	5.8	165.1	7.8	61.7
6.8	100.0	4.2	457.8	6.0	145.3	8.0	57.8
2.6	1343.7	4.4	401.5	6.2	131.5	8.2	55.1
2.8	1209.5	4.6	336.4	6.4	120.8		
3.0	1045.5	4.8	296.1	6.6	110.2		
3.2	891.5	5.0	255.7	7.0	89.1		

Table 2.13: Neon - Allene scattering data at high resolution.

θ	$I(\theta)$	θ	$I(\theta)$	θ	$I(\theta)$	θ	$I(\theta)$
1.8	1727.2	4.0	401.2	6.4	122.6	9.0	39.6
2.0	1416.4	4.2	364.7	6.6	113.6	9.2	37.1
2.2	1174.2	4.4	324.1	7.0	92.3	9.4	34.1
2.4	1016.5	4.6	298.0	7.2	82.5	9.6	33.7
6.8	100.0	4.8	266.9	7.4	77.4	9.8	29.9
2.6	914.3	5.0	243.5	7.6	69.5	10.3	26.8
2.8	811.1	5.2	221.2	7.8	65.5	10.8	21.9
3.0	712.2	5.4	198.4	8.0	60.6	11.3	21.4
3.2	622.3	5.6	179.0	8.2	56.2	11.8	19.0
3.4	562.5	5.8	162.4	8.4	52.4		
3.6	504.1	6.0	150.7	8.6	46.4		
3.8	461.4	6.2	137.1	8.8	43.1		

Table 2.14: Argon - Ethylene scattering data.

θ	$I(\theta)$	θ	$I(\theta)$	θ	$I(\theta)$	θ	$I(\theta)$
2.8	1539.8	8.0	357.1	12.3	103.0	17.8	45.2
3.3	1095.5	8.1	348.2	12.8	90.6	18.3	45.2
3.8	831.9	8.3	329.7	13.3	79.2	18.8	45.4
4.3	698.2	8.5	312.8	13.8	71.7	19.8	43.7
4.8	617.2	8.8	287.0	14.3	64.4	20.8	42.5
5.3	568.0	9.3	250.5	14.8	59.2	21.8	43.5
5.8	529.2	9.8	216.6	15.3	55.4	22.8	42.2
6.3	492.1	10.3	185.5	15.8	52.2	23.8	43.4
6.8	453.0	10.8	158.2	16.3	50.5	24.8	42.0
7.3	411.5	11.3	138.2	16.8	48.0		
7.8	371.9	11.8	118.0	17.3	46.2		

Table 2.15: Argon - Allene scattering data.

θ	$I(\theta)$	θ	$I(\theta)$	θ	$I(\theta)$	θ	$I(\theta)$
3.3	262.2	9.7	51.0	11.7	34.2	13.7	23.8
3.8	195.0	9.8	49.4	11.8	33.6	13.8	23.2
4.3	155.5	9.9	49.1	11.9	33.0	13.9	23.1
4.8	127.6	10.0	48.1	12.0	32.3	14.0	22.6
5.3	111.3	10.1	47.3	12.1	31.4	14.3	21.3
5.8	100.0	10.2	46.4	12.2	31.0	14.8	19.8
6.3	92.0	10.3	45.2	12.3	30.5	15.3	18.6
6.8	84.3	10.4	44.6	12.4	30.0	15.8	17.3
7.3	78.2	10.5	43.8	12.5	29.4	16.3	16.6
7.7	73.2	10.6	42.7	12.6	28.5	16.8	15.4
8.3	66.1	10.7	42.1	12.7	28.1	17.3	14.5
8.8	60.4	10.8	41.0	12.8	27.6	17.8	14.1
8.9	59.5	10.9	40.2	12.9	27.4	18.3	14.1
9.0	58.7	11.0	39.6	13.0	26.9	18.8	13.1
9.1	57.8	11.1	38.2	13.1	26.2	19.8	12.8
9.2	56.7	11.2	37.6	13.2	25.9	20.8	12.7
9.3	55.2	11.3	37.0	13.3	25.4	21.8	11.7
9.4	54.2	11.4	36.5	13.4	25.0	22.8	11.0
9.5	52.8	11.5	35.4	13.5	24.9	23.8	10.4
9.6	51.8	11.6	34.9	13.6	24.2	24.8	10.5

Table 2.16: Argon - Diacetylene scattering data.

θ	$I(\theta)$	θ	$I(\theta)$	θ	$I(\theta)$	θ	$I(\theta)$
2.2	771.3	7.5	74.9	13.5	30.4	20.0	15.5
2.5	587.7	8.0	69.9	14.0	28.4	21.0	14.7
2.8	462.8	8.5	65.0	14.5	26.6	22.0	13.6
3.0	396.6	9.0	60.5	15.0	24.9	23.0	13.1
3.5	288.4	9.5	56.0	15.5	23.4	24.0	12.4
4.0	213.7	10.0	52.0	16.0	21.5	25.0	11.9
4.5	169.9	10.5	48.8	16.5	20.8	26.0	11.7
5.0	135.0	11.0	44.7	17.0	19.9	27.0	10.7
5.5	116.4	11.5	41.2	17.5	19.1	28.0	10.2
6.0	100.0	12.0	38.4	18.0	17.9	29.0	10.3
6.5	89.5	12.5	35.3	18.5	17.4	30.0	9.8
7.0	81.0	13.0	32.9	19.0	16.6		

Table 2.17: Nitrogen - Ethylene scattering data.

θ	$I(\theta)$	θ	$I(\theta)$	θ	$I(\theta)$	θ	$I(\theta)$
2.8	263.2	7.8	62.9	12.8	14.4	17.8	7.4
3.3	198.9	8.3	55.1	13.3	12.9	18.3	7.3
3.8	161.2	8.8	47.6	13.8	11.1	18.8	7.1
4.3	138.7	9.3	41.1	14.3	10.2	19.8	7.2
4.8	123.0	9.8	35.4	14.8	9.2	20.8	7.2
5.3	110.8	10.3	30.3	15.3	8.7	21.8	7.0
5.8	100.0	10.8	26.1	15.8	8.3	22.8	6.8
6.3	89.7	11.3	22.4	16.3	7.6	23.8	6.4
6.8	80.1	11.8	19.2	16.8	7.7	24.8	6.2
7.3	71.6	12.3	16.4	17.3	7.5		

Table 2.18: Nitrogen - Allene scattering data.

θ	$I(\theta)$	θ	$I(\theta)$	θ	$I(\theta)$	θ	$I(\theta)$
4.0	186.4	10.0	44.7	13.8	20.4	17.6	12.7
4.5	150.0	10.2	43.0	14.0	20.0	17.8	12.8
5.0	126.3	10.4	40.7	14.2	19.1	18.0	13.1
5.5	110.9	10.6	39.6	14.4	18.4	18.2	12.5
6.0	100.0	10.8	37.9	14.6	17.8	18.4	12.8
6.5	89.3	11.0	36.1	14.8	17.0	18.6	13.2
7.0	82.5	11.2	34.7	15.0	16.9	18.8	12.6
7.5	75.0	11.4	33.4	15.2	16.5	19.0	12.6
8.0	67.8	11.6	31.6	15.4	15.8	19.2	12.6
8.2	65.6	11.8	30.3	15.6	15.8	19.5	12.2
8.4	62.6	12.0	29.5	15.8	15.1	20.0	11.9
8.5	60.3	12.2	28.4	16.0	15.2	20.5	12.1
8.6	59.4	12.4	26.8	16.2	14.6	21.0	12.0
8.8	57.5	12.6	26.0	16.4	14.2	21.5	10.7
9.0	55.0	12.8	24.5	16.6	13.9	22.0	11.6
9.2	53.2	13.0	24.1	16.8	13.8	22.5	11.2
9.4	51.3	13.2	22.3	17.0	13.8	23.0	10.7
9.6	49.1	13.4	22.3	17.2	13.3	23.5	10.8
9.8	47.0	13.6	21.3	17.4	13.3	24.0	8.9

Table 2.19: Carbon Monoxide - Acetylene scattering data.

θ	$I(\theta)$	θ	$I(\theta)$	θ	$I(\theta)$	θ	$I(\theta)$
2.8	269.2	7.8	65.8	12.8	20.3	17.8	10.3
3.3	199.8	8.3	58.7	13.3	18.2	18.3	9.8
3.8	162.7	8.8	52.0	13.8	16.7	18.8	9.6
4.3	139.9	9.3	46.1	14.3	15.3	19.8	9.2
4.8	123.2	9.8	41.2	14.8	14.1	20.8	8.7
5.3	110.8	10.3	36.1	15.3	13.0	21.8	8.4
5.8	100.0	10.8	32.0	15.8	12.1	22.8	7.9
6.3	90.7	11.3	28.8	16.3	11.4	23.8	7.5
6.8	82.0	11.8	25.4	16.8	10.9	24.8	7.0
7.3	73.6	12.3	22.5	17.3	10.3		

Table 2.20: Carbon Monoxide - Ethylene scattering data.

θ	$I(\theta)$	θ	$I(\theta)$	θ	$I(\theta)$	θ	$I(\theta)$
2.8	273.3	7.8	65.7	12.8	18.7	17.8	8.4
3.3	202.6	8.3	58.6	13.3	16.5	18.3	8.2
3.8	164.1	8.8	51.9	13.8	14.7	18.8	8.1
4.3	139.6	9.3	46.0	14.3	13.4	19.8	7.9
4.8	122.8	9.8	40.7	14.8	12.0	20.8	7.7
5.3	111.0	10.3	35.7	15.3	11.0	21.8	7.5
5.8	100.0	10.8	31.2	15.8	10.2	22.8	7.1
6.3	90.3	11.3	27.4	16.3	9.4	23.8	6.9
6.8	81.5	11.8	24.2	16.8	9.1	24.8	6.9
7.3	73.1	12.3	21.2	17.3	8.8		

Table 2.21: Carbon Monoxide - Allene scattering data.

θ	$I(\theta)$	θ	$I(\theta)$	θ	$I(\theta)$	θ	$I(\theta)$
3.5	242.0	9.0	51.5	14.5	20.0	20.0	14.1
4.0	182.7	9.5	47.3	15.0	18.3	20.5	14.5
4.5	142.6	10.0	43.6	15.5	17.6	21.0	13.3
5.0	121.7	10.5	39.6	16.0	17.0	21.5	13.2
5.5	114.7	11.0	35.1	16.5	16.5	22.0	12.4
6.0	100.0	11.5	32.1	17.0	15.6	22.5	12.7
6.5	84.4	12.0	29.5	17.5	16.0	23.0	12.0
7.0	76.0	12.5	26.8	18.0	15.9	23.5	11.4
7.5	68.3	13.0	24.2	18.5	15.6		
8.0	62.7	13.5	23.3	19.0	14.9		
8.5	56.5	14.0	21.0	19.5	14.8		

Table 2.22: Nitric Oxide - Acetylene scattering data.

θ	$I(\theta)$	θ	$I(\theta)$	θ	$I(\theta)$	θ	$I(\theta)$
3.5	203.4	8.3	60.2	13.3	21.2	18.3	10.9
3.8	178.6	8.8	53.7	13.8	19.0	18.8	10.5
4.3	148.7	9.3	48.8	14.3	17.2	19.8	9.7
4.8	127.6	9.8	43.8	14.8	15.7	20.8	9.4
5.3	112.9	10.3	39.0	15.3	14.8	21.8	8.6
5.8	100.0	10.8	35.1	15.8	13.8	22.8	8.1
6.3	90.6	11.3	31.5	16.3	12.9	23.8	7.4
6.8	81.5	11.8	28.3	16.8	12.3	24.8	7.1
7.3	73.9	12.3	25.7	17.3	11.7		
7.8	66.5	12.8	23.0	17.8	11.5		

Table 2.23: Nitric Oxide - Ethylene scattering data.

θ	$I(\theta)$	θ	$I(\theta)$	θ	$I(\theta)$	θ	$I(\theta)$
3.3	201.6	8.3	57.3	13.3	15.4	18.3	7.8
3.8	163.5	8.8	50.3	13.8	13.7	18.8	7.9
4.3	139.7	9.3	44.4	14.3	12.1	19.8	7.4
4.8	123.0	9.8	39.0	14.7	11.3	20.8	7.2
5.3	111.0	10.3	34.1	15.3	10.2	21.8	7.0
5.8	100.0	10.8	29.4	15.8	9.3	22.8	6.7
6.3	89.6	11.3	25.9	16.3	8.7	23.8	6.6
6.8	81.0	11.8	22.3	16.8	8.4		
7.3	72.4	12.3	19.8	17.3	8.2		
7.8	64.4	12.8	17.2	17.8	8.0		

Table 2.24: Nitric Oxide - Allene scattering data.

θ	$I(\theta)$	θ	$I(\theta)$	θ	$I(\theta)$	θ	$I(\theta)$
3.5	222.7	10.0	51.4	16.5	18.4	23.0	11.6
4.0	172.7	10.5	46.8	17.0	17.7	23.5	11.7
4.5	143.8	11.0	42.6	17.5	16.8	24.0	10.5
5.0	122.8	11.5	38.9	18.0	16.2	24.5	9.9
5.5	109.8	12.0	35.4	18.5	15.8	25.0	9.5
6.0	100.0	12.5	32.6	19.0	15.4	25.5	9.8
6.5	91.7	13.0	30.0	19.5	15.1	20.5	13.6
7.0	84.4	13.5	27.6	20.0	14.7	23.5	11.5
7.5	78.3	14.0	25.3	20.5	13.4	24.0	10.6
8.0	72.3	14.5	23.8	21.0	13.4	24.5	10.3
8.5	66.8	15.0	22.2	21.5	12.8		
9.0	61.4	15.5	20.9	22.0	12.4		
9.5	56.4	16.0	19.5	22.5	12.1		

2.3 *Time-of-Flight Analysis Experiments*

An essential piece of information required for analyzing the total differential scattering data is the velocity distributions of the probe and target molecular beams. The velocity of an atom or molecule can be determined by measuring the time it takes the particle to travel a known distance. A supersonic beam with a distribution of velocites will therefore have a corresponding distributions of flight times.

Figure 2.5 shows the experimental setup to measure the time-of-flight (TOF) distributions of the molecular beams under the same experimental conditions as the scattering experiments. Supersonic gases from the primary and secondary beam sources are directed towards a high speed chopper wheel assembly, which is placed in position B of the scattering apparatus. The 53 mm. diameter chopper, rotating at 400 Hz, creates brief 6 μs pulses of gas that spread in time due to the slow and fast velocity components. After traveling a fixed flight path, the particles are ionized by electron bombardment, mass filtered, and detected with a channeltron electron multiplier. The Extrel C50 mass spectrometer is operated in pulse-counting mode providing TTL logic pulses proportional to the ion density per unit time. An EG&G Ortec multichannel scaler (MCS) collects the digitized signal in many channels at 2 μs intervals after being triggered with a start pulse from the timing output of the chopper. To improve the signal to noise ratio, the signal is histogrammed over many passes to build-up the TOF distribution.

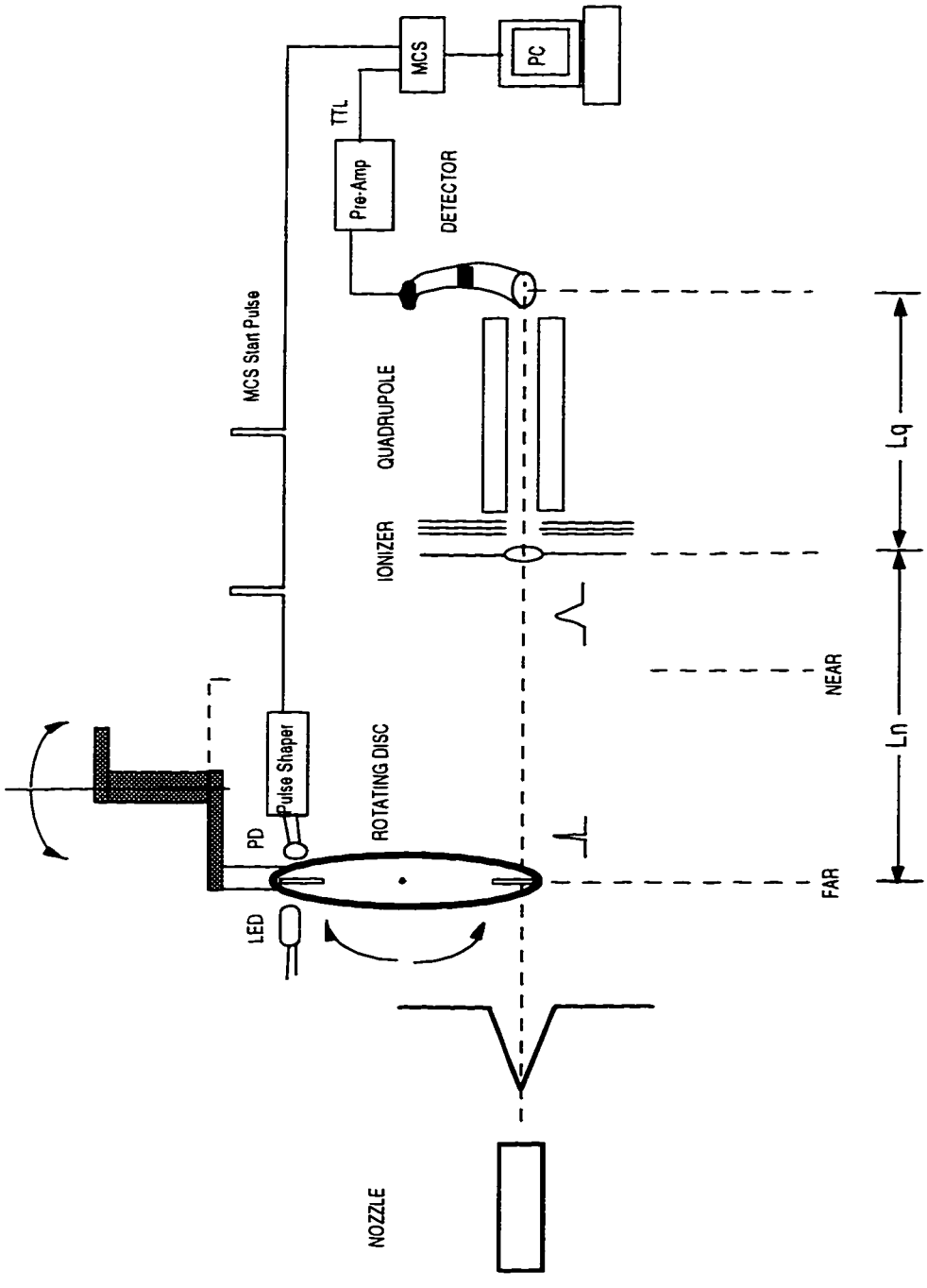

Figure 2.5: Experimental setup for time-of-flight measurements.

The absolute timing of the TOF distribution is accomplished with a LED - photodiode circuit which provides the logic start pulse to trigger the internal clock of the MCS. The chopper wheel has two diametrically opposed slits, allowing a voltage pulse from the LED - photodiode circuit to be generated as the bottom slit rotates through the gas beam. Because there are two slits, the 400 Hz chopper creates 6 μs pulse every 1.25 ms. The complete time-window of the MCS board is determined by the period between pulses, corresponding to 625 channels at 2μs intervals.

The actual timing is not exact and two corrections are needed to obtain an accurate TOF distribution as follows:

1. The two diametrically opposed slits are not exactly 180 degrees opposed, thus a small delay occurs in the TOF for rotation of the disk in one direction. This is corrected by also measuring the TOF with the chopper rotated in the reverse direction. Since the time delays in the two rotation direction are exactly opposite, the data can be averaged to cancel the delay.

2. A correction must be made for the time the particle spends in the mass spectrometer. After the particles are ionized they are accelerated and an additional flight time contributes to the total flight time. The chopper assembly may distance may be placed in two positions to determine the quadrupole flight length independently. Since the ion energy is known, the quadrupole flight time may be determined and subtracted after the first correction is made.

The total flight time for the chopper rotated in the forward direction is:

$$TOF_{forward} = T_n + T_q + T_{df} \tag{2.14}$$

where T_n is the neutral flight time, T_q the quadrupole flight time, and T_{df} is the delay time in the forward direction. Similarly, the total flight time for the chopper rotated in the reverse direction is:

$$TOF_{reverse} = T_n + T_q + T_{dr} \tag{2.15}$$

and T_{dr} is the delay time in the reverse direction. Since $T_{df} = -T_{dr}$, equations 2.14 and 2.15 can be summed to give:

$$T_n = \frac{1}{2}(TOF_{forward} + TOF_{reverse}) - T_q \tag{2.16}$$

The correction for quadrupole flight time, T_q can be directly calculated from the equations:

$$T_q = \frac{l_q}{v_q} \qquad \text{and} \qquad v_q = \sqrt{\frac{2qE_{ion}}{m}} \tag{2.17}$$

where l_q is the quadrupole length, v_q is the ion velocity calculated from the charge, q with mass, m, and ion energy, E_{ion}.

The previous equations express the TOF of a single particle. Using the simple relationship $v = l/t$, we can derive the TOF distribution $f(t)\,dt$ from the known velocity distribution given in Section 2.1.2. The conservation of flux implies that $f(t)\,dt = f(v)\,dv$. Since the MS ionization probability is proportional to $1/v$, the TOF distribution becomes:

$$\frac{1}{v}f(v)dv = \frac{t}{l}f(l/t)\left(-l/t^2\right)dt = -A\left(\frac{l^3}{t^4}\right)\exp\left[-F\left(\frac{l}{t}-G\right)^2\right]dt \tag{2.18}$$

where A, F, and G are constants which can be determined in terms of the neutral flight length, l, the stream velocity, v_s, and the velocity width v_w as:

$$G = \frac{v_s}{l} \qquad \text{and} \qquad F = \frac{l^2}{v_w^2}. \tag{2.19}$$

By applying the TOF corrections, the averaged TOF distrubtions may be fit to determine the parameters l,[3] A, F, and G from which the velocity information may be

[3]The neutral flight length in near and far positions were determined to 535 mm, and 636 mm, respectively, by assuming the atomic gas stream velocities were given by Eq. 2.4

determined. A previously developed nonlinear least-squares fitting procedure [21] was used to determine the TOF parameters with quite good accuracy. The flight times are estimated to be accurate to within 2-3% given the uncertainties in flight lengths, chopper frequency, and the discrete time sampling of the MCS. Figure 2.6 shows the fitted TOF spectra for the rare gases, diatomic molecules, and unsaturated hydrocarbons. The results of the non-linear least squares procedure and the quadrupole delay corresections are presented in Table 2.25.

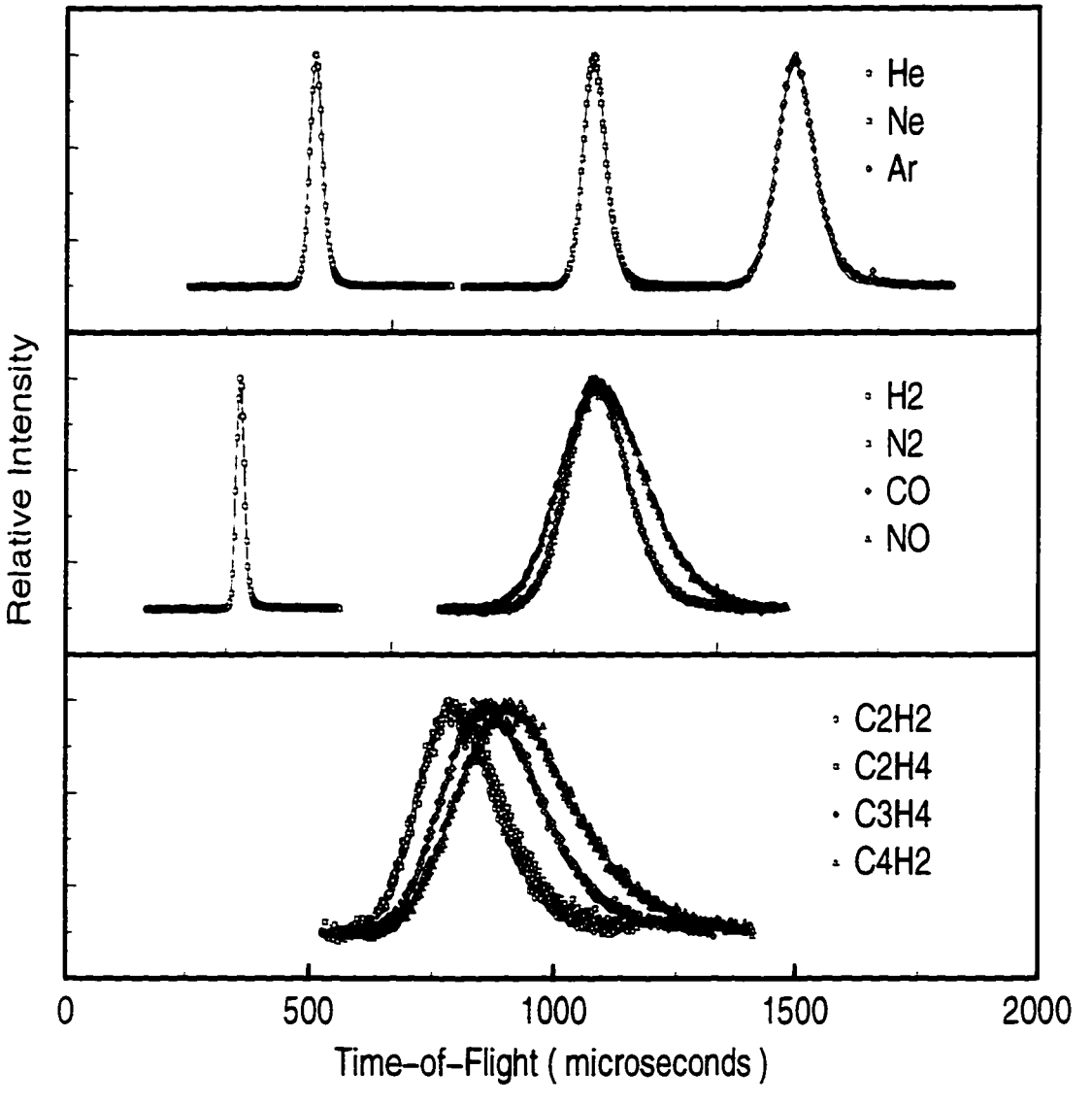

Figure 2.6: Time-of-Flight spectra for atomic, diatomic and polyatomic molecular beam source gases.

Table 2.25: Fitted TOF parameters for atomic, diatomic, and polyatomic gases.

	NEAR Position			FAR Position				
	A	F	G	A	F	G	V_q	T_q
System	$\times 10^{-11}$	$\times 10^{3}$	$\times 10^{-7}$	$\times 10^{-11}$	$\times 10^{3}$	$\times 10^{-7}$	m/s	μs
He	.078	3.34	5.10	.161	2.83	8.57	26876	10
Ne	1.79	1.53	35.7	3.64	1.28	63.6	11970	24
Ar	6.75	1.09	53.6	8.25	9.11	84.4	8508	32
H_2	.017	4.90	2.81	.037	4.17	5.29	37874	8
N_2	1.86	1.50	6.24	3.72	1.26	8.91	10160	28
CO	1.87	1.50	6.44	3.76	1.26	9.44	10159	28
NO	1.97	1.47	3.17	3.99	1.23	4.62	9816	28
C_2H_2	1.66	1.53	1.74	3.35	1.28	2.41	10538	26
C_2H_4	1.70	1.50	1.54	3.42	1.27	2.15	10152	28
C_3H_4	2.34	1.38	1.47	4.74	1.16	2.17	8495	32
C_4H_2	2.99	1.31	1.28	6.14	1.08	1.93	7598	34

The determined velocity distributions for all the source gases are presented in Table 2.26. Stream velocities range from approximately 600 to 2700 m/s for the heaviest and lightest gases, respectively. The measured velocities agree with predictions using Equation 2.4 to with in 1-5%. The largest discrepancy in the stream velocity data is for H_2 which is known to be less relaxed due its large rotational constant [47, 82]. Special consideration of the H_2 spin statistics should also be taken into account. The actual measured velocities agree very well with measurements of velocity distributions of supersonic gases in other molecular beam experiments [124, 21, 121]. The measured velocity resolutions are found to be around 1-10% for the expanded gases.

The diatomic and polyatomic gases have the largest velocity widths, primarily due to the lower stagnation pressures used to avoid condensation. The determined Mach numbers indicate high quality supersonic beams for the atomic and diatomic gases ($M > 10$) and slightly supersonic beams for the hydrocarbon gases ($M < 10$).

Table 2.26: Velocity parameters for atomic, diatomic, and polyatomic gases.

System	mass amu	γ	P_0 KPa	T_0 Kelvin	v_s m/s	v_w m/s	v_{mp} m/s	M
He	4.0	1.67	1000	310	1796	75	1801	24
Ne	20.2	1.67	700	310	819	28	820	29
Ar	39.95	1.67	200	310	583	25	585	23
H_2	2.02	1.40	500	310	2660	101	2666	26
N_2	28.0	1.40	400	310	803	67	811	12
CO	28.0	1.40	300	310	804	68	812	12
NO	30.0	1.40	200	310	787	95	804	8
C_2H_2	26.0	1.40	50	310	818	130	848	6
C_2H_4	28.0	1.33	50	310	806	137	840	6
C_3H_4	40.0	1.33	50	310	742	142	734	5
C_4H_2	50.0	1.40	30-25	310	690	147	779	5

The rotational populations of the hydrocarbon molecules may be estimated by assuming an equilibrium between the translational and rotational degrees of freedom in the supersonic expansions as mentioned earlier. Table 2.27 gives the rotational constants of the unsaturated hydrocarbons from the literature [98, 72, 75, 79], the measured translational temperatures, estimates for maximum of the initial population of rotational states, j_{max},[4] and an estimate for the number of open channels, N_j,[5] at approximately 800 K relative collision energy. The effect of decreasing the

[4] j_{max} was obtained by a sum over states at T_r using linear molecule rigid-rotor partition function [80] and $E_j = B\,j(j+1)$.

[5] The number of open channels was estimated by $N_j = E/E_j$.

rotational constant from C_2H_2 to C_4H_2 leads to 3-fold increase in the number of open rotational channels. The higher translational temperatures as determined from the TOF analysis also leads to a larger number of initially populated rotational states. The true rotational populations of the hydrocarbon beams should be obtained from spectroscopy. In a previous study, Yang showed that the IOS total differential scattering cross sections for He-C_2H_2 in $j_i = 0, 1, 2$ gave similar, almost identical, results [126, 124]. The estimates for the number initial rotational states for C_2H_2 presented here also agree with those obtained in an earlier analysis of C_2H_2 molecular beams [121].

Table 2.27: Rotational Population Analysis of Hydrocarbons

	Rotational Constants					
	$\tilde{A}$	$\tilde{B}$	$\tilde{C}$	T_s	j_{max}	N_j
Molecule	cm^{-1}	cm^{-1}	cm^{-1}	K		
C_2H_2		1.177		26	3	20
C_2H_4	4.865	1.001	0.8284	32	4	22
C_3H_4	4.812	0.2963	0.2963	47	7	42
C_4H_2		0.1464		64	12	58

Chapter 3

SCATTERING THEORY

3.1 Introduction

The goal of this chapter is to elucidate the non-reactive scattering dynamics of thermal molecular collisions in the classical, quantal, and semi-classical regimes as they pertain to the total differential scattering measurements. In particular, we are primarily concerned with relating the total differential scattering cross section to the underlying intermolecular potential energy surface which governs the scattering process. Classical mechanics provides an intuitive understanding of the scattering dynamics, but it ultimately fails to quantitatively predict the scattering features in high resolution experiments [50, 70, 44]. An accurate description of the scattering features can be obtained using quantum mechanics, since this formalism properly includes interference effects and the quantization of internal states of the system [71, 81, 101]. Unfortunately, a full quantum mechanical solution is not always computationally feasible for all scattering problems, therefore approximate methods are required in order to make the problem more tractable without significant loss of accuracy. In many cases, semi-classical methods can provide an accurate description of the scattering dynamics with less computational effort [71, 35, 44, 88]. The efficient calculation of scattering cross sections is tremendously beneficial in the analysis of scattering data, especially when experimental averaging and re-iterative fitting procedures have to be considered in the comparison of the theoretical and experimental results.

In general, the calculation of the theoretical differential scattering cross section is performed by a sum over individual partial wave phase shifts that have been deter-

mined semi-classically from an assumed model potential. For the most part the scattering dynamics can be understood in terms of a single-channel elastic scattering calculation based on a spherically symmetric potential model. However, the anisotropy in the intermolecular potential requires that rotational inelastic collisions be considered. The coupling of rotational and orbital angular momentum lead to a set coupled second order scattering equations which are difficult to solve efficiently. Fortunately in many thermal scattering problems, several angular momentum decoupling approximations may be applied to reduce the computational task. The infinite-order-sudden (IOS) approximation allows a full decoupling of the angular momentum while retaining the damping effects due to the anisotropic intermolecular potential. The multichannel scattering dynamics under the IOS approximation essentially reduces to a single channel problem.

The theory presented in this chapter addresses the scattering problem primarily from the standpoint of elastic scattering, where the potential is spherically symmetric and no changes in internal states occur. To give an intuitive basis for understanding the connection of the differential scattering cross section to the intermolecular potential, a brief discussion of the classical scattering theory is given in Section 3.2. The accurate calculation the differential scattering cross section from quantum mechanical methods is briefly reviewed in Section 3.3, and the semi-classical phase shifts that determine the differential scattering cross section in the quantal solution are discussed in Section 3.4. Since inelastic collisions must be considered, the multichannel scattering formalism for atom-symmetric top collisions is given in Section 3.5 with emphasis on the IOS decoupling approximation.

3.2 Classical Scattering Theory

The theory of elastic binary collisions has been extensively developed in many popular textbooks concerning classical mechanics [50, 44, 70, 73]. Only a cursory overview of

the fundamental classical scattering concepts will be presented here with the purpose of developing the framework for understanding more complex scattering phenomena. To a large degree, classical scattering theory provides a sufficient, intuitive basis for understanding the features in the differential scattering cross section and their relationship to the intermolecular potential. In general, the outcome of a two body elastic collision results in the angular deflection of a particle due to the presence of intermolecular forces. The combination of all possible individual deflections comprise the differential scattering intensity which is measured in an experiment. The connection between the intermolecular potential and the differential scattering cross section is what must be determined in order to effectively analyze the scattering results in this thesis. The discussion given here was developed from many sources, but most closely follows that of Fluendy and Lawley [44].

In the interaction between two structureless bodies, the potential energy depends only upon the relative distance between particles. Therefore, the center-of-mass motion may be separated from the relative motion, and the two-body scattering problem can be reduced to an equivalent one-body scattering event. Figure 3.2 shows a typical scattering trajectory of a fictitious particle of mass μ interacting with an infinitely massive scattering center. As a consequence of the conservation of energy and angular momentum, scattering trajectory is confined to a plane and the evolution of scattering process results in the angular deflection of the particle to an angle χ, which of course depends on the details of the intermolecular potential, $V(r)$, the impact parameter, b, and the relative collision energy, $E = \frac{1}{2}\mu g^2$. A close analysis of Figure 3.2 reveals the deflection angle may be related to the orientation angle θ_0 by:

$$\chi(b, E) = \pi - 2\theta_0 \,. \tag{3.1}$$

The total energy of the equivalent one-body interaction is usually expressed in relative coordinates by:

$$E = \frac{1}{2}\mu\dot{r}^2 + \frac{L^2}{2\mu r^2} + V(r) \tag{3.2}$$

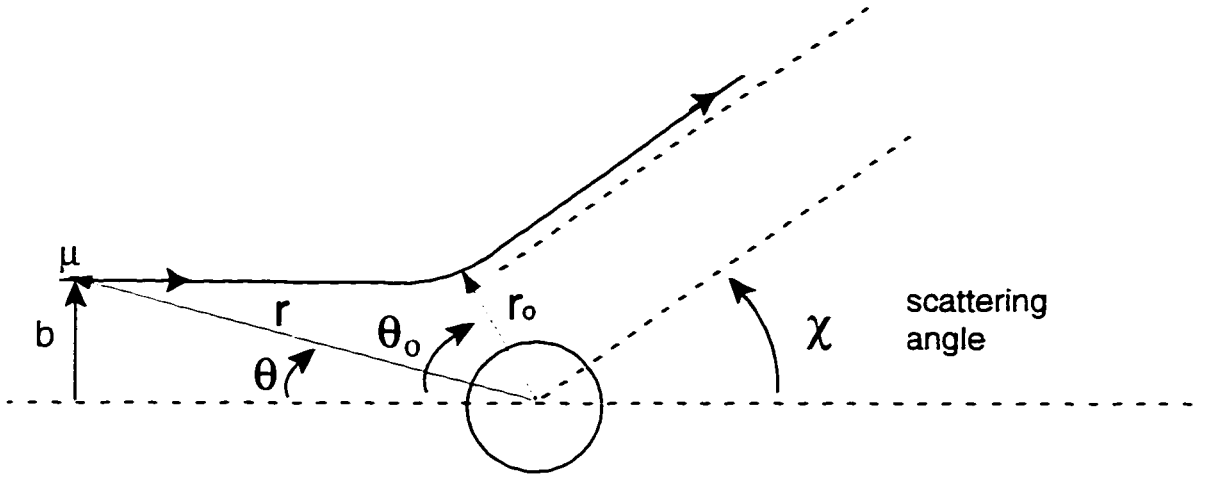

Figure 3.1: Scattering trajectory for a two body binary elastic collision. A fictitious particle μ at impact parameter, b, is deflected to angle, χ. The turning point of the potential is indicated by θ_0 and r_0.

where the first term represents the relative kinetic energy, the second term is the centrifugal potential energy with orbital angular momentum, L, and $V(r)$ is the intermolecular potential. The initial angular momentum, $L_i = \mu g b$, is a function of the relative velocity g and more importantly, the impact parameter b, which defines the collision in the absence of the potential. During the collision process the conservation of angular momentum requires that initial angular momentum equals the final angular momentum at any point during the scattering event, $L_f = \mu r^2 \dot{\theta}$. To determine the deflection angle the equations of motion must be solved.

The equation of motion for the radial coordinate, $\dot{r}$, can be expressed by rearranging Equation 3.2 as follows:

$$\dot{r} = \left[\frac{2}{\mu}\left\{E - \frac{Eb^2}{r^2} - V(r)\right\}\right]^{\frac{1}{2}} \tag{3.3}$$

where the initial angular momentum has been used has been used to simplify the equation. The angular velocity is determined from the final angular momentum by $\dot{\theta} = L/\mu r^2$.

The equations of motion for radial and angular coordinates define the scattering

trajectory. In order to yield a time independent solution, they may be arranged as follows:

$$\frac{d\theta}{dr} = \frac{\dot{\theta}}{\dot{r}} = \frac{b}{r^2}\left[1 - \frac{b^2}{r^2} - \frac{V(r)}{E}\right]^{-\frac{1}{2}} . \tag{3.4}$$

The integration of the Equation 3.4 allows the orientation angle at the turning point, θ_0, to be determined in terms of the equations of motion as:

$$\theta_0 = \int_0^{\theta_0} d\theta = -\int_{\infty}^{r_0}\left[1 - \frac{b^2}{r^2} - \frac{V(r)}{E}\right]^{-\frac{1}{2}} br^{-2}dr . \tag{3.5}$$

Using Equations 3.5 and 3.1, the deflection function of the particle is given by:

$$\chi(b, E) = \pi - 2b\int_{r_0}^{\infty}\left[1 - \frac{b^2}{r^2} - \frac{V(r)}{E}\right]^{-\frac{1}{2}} r^{-2}dr . \tag{3.6}$$

which is expressed in terms of the collision energy, impact parameter, and the potential energy.

Figure 3.2 show a typical deflection function for an attractive-repulsive potential in the thermal energy regime. It is important to notice that for a given potential, small impact parameters lead to large positive angular deflections that probe primarily the repulsive part of the potential; and the large impact parameters lead to small negative angular deflections that probe mostly the attractive potential. The positive and negative branches coalesce when the attractive and repulsive forces balance, leading to zero angular deflection. Also, evident in Figure 3.2, is the deflection function minimum. At this point several impact parameters may be deflected to the same absolute angle. In the context of classical scattering, this leads to a increased intensity at a given angle, since all impact parameters are equally probable in a scattering process. This point gives rise to rainbow scattering. In the quantum mechanical formalism, the wave properties of the particles must be considered, leading to serious differences between the classical and quantum scattering outcomes.

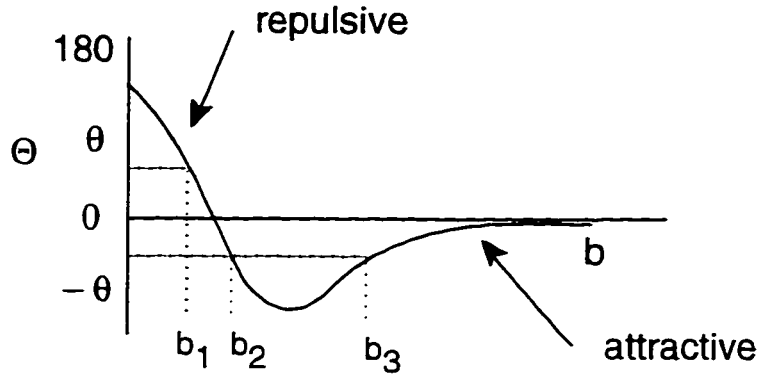

Figure 3.2: The classical deflection function for an attractive-repulsive potential.

3.2.1 *Differential Scattering Cross Section*

The differential scattering cross section is defined as the ratio of the scattered current per solid angle to the incident particle flux. More specifically, the differential scattering is essentially the number of particles per unit time which strike a detector subtending an angle $d\omega$ divided by the incident particle flux. For an incident current, J_0, which enters an infinitesimal area of $2\pi b db$, and is scattered into the solid angle, $d\omega = 2\pi \sin \chi d\chi$, the differential scattering cross section in the center of mass frame is given by:

$$I(\chi, E) = \frac{J_0 2\pi b db / 2\pi \sin \chi d\chi}{J_0} . \tag{3.7}$$

which is more conveniently expressed as:

$$I(\chi, E) = \frac{b}{\sin \chi \left(d\chi/db\right)} . \tag{3.8}$$

In a scattering experiment only absolute angular deflections may be detected, therefore the scattering angle is redefined as $\theta = |\chi|$. Considering collisions resulting from all equally probable impact parameters, the classical differential scattering cross section is usually given by:

$$I(\theta, E) = \sum_{i=1}^{n} \frac{b_i}{\sin \theta \left|d\theta/db_i\right|} . \tag{3.9}$$

Therefore, the differential scattering cross section depends directly on the form of the deflection function, or more correctly, on the slope of deflection function $d\theta/db$. Examination of Equation 3.9 reveals interesting singularities which arise that do not support the experimental observations for finite scattering at very small angles or at the rainbow angle. The classical results fail completely in predicting the diffraction oscillations. Forward or glory scattering results from zero angle scattering for a finite impact parameter, mainly concerning collisions where the attractive and repulsive forces cancel. The failure of classical methods to predict glory scattering results from the neglect of interference between particles which are deflected minimally and those which are outside the influence of the potential at very large impact parameters. The failure of the classical mechanics to predict finite rainbow scattering results from the neglect of interference from particles following nearly identical paths. Classically, the density of states is high near the rainbow point where $d\theta/db = 0$, leading to a divergence in the classical cross section.

The integral scattering cross section is also an important quantity and can be easily obtained through integration of Equation 3.9 to yield:

$$I_T(E) = \int I(\theta, E)d\omega = \int I(\theta, E)2\pi \sin\theta d\theta. \tag{3.10}$$

Unfortunately, the classical integral scattering cross section diverges for typical attractive-repulsive potentials. Given the failure of the classical results a more accurate description must be sought.

3.3 Quantum Scattering Theory

Quantum scattering theory incorporates the wave-particle nature of the scatterers and must obey the uncertainty principle, which prevents us from knowing simultaneously both the angular momentum and deflection angle to infinite precision. The singularities found in the classical results get "smeared" over by interference effects caused by the deBroglie wavelength dependence of the relative collision dynamics.

Proper treatment of the scattering problem in the quantum mechanical formalism predicts quantitatively the fast diffraction and rainbow oscillations in the differential scattering cross section. In general, the quantal solution expresses the differential scattering cross section in terms of individual partial wave phase shifts of distinct angular momentum which must be summed together. Rather than a single impact parameter leading to the scattering at a specific angle, in the quantum description all components of angular momentum contribute to scattering at given angle. It is the relative phase shifts caused by the intermolecular potential that gives rise to the quantum interferences which are measured in high resolution scattering experiments. The theory of elastic single-channel quantum scattering has appeared extensively in many texts on non-relativistic quantum mechanics [38, 35, 81, 88, 71]. The discussion presented here follows from Cohen-Tannoudji [38].

The complete single-channel quantal formalism requires a wavepacket description of the scattering dynamics. However, since the potential is time-invariant and the range of interaction is small compared to spatial dimensions of the wavepacket, the elastic scattering dynamics may be expressed in a stationary state formalism.

The time-independent nuclear Schrödinger equation is:

$$\hat{H}\Psi(\mathbf{r}) = E\Psi(\mathbf{r}) \tag{3.11}$$

where $\hat{H}$ is the Hamiltonian operator, and Ψ and E are the eigenvectors and eigenvalues respectively of the stationary states scattering problem. Since the potential depends only upon the relative distance between the scatterers, the center of mass motion may be separated and Equation 3.11 may be expressed in relative spherical coordinates as:

$$\left[-\frac{\hbar^2}{2\mu}\frac{1}{r}\frac{\partial^2}{\partial r^2}r + \frac{\hat{l}^2}{2\mu r^2} + V(r) - E\right]\Psi_k(\mathbf{r}) = 0 \tag{3.12}$$

where $\hat{l}^2$ orbital angular momentum operator, and $E = \hbar^2 k^2/2\mu$ is the relative collision energy which depends on the wavevector k.

The scattering is observed at dimensions much larger than the range of the potential. therefore we seek an asymptotic solution to Equation 3.12. The form of $\Psi_k(\mathbf{r})$ as $r \rightarrow \infty$ is given by:

$$\Psi_k(\mathbf{r}) \approx e^{ikz} + |f(\theta, o)|\frac{e^{ikr}}{r} = \Psi_k^0 + \Psi_k^S \tag{3.13}$$

where $\Psi_k^0 = e^{ikz}$ defines the incident plane wave state in the field free region moving along the direction z. and Ψ_k^S is the scattered spherical wave with amplitude $f(\Omega)$.

The general solution to Equation 3.12 can be determined by expanding the total wavefunction in terms of a complete set of partial wavefunctions with defined angular momentum, l. Thus.

$$\Psi_k(\mathbf{r}) = \frac{1}{r}\sum_{l=0}^{\infty}\sum_{m=-l}^{l} C_l \Phi_{klm}(r, \theta, o) \tag{3.14}$$

where $\Phi_{klm}(r, \theta, o)$ is the product of radial wavefunctions. $u_{kl}(r)$. and spherical harmonics functions. $Y_{lm}(\theta, o)$. expressed as:

$$\Phi_{klm}(r, \theta, o) = \frac{1}{r} u_{kl}(r) Y_{lm}(\theta, o)\,. \tag{3.15}$$

The normalization constant is given by $C_l = i^l\sqrt{4\pi(2l+1)}$ which is obtained by plane wave expansion of incident wave Ψ_k^0.

The spherical harmonic wavefunctions are eigenfunctions of the orbital angular momentum operator. $\hat{l}^2$ as follows:

$$\hat{l}^2 Y_{lm}(\theta, o) = \hbar^2 l(l+1) Y_{lm}(\theta, o)\,. \tag{3.16}$$

Since the incident plane wave state is directed along the z direction. the m component angular momentum is zero. Integration over the angular coordinates in Equation 3.14. taking into the orthogonality relationships of the spherical harmonic functions. yields a set of partial radial wave equations as:

$$\left[-\frac{\hbar^2}{2\mu}\frac{d^2}{dr^2} + \frac{l(l+1)}{2\mu r^2} + V(r) - \frac{\hbar^2 k^2}{2\mu}\right] u_{kl}(r) = 0 \tag{3.17}$$

which can be simplified to:

$$\left[\frac{d^2}{dr^2} - k^2 + \frac{2\mu}{\hbar^2}V_{eff}(r)\right] u_{kl}(r) = 0 \tag{3.18}$$

where V_{eff} is the effective potential. Notice at $r = 0$, the effective potential is infinite, satisfying the boundary condition for scattering at the origin, $u_{kl}(0) = 0$.

For large r, the effective potential is negligible, and Equation 3.18 is simplified by:

$$\left[\frac{d^2}{dr^2} - k^2\right] u_{kl}(r) = 0 \tag{3.19}$$

The general asymptotic solution as $r \to \infty$ to the radial wave equation given above is:

$$u_{kl}(r) \approx \sin(kr - l\pi/2 + \eta_l) \tag{3.20}$$

where the term $l\pi/2$ corresponds to phase shift due to the centrifugal potential and η_l is the phase shift caused by the potential, $V(r)$.

Equation 3.20 can be applied to Equation 3.15 to give the asymptotic behavior as:

$$\begin{aligned} \Phi_{klm}(r,\theta,o) &\approx \frac{\sin(kr - l\pi/2 + \eta_l)}{r} Y_{lm}(\theta,o) \\ &\approx -Y_{lm}(\theta,o)\frac{e^{-ikr}e^{i(l\pi/2-\eta_l)} - e^{ikr}e^{-i(l\pi/2-\eta_l)}}{2ir} \end{aligned} \tag{3.21}$$

where the second terms reflects the exponential form of the sin function.

We can multiply by arbitrary phase factor, $e^{i\eta_l}$ and choose the normalization to reduce Equation 3.21 to be:

$$\Phi_{klm}(r,\theta,o) \approx -Y_{lm}(\theta,o)\frac{e^{-ikr}e^{il\pi/2} - e^{ikr}e^{-il\pi/2}e^{2i\eta_l}}{2ikr} \tag{3.22}$$

Considering the $m = 0$ components of spherical harmonics and the normalization constant C_l for the partial waves Equation 3.22 becomes:

$$\begin{aligned} \Psi_k(\mathbf{r}) &\approx \sum_{l=0}^{\infty} C_l \Phi_{kl0}(r,\theta,o) \\ &\approx -C_l Y_{l0}(\theta,o)\frac{e^{-ikr}e^{il\pi/2} - e^{ikr}e^{-il\pi/2}e^{2i\eta_l}}{2ikr}. \end{aligned} \tag{3.23}$$

which shows explicitly contributions from the incoming and outgoing waves. As the incoming wave approaches the scattering center, it becomes more perturbed by the potential, until it is reflected as an outgoing wave with an accumulated phase shift of $2\eta_l$.

Using the fact that $e^{2i\eta_l} = 1 + 2ie^{i\eta_l}\sin\eta_l$ in the equation above, yields the final asymptotic solution to the scattering wave equation as :

$$\Psi_k(\mathbf{r}) \sim \sum_{l=0}^{\infty} C_l Y_{l0}(\theta, o) \times \left[\frac{e^{-ikr}e^{il\pi/2} - e^{ikr}e^{-il\pi/2}e^{2i\eta_l}}{2ikr} - \frac{e^{ikr}}{r}\frac{1}{k}e^{-il\pi/2}e^{i\eta_l}\sin\eta_l\right] \tag{3.24}$$

which has the proper form given initially in Equation 3.13. The first term represents a plane wave expansion of the incoming free particle and an outgoing spherical scattered wave .

The initial plane wave state is given by:

$$\Psi_k^0 \sim e^{ikz} = \sum_{l=0}^{\infty} C_l Y_{l0}(\theta, o) \times \left[\frac{e^{-ikr}e^{il\pi/2} - e^{ikr}e^{-il\pi/2}e^{2i\eta_l}}{2ikr}\right] \tag{3.25}$$

and the asymptotic scattered wave has the form:

$$\Psi_k^S = |f(\theta)|\frac{e^{ikr}}{r} = \sum_{l=0}^{\infty} C_l Y_{l0}(\theta, o)\frac{e^{ikr}}{r}\frac{1}{k}e^{-il\pi/2}e^{i\eta_l}\sin\eta_l \tag{3.26}$$

Comparision of Equations 3.26 and 3.13, gives directly the scattering amplitude:

$$f(\theta) = \frac{1}{k}\sum_{l=0}^{\infty}\sqrt{4\pi(2l+1)}e^{i\eta_l}\sin\eta_l Y_{l0}(\cos\theta) \ . \tag{3.27}$$

The differential scattering cross section being a probability for the scattering event to occur, requires that we square the scattering amplitude, $|f(\theta)|^2$. The derivation of the differential scattering can be determined by considering the quantum current operator for the radial component, which is given by:

$$\mathbf{J}(\mathbf{r}) = \frac{-\hbar}{2i\mu}\{\Psi_k\nabla_r\Psi_k^* - \Psi_k^*\nabla_r\Psi_k\} \tag{3.28}$$

Application of Equation 3.28 to the intial Ψ_{k0} and scattered Ψ_{S0} wavefunctions give the initial flux and scattered currents.

$$\mathbf{J_0} = \frac{\hbar k}{\mu} \quad \text{and} \quad \mathbf{J_S} = \frac{\hbar k}{\mu}\frac{1}{r^2}|f(\theta,o)|^2 \ . \tag{3.29}$$

The differential scattering cross section, considering the earlier definition from the classical scattering, is:

$$I(\theta) = \frac{\mathbf{J_S} r^2/d\Omega}{\mathbf{J_0}/d\Omega} = |f(\theta,o)|^2 \ . \tag{3.30}$$

the square of the scattering amplitude. The differential scattering cross section represents a probability for observing a scattering at a given angle. Using the the relationship shown earlier, the quantum mechanical scattering cross section in terms of the partial wave phase shifts η_l is expressed by:

$$\begin{aligned} I(\theta) &= \frac{1}{4k^2}\left[\sum_{l=0}^{\infty}(2l+1)\sin 2\eta_l P_l(\cos\theta)\right]^2 \\ &+ \frac{1}{4k^2}\left[\sum_{l=0}^{\infty}(2l+1)(\cos 2\eta_l - 1)P_l(\cos\theta)\right]^2 \end{aligned} \tag{3.31}$$

where the spherical harmonic functions have been reduced in terms of the Legendre polynomials.

Another important quantity is the total scattering cross section, which is determined by integrating over all scattering angles to be:

$$I_T(E) = \frac{4\pi}{k^2}\sum_{l=0}^{\infty}(2l+1)\sin^2\eta_l \ . \tag{3.32}$$

Equation 3.31 implies that the differential scattering cross section can be calculated directly knowing the phase shifts for each angular momentum state. Figure 3.3 shows the typical phase shift dependence on l for a typical attractive-repulsive potential in the thermal scattering regime. The figure shows that small angular momentum leads to negative phase shifts which are due to the repulsive potential, and large angular momentum gives rise to positive phase shifts primarily as a result of the attractive

potential. For very large angular momentum, the phase shifts become vanishingly small. In general, the number of angular momentum states which must be summed in order to determine the differential scattering cross section can be estimated by $l_{max} = kR_0$, where R_0 is the range of the intermolecular potential. For typical van der Waals interactions, approximately $l = 200 - 300$ gives adequate convergence.

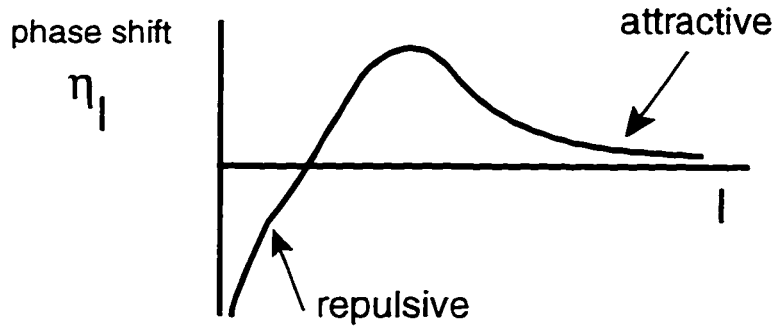

Figure 3.3: Partial Wave phase shifts vs l for a typical attractive-repulsive potential.

In most cases, the phase shifts for given potential must be obtained from numerical solution of the Schrödinger equation, since analytical solutions are uncommon and not generally valid over the full range of the intermolecular potential. Accurate numerical techniques allow the wavefunction to be propagated from a region inside the turning point to large distances where the phase of the scattering amplitude is stable. The relative phase shift can be calculated by considering the turning point for each angular momentum state and propagating two solutions, one with the full effective potential and the other with only the centrifugal potential, to large distance. By comparing the phase of the two solutions at long distance, where the phase becomes stable, the relative phase shift can be determined.

Figure 3.4 shows an example for the determination of relative phase shifts calculated by finite difference methods using a typical potential in the low angular momentum and high angular momentum cases. The full potential and wavefunction are

given by the solid lines, and the dashed lines indicate the centrifugal potential and wavefunction. In the low angular momentum case, we see that the full solution leads the centrifugal solution, therefore the phase shift is negative. For the high angular momentum case, the opposite is true. The full solution lags the centrifugal solution and the phase shift is positive. Considering the amplitude of the wavefunction, it is easy to see that the low angular momentum collisions spend less time in the interaction region due the repulsive potential, while the high angular momentum collisions spend more time in the interaction region due to the attractive potential.

Unfortunately, accurate numerical techniques are not always feasible in cases which require the evaluation of phase shifts for several hundred partial wave states. Numerical solutions usually require quite small step sizes for stability reasons, thus making the calculation too computationally expensive to be applicable to differential scattering problems. However, in many cases, full numerical accuracy is not always necessary and approximate methods can be used to determine the phase shifts with high efficiency.

3.4 *Semiclassical Phase Shift Approximation*

The JWKB method is a well known semi-classical technique applicable to many quantum mechanical problems. In the scattering formalism, the JWKB method allows the rapid calculation of partial wave phase shifts from a given model potential. The theory of the JWKB is well presented in many texts [35, 88, 101]. Only a summary, based mostly on discussions in Child is presented here.

The radial wave equation presented given in Equation 3.17 can be written as follows:

$$-\frac{d^2 u_{kl}(r)}{dr^2} = \left[k^2 - U(r) - \frac{l(l+1)}{r^2}\right] u_{kl}(r) \tag{3.33}$$

where

$$k^2 = 2\mu E/\hbar^2 \quad U(r) = 2\mu V(r)/\hbar^2 \tag{3.34}$$

a) high angular momentum, l

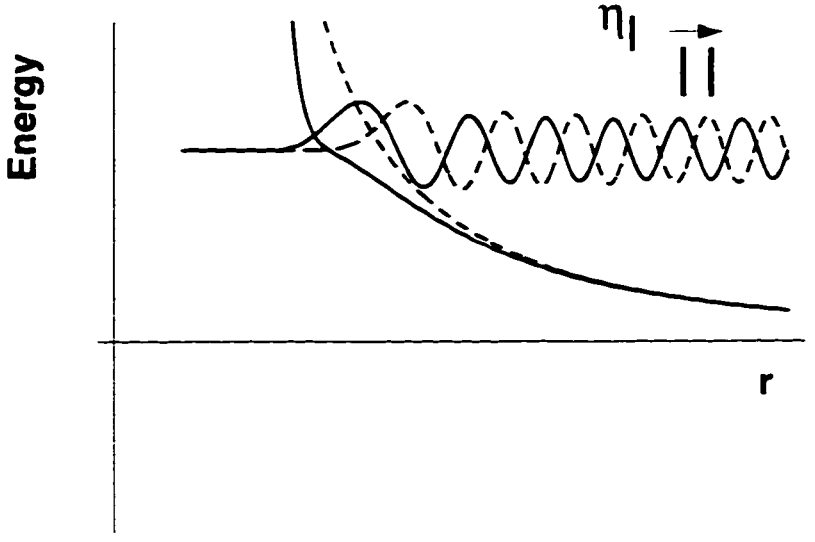

b) low angular momentum, l

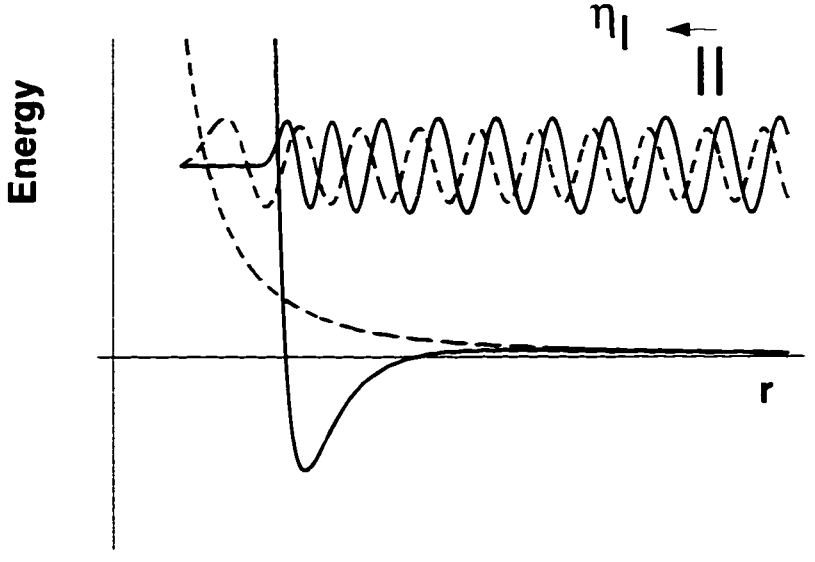

Figure 3.4: Phase shifts for high angular momentum and low angular momentum cases. Solid lines indicate full potential and solution, while dashed lines are the centrifugal potential and solution.

In the semi-classical approximation, we assume the solution has the form:

$$u_{kl}(r) = exp[iS(r)/\hbar] \tag{3.35}$$

where the phase factor S may be expanded in powers of $\hbar$ as:

$$S = S_0 + \hbar S_1 + \frac{\hbar^2}{2} S_2 + \ldots \tag{3.36}$$

By application of Equation 3.35 to Equation 3.33 gives the differential equation :

$$(S')^2 - i\hbar S'' = 2\mu \left(k^2 - U(r) + \frac{l(l+1)}{r^2} \right) = p^2(r) \tag{3.37}$$

Using Equation 3.36 into Equation 3.37 and keeping only terms to first order in $\hbar$ gives the two components to phase factor as follows:

$$S_0 = \pm \int p(r)\, dr \quad \text{and} \quad S_1 = \frac{i}{2} \ln p(r) \tag{3.38}$$

The first order JWKB wave function is obtained by taking a linear combination of the two solutions to give:

$$u^{\pm}_{kl}(r) = \frac{1}{[p(r)]^{1/2}} exp\left[\pm \frac{i}{\hbar} \int p(r)\, dr \right] \tag{3.39}$$

which is valid if

$$|\hbar S''| \ll \left| (S')^2 \right| . \tag{3.40}$$

Since $\lambda(r) = h/p(r) = 2\pi/k(r)$, the JWKB is valid if the gradient of the de-Broglie wavelength is much less than 2π, or

$$\left| \frac{d\lambda(r)}{dr^2} \right| \ll 2\pi . \tag{3.41}$$

A more common interpretation is that the potential must be slowly varying compared to the local wavelength.

The JWKB wave function in terms of the wave vector in the classically allowed region is:

$$u_{kl}(r) = [k_l(r)]^{-1/2} \sin \int_{r_0}^{\infty} k_l(r)\, dr + \frac{\pi}{4} \quad r > r_0 \tag{3.42}$$

where

$$k_l(r)^2 = k^2 - U(r) - \frac{l(l+1)}{r^2} \tag{3.43}$$

which is valid for all regions greater than the turning point r_0. At the turning point, the Langer approximation [35] to the centrifugal potential must be used.

$$\frac{l(l+1)}{r^2} \approx \frac{\left(l+\frac{1}{2}\right)^{1/2}}{r^2} \tag{3.44}$$

The semi-classical phase shift can be determined by equating the arguments of the quantum and the semiclassical solutions using Equations 3.20 and 3.42, respectively. The semiclassical phase shift is expressed as:

$$\begin{aligned} \eta_l &= \lim_{r\to\infty} \int_{r_0}^{r} k_l(r)\,dr - kr_0 + \left(l+\frac{1}{2}\right)\frac{\pi}{2} \\ &= \int_{r_0}^{\infty} k_l(r)\,dr - \int_{r_0^0}^{\infty} k_l^0(r)\,dr\,. \end{aligned} \tag{3.45}$$

indicating a relative phase shift determined from comparing two solutions at an asymptotic distance. The first term includes the full potential, and the second term includes only the contribution from centrifugal potential. The advantage of using the phase shift equation above is that a quadrature may be used rather than the a numerical integration. In our case, we use a Gauss-Mehler quadrature [2, 6] for the integration of Equation 3.45 to determine the phase shifts, and then Equation 3.31 to calculate the differential scattering cross section. Usually only the only first $l = 100$ or so phase shifts need to be determined semiclassically. At higher angular momentum where the phase shift becomes very small, the Born approximation may be used. This approximation is discussed in the next section.

For clarity it is important to relate the semiclassical phase shift function to the classical deflection function. By differentiating Equation 3.45 with respect to the angular momentum, the classical deflection function is obtained :

$$2\frac{\partial \eta_l}{\partial l} = \pi - 2\int_{r_0}^{\infty} \frac{(l+1/2)\,dr}{r^2 k_l(r)} \tag{3.46}$$

if

$$k_l(r) = \frac{1}{\hbar}[2\mu(E - V_{eff})]^{\frac{1}{2}} \quad \text{and} \quad L \approx \hbar(l + 1/2) \ . \tag{3.47}$$

The classical expression in Equation 3.6 is obtained in terms of the phase shift function. By comparing the angular momentum in the classical and semi-classical cases we see that

$$b = \frac{l + \frac{1}{2}}{k} \tag{3.48}$$

meaning that the classical impact parameter corresponds to a well defined angular momentum through the wave vector. The implication is that trajectories originating from a given impact parameter correspond to a particular angular momentum with an associated stationary phase. Thus, for trajectories leading to scattering at the same angle interference effects will result from the corresponding angular momentum components each with different relative phase dependence.

3.4.1 Born Phase Shift Approximation

At very large angular momentum ($l > 100$), the phase shifts become increasingly small. Rather than use the semiclassical JWKB technique, the Born approximation gives a more convenient expression for the phase shifts, which depends only upon the long range intermolecular potential. The Born approximation, an integral equation method, is based on perturbation theory and is obtained by expanding the wavefunction in powers of the potential [35, 38, 81].

The radial wave equation may be written in the following form:

$$\left[\frac{d^2}{dr^2} + k^2 - \frac{l(l+1)}{r^2}\right] u_{kl}(r) = U(r)\, u_{kl}(r) \tag{3.49}$$

where $U(r) = \frac{2\mu}{\hbar^2} V(r)$.

In general the solution can be written terms of an intial plane wave part and an outgoing Greens' function as follows:

$$u_{kl}(r) = u^0_{kl}(r) + \int_0^\infty G^+(r, r')\, U(r')\, u_{kl}(r')\, dr' \tag{3.50}$$

where u^0_{kl} is the solution in the absence of the potential and the outgoing Greens' function has proper asymptotic form as given by:

$$G^+(r,r') = \frac{-1}{k} u^+_{kl}(r)\, u^0_{kl}(r') \qquad r > r' \tag{3.51}$$

and

$$u^0_{kl}(r') = kr' j_l(kr') \approx \sin(kr' - l\pi/2) \tag{3.52}$$

$$u^+_{kl}(r) = ikrh^{(2)}_l \approx exp[i(kr - l\pi/2)] \tag{3.53}$$

A solution is obtained by iteration as follows:

$$\begin{aligned} u_{kl}(r) = u^0_{kl}(r) \;&+\; \int_0^\infty G^+(r,r')\, U(r')\, u^0_{kl}(r')\, dr' \\ &+\; \int_0^\infty \int_0^\infty G^+(r,r')\, U(r')\, G^+(r',r'')\, U(r'')\, u^0_{kl}(r'')\, dr'dr'' \ldots \end{aligned} \tag{3.54}$$

For the first-order Born approximation, valid for single scattering events in the high energy limit and where the potential perturbation is small, we keep only the first two terms of the iterative process. From Equation 3.54, the solution to the radial wave equation is:

$$\begin{aligned} u_{kl}(r) &= u^0(r) + \int_0^\infty G^+(r,r')\, U(r')\, u^0_{kl}(r')\, dr' \\ &\approx \sin(kr - l\pi/2) - k^{-1} exp(ikr - l\pi/2) \int_0^\infty U(r) \left[u^0_{kl}(r)\right]^2 dr \end{aligned} \tag{3.55}$$

which can be simplified to a more recognizable form as:

$$u_{kl}(r) \simeq e^{i\eta_l} \sin(kr - l\pi/2 + \eta_l)\ . \tag{3.56}$$

and the phase shift can be expressed analytically in terms of the potential. For an attractive long range potential where $V(r) = -C_s/r^s$ the, the Born approximation phase shift is given by:

$$\eta_l = -\frac{2C_s \mu k}{\hbar^2} \int_0^\infty r^{2-s} [j_l(kr)]^2 dr\ . \tag{3.57}$$

Using standard integration methods, the phase shifts under the Born approximation are given in a convenient form as:

$$\eta_l = \frac{\mu\pi C_s}{\hbar^2}\frac{k^{s-2}}{2}\frac{\Gamma(s-1)\,\Gamma(l-s/2+3/2)}{\Gamma(s/2)^2\Gamma(l+s/2+1/2)}. \tag{3.58}$$

In the calculation of the differential scattering cross section, the first $l \approx 100$ are computed semi-classically, but at higher angular momentum, the Born approximation is preferred. The actual switch between the two methods is determined by comparing the phase shifts for both cases. When the methods agree to within 1%, the Born approximation is used, rather than the JWKB quadrature, to calculate the remaining phase shifts, $l \approx 150 - 200$.

3.5 Multichannel Scattering Theory

3.5.1 Introduction

The previous discussions concentrated on the classical and quantal elastic scattering theories of centrally symmetric systems. For molecular systems, inelastic transitions between the internal degrees of freedom are possible as a result of the anisotropy in the potential energy surface. Under thermal energy conditions rotational transition are most probable, and the vibrational and electronic degrees freedom for the most part do not change state in the collision process. The work presented in this thesis concerns the rotationally inelastic scattering of atom-symmetric top or linear molecule systems. A good discussion of inelastic scattering can be found in many books and articles [17, 111, 52, 25]. The full multichannel scattering problem requires a solution to the time-independent nuclear Schrödinger for the complete system. In general, the total wavefunction is expanded in terms of total angular momentum functions of the coupled rotational and orbital momenta and radial wavefunctions of the collision coordinate. The radial wavefunctions are solutions to a set of second order differential equations, which are coupled due to the orientation dependence of the intermolecular

potential. The outcome of the scattering process is obtained from the asymptotic behavior of the scattering amplitude in terms of the collisional S-matrix, which contains the specific information for determining the inelastic transition probabilities and the total differential scattering cross sections for the molecular systems.

The close-coupled equations are essentially exact in the limit of an infinite number basis functions in **J** and **j**, but the degeneracy of the rotational sublevels $(2j + 1)$ leads to increased dimensionality of the scattering equations. The actual number of coupled channels used in the calculation depends on the number of rotational levels accessible at the relative collision energy. In general, the high dimensionality can be reduced by considering the conservation properties in the multichannel problem. The conservation of total angular momentum $\mathbf{J} = \mathbf{l} + \mathbf{j}$, owing to the rotational invariance of the total Hamiltonian, allows the scattering equations to be block diagonalized in both **J** and **M**. Since the total energy depends on J and not M, only one solution of M needs to be determined for each value of J. The conservation of parity $P = (-1)^{l+j+k}$ of the total wavefunction, due to the invariance on inversion of the spatial coordinates, enables the solutions to be separated into non-interacting blocks of symmetric and antisymmetric contributions for each **J**. Separate calculations can be performed for each parity case, which leads to the general selection rule in molecular scattering theory, where only even or odd changes in the rotational quantum numbers contribute for each parity case.

Despite the reduction in complexity obtained using the conservative properties, other considerations make the multichannel formalism too difficult to be applied in most cases. For molecular scattering systems with small rotational constants, there are many energetically accessible channels which must be included in the basis to obtain proper convergence, making the full close-coupled equations too complex to solve efficiently. Further, in many cases, the full accuracy of the scattering dynamics is not always needed given the overall quality of the scattering data. This is especially true for non-state selected experiments where only an average over all orientations

is measured and the detailed state-to-state transitions are for the most part unresolved. Fortunately, several approximation methods can be used in order to reduce the complexity of the close-coupled equations. The coupled-states (CS) approximation [66, 78] decouples the rotational and orbital angular momentum through approximation of the centrifugal potential energy, making the scattering equations coupled in j but decoupled in l. The infinite-order-sudden (IOS) approximation [66, 101, 100] uses the same approximation to the centrifugal potential as in the CS approximation, but also treats the rotational energy levels as degenerate, leading to a full decoupling of the angular momenta. In the IOS approximation, the scattering equations reduce to the one-dimensional formalism with the orientation dependence of the intermolecular potential entering only parametrically. The total differential scattering cross section may then be obtained by performing an average over the individual differential cross sections calculated for each orientation. The simplification to the scattering dynamics in the IOS approximation provides a convenient method for the determination of anisotropic intermolecular potential energy surfaces from scattering experiments.

3.5.2 Atom-Symmetric-Top Scattering Formalism

The theory of atom-symmetric top collisions has been discussed in the literature primarily by Green [52, 53], but it follows from the theory of atom-linear molecule collisions first presented by Arthurs and Dalgarno [8].

The total Hamiltonian for an atom-symmetric top collision can be expressed in space-fixed coordinates ($\mathbf{r} = r, \theta, o$), where the collision coordinate r is defined as the distance from the molecular center of mass to the atomic center, and θ, o define the collisional orbital momentum of the atom with respect to the molecule. The atom-symmetric top Hamiltonian is expressed as::

$$\left[-\frac{\hbar^2}{2\mu}\nabla_{\mathbf{r}}^2 + H_{rot.}\left(\hat{R}\right) + V\left(\mathbf{r}, \hat{R}\right) - E - E_{jk}\right] \Psi_{jkl}^{JM}\left(\mathbf{r}, \hat{R}\right) = 0 \qquad (3.59)$$

where $H_{rot.}\left(\hat{R}\right)$ is rigid rotor Hamiltonian of the symmetric-top satisfying free rotor

Schrödinger equation as

$$H_{rot.}\left(\hat{R}\right) \mid jkm\rangle = E_{jk} \mid jkm\rangle \quad \text{with} \quad E_{jk} = \tilde{B}j\,(j+1) + \left(\tilde{A} - \tilde{B}\right) k^2 \,. \tag{3.60}$$

$\tilde{A}$ and $\tilde{B}$ reflect the rotational constants of the principle inertial axes. and the quantum numbers j. k. and m are the total rotational angular momentum. the projection of rotational angular momentum on the body-fixed z' axis. and the projection of the total rotational angular momentum on the space-fixed z axis. respectively. The rotor orientation in the body-fixed frame is given by the Euler angles$(\alpha. \beta. \gamma)$ [6] and the symmetric-top eigenfunctions are expressed in terms of the rotational matrix elements [71] as:

$$\mid jkm\rangle = \left[(2j+1)/8\pi^2\right]^{\frac{1}{2}} \mathcal{D}^{j}_{km}\,(\alpha. \beta. \gamma) \,. \tag{3.61}$$

The general solution to the total Hamiltonian expands the total wavefunction in terms of radial functions $U^{JM}_{jkl}\,(r)$ and total angular momentum eigenfunctions $\mid JMjkl\rangle$ as:

$$\Psi^{JM}_{jkl}\left(\mathbf{r}. \hat{R}\right) = \sum \frac{1}{r} U^{JM}_{jkl}\,(r) \mid JMjkl\rangle \,. \tag{3.62}$$

The total angular momentum ($J = j + l$) is determined by the coupling of rotational and orbital angular momentum functions as :

$$\mid JMjkl\rangle = \sum_{m.m_l} \langle jmlm_l \mid JM\rangle \mid jkm\rangle \mid lm_l\rangle \,. \tag{3.63}$$

with $\langle jmlm_l \mid JM\rangle$ denoting the Clebsch-Gordon vector coupling coefficients [71. 81]. and $\mid lm_l\rangle$ expresses the partial wave functions given by spherical harmonics $Y_{lm_l}\,(\theta. o)$ in spaced-fixed coordinates.

The close-coupled scattering equations are obtained by integration of Equation 3.59 over angular coordinates leading to a set of second order radial wave equation in space fixed coordinates as:

$$\left[\frac{d^2}{dr^2} - \frac{l\,(l+1)}{r^2} + \kappa^2_{j'k'jk}\right] U^{JM}_{jkl}\,(r) =$$
$$\left(2\mu/\hbar^2\right) \sum_{j''k''l''} \langle JMj''k''l'' \mid V\left(\mathbf{r}. \hat{R}\right) \mid JMj'k'l'\rangle U^{JM}_{jkl}\,(r) \tag{3.64}$$

where the wave vector depends on the internal states before and after the collision as:

$$\kappa^2_{j'k'jk} = \left(2\mu/\hbar^2\right)\left(E + E_{jk} - E_{j'k'}\right) \tag{3.65}$$

and $\langle JMj''k''l'' \mid V\left(\mathbf{r}, \hat{R}\right) \mid JMj'k'l'\rangle$ is the potential matrix, which couples the rotational and orbital angular momentum components.

Intermolecular Potential

In most molecular scattering problems, it is convenient to expand the intermolecular potential in real functions which are rotationally invariant to the point group symmetry operations. The actual group symmetries of the unsaturated hydrocarbons are considered in the next chapter. For symmetric-top molecules with a n-fold rotational symmetry axis, the principle moments of inertia in the body-fixed frame may be aligned with the space-fixed z axis by assigning the Euler angles $\alpha = \beta = \gamma = 0$ [6]. Provided that the $x'z'$ axis is also a reflection plane of symmetry, the potential may be expanded in linear combinations of renormalized spherical harmonic functions $C_{\lambda,\mu}(\theta', \phi')$ [54, 52, 111] as:

$$\begin{aligned} V(r, \theta', \phi') &= \sum_{\lambda,\mu} v_{\lambda,\mu}(r)\, \frac{1}{1+\delta_{\mu 0}} \left[C_{\lambda,\mu}(\theta', \phi') + (-1)^{\mu} C_{\lambda,-\mu}(\theta', \phi')\right] \\ &= \sum_{\lambda,\mu} v_{\lambda,\mu}(r)\, P_{\lambda}(\cos\theta') \cos\mu\phi' \,. \end{aligned} \tag{3.66}$$

where the potential has be simplified using the Legendre polynomials.

The advantage gained by expanding the intermolecular potential in functions of the proper rotational symmetry is that the potential matrix may then be integrated analytically using the orthonormality relationships of the spherical harmonic functions. The potential matrix for symmetric top interactions given in Equation 3.64 then becomes:

$$\langle JMj''k''l'' \mid \sum_{\lambda,\mu} v_{\lambda,\mu}(r)\, C_{\lambda,\mu}(\theta', \phi') \mid JMj'k'l'\rangle$$

$$= \sum_{\lambda,\mu} r_{\lambda,\mu}(r)(-1)^{j''+j'+k''-J}[(2j''+1)(2j'+1)(2l''+1)(l'+1)(2\lambda+1)]^{\frac{1}{2}}$$
$$\times \begin{pmatrix} l' & l'' & \lambda \\ 0 & 0 & 0 \end{pmatrix} \begin{pmatrix} j' & j'' & \lambda \\ k' & -k'' & \mu \end{pmatrix} \begin{Bmatrix} j'' & l'' & J \\ l' & j' & \lambda \end{Bmatrix} \tag{3.67}$$

where $\begin{pmatrix} \cdot & \cdot & \cdot \\ \cdot & \cdot & \cdot \end{pmatrix}$ and $\begin{Bmatrix} \cdot & \cdot & \cdot \\ \cdot & \cdot & \cdot \end{Bmatrix}$ denote the 3-J and 6-J symbols [71], respectively.

Collisional S-matrix and Scattering Amplitude

To determine the inelastic transitions and the differential scattering cross sections the asymptotic form of the radial wave functions must be considered. The asymptotic form of the radial wave equation is given by:

$$\begin{aligned} I^{JM}_{jkl}(r) &\sim \delta_{jj'}\delta_{kk'}\delta_{ll'}\exp[-i(\kappa_{jkjk}r - l\pi/2)] - (\kappa_{jkjk}/\kappa_{jkj'k'})^{1/2} \\ &\times S^J(jkl \mid j'k'l')\exp[i(\kappa_{jkj'k'}r - l'\pi/2)] \end{aligned} \tag{3.68}$$

where $S^J(jkl \mid j'k'l') = \langle jkl \mid S^J \mid j'k'l' \rangle$ is the collisional S-matrix. In analogy to the form presented in the single channel quantal theory, the first term represents the initial free plane wave state and the second term expresses the outgoing spherical scattered waves, and the S^J contains all the phase shift information.

The scattering amplitude can expressed in terms of the collisional S-matrix by considering the asymptotic radial solution in the absence of the interaction potential. The general form of the scattering amplitude for the multichannel scattering problem [111, 52] is:

$$\begin{aligned} &F(j'm_{j'} - jm_j \mid \theta, o) = \\ &\left(\frac{\pi}{\kappa_{jk}\kappa_{j'k'}}\right)^{\frac{1}{2}} \sum_{J,l,l'} i^{l-l'+1}(2l+1)^{\frac{1}{2}}(2J+1)(-1)^{j-j'+l'-l} Y_{l'm_{l'}}(\theta, o) \\ &\times T^J(jkl \mid j'k'l') \begin{pmatrix} j & l & J \\ m_j & 0 & M \end{pmatrix} \begin{pmatrix} j' & l' & J \\ m_{j'} & m_{l'} & M \end{pmatrix} \end{aligned} \tag{3.69}$$

where $T^J(jkl \mid j'k'l') = \delta_{jj'}\delta_{kk'}\delta_{ll'} - S^J(jkl \mid j'k'l')$ is the transitional T-matrix.

For the non-state selected experiments where alignment effects are not considered, only the degeneracy averaged differential scattering cross sections are required. By summing over all final $m_{j'}$ states and averaging over all initial states m_j, the degeneracy averaged state-to-state differential scattering cross section is:

$$I(j' \leftarrow j \mid \theta) = \frac{1}{2j+1} \frac{\kappa_{j'k'}}{\kappa_{jk}} \sum_{m_j, m_{j'}} |F(j' m_{j'} \leftarrow j m_j \mid \theta)|^2 . \tag{3.70}$$

3.5.3 *Coupled States (CS) Scattering Approximation*

The coupled states approximation [66, 111, 78] to the close coupled scattering formalism is solved in the body-fixed coordinates, where the body-fixed z' axis stays aligned with the collision direction. The projection of the orbital angular momentum m_l is then zero, enabling the states to labeled by $|JMjk\bar{m}\rangle$, with $\bar{m}$ being the projection of j on the space-fixed z axis, rather than the fully coupled basis $|JMjkl\rangle$. Further, the centrifugal sudden approximation is used to decouple the orbital and rotational angular momentum, therefore, the interaction potential matrix becomes independent of l in the CS approximation. The centrifugal sudden approximation replaces the orbital angular momentum operator by an effective eigenvalue form as:

$$l^2 \approx \hbar^2 \bar{l}\left(\bar{l}+1\right) \tag{3.71}$$

where $\bar{l}$ is an average value over the initial and final states l and l'. The actual choice of $\bar{l}$ can either be the initial, final, or an average value of the orbital angular momentum. Previous calculations for our laboratory have used the l-final CS approximation with sufficient success [124, 121]. The CS approximation is considered valid in the high energy limit where the relative collision energy is much greater than the intermolecular potential well depth, $E/\epsilon \gg 1$. At higher energy, the specific value of the centrifugal potential is less important, and the turning point of the potential is weakly dependent on $\bar{l}$. Under the CS formalism, the radial wave equation becomes:

$$\left[\frac{d^2}{dr^2} - \frac{\bar{l}\left(\bar{l}+1\right)}{r^2} + \kappa^2_{j'k'jk}\right] U^J_{jk\bar{m}}(r) =$$

$$\left(2\mu/\hbar^2\right)\sum_{j''k''}\langle Jj''k''\bar{m}''\mid V\left(\mathbf{r},\hat{R}\right)\mid Jj'k'\bar{m}'\rangle U^{J}_{jk\bar{m}}(r) \qquad (3.72)$$

where the orbital angular momentum l is fully decoupled. Likewise, simplifications to the S-matrix and the scattering amplitude are obtained by removing the l coupling. More detailed discussions of the CS approximation can be found in the literature [101, 66, 78].

3.5.4 *Infinite-Order-Sudden(IOS) Approximation*

In addition to the centrifugal sudden approximation, the IOS approximation also uses the energy sudden approximation [53, 66, 100, 111], which essentially treats the rotational energy levels as degenerate, leading to a full angular momentum decoupling in both the rotational angular momentum and the orbital angular momentum. The IOS approximation is a good approximation when the relative collision energy is large compared to the rotational energy level spacing of the rotor, $E \gg \Delta E_{jk}$. Under the energy sudden approximation, the relative scattering wave vector is approximated by replacing the rotational angular momentum operator by an effective rotational eigenvalue form, $\hat{j}^2 = \bar{B}\hat{j}\,(\hat{j}+1)$. Since the rotational energy contributions are small, the initial relative kinetic energy is appropriate for approximating the wavevector as follows:

$$\kappa^2_{j'k'jk} \rightarrow \bar{\kappa}^2 = \left(2\mu/\hbar^2\right)(E)\ . \qquad (3.73)$$

The potential matrix may then be integrated over the rotor eigenfunctions, making the scattering equations parametrically dependent on the orientation dependence. Under the IOS approximation, the orientation remains fixed during collision process, which is considered to be a good approximation if the relative collision time is small compared to the rotational period of the molecule, $t_{coll} < t_{rot}$. For thermal collisions the average collision time is on the order of a few picoseconds for a particle traversing an assumed intermolecular range of approximately 10 Å. The collision time is fast compared to the rotational periods for the first rotational states of the four hy-

drocarbon molecules as is clearly shown in Table 3.1. Using these criteria, the IOS approximation appears to be a valid method for determining the theoretical scattering cross sections for the molecular systems of concern in this thesis.

Table 3.1: The $j = 0$ Rotational Periods for C_2H_2, C_2H_4, C_3H_4, C_4H_2.

Molecule	$\tilde{B}^a$ cm^{-1}	t_{rot} ps.
C_2H_2	1.17	28
C_2H_4	1.0	33
C_3H_4	0.296	113
C_4H_2	0.146	228

[a]Rotational Constants from refs. [98, 72, 75, 79]

Using the energy sudden approximation into CS formalism, the radial wave equation for the IOS approximation is given by:

$$\left[\frac{d^2}{dr^2} - \frac{l\left(l+1\right)}{r^2} + \kappa^2\right] U_{jl}^{JM}(r \mid \theta', o') = \left(2\mu/\hbar^2\right) V(r \mid \theta', o')\, U_{jl}^{JM}(r \mid \theta', o') \ . \tag{3.74}$$

indicating the parametric orientation dependence of the atom with respect to the rotor by the angles θ' and o'.

The asymptotic solution to the radial wave equation gives the orientation dependent S-matrix, which contains all the information on the phase shifts as follows:

$$S^l(\kappa \mid \theta', o') = \exp\left[2i\eta_l(\kappa \mid \theta', o')\right] \ . \tag{3.75}$$

In the IOS formalism, the S-matrix is expanded in the same angular functions as the intermolecular potential. Using the same renormalized spherical harmonics as

before, the S-matrix [53] expressed as:

$$S^l(\kappa \mid \theta', o') = \sum_{\lambda,\mu} S^l_{\lambda\mu}(\kappa)\, C_{\lambda,\mu}(\theta', o') \ . \tag{3.76}$$

where the expansion coefficients are determined using the orthnormality of the spherical harmonic functions as:

$$S^l_{\lambda\mu}(\kappa) = \int_0^{2\pi} do' \int_{-1}^{1} d(\cos\theta')\, C_{\lambda,\mu}(\theta', o')\, S^l(\kappa \mid \theta', o') \ . \tag{3.77}$$

The IOS S-matrix[100, 53] is then evaluated directly by integration over the rotor eigenfunctions $\mid jkm)$ giving:

$$\begin{aligned} S^l_{IOS} \ &= \ (-1)^{k'+m'} \left[(2j'+1)(2j+1)(2\lambda+1)\right]^{\frac{1}{2}} \\ &\times \sum_{\lambda,\mu} S^l_{\lambda\mu}(\kappa) \begin{pmatrix} j' & \lambda & j \\ k' & \mu & -k \end{pmatrix} \begin{pmatrix} j' & \lambda & j \\ m' & 0 & -m \end{pmatrix} \ . \end{aligned} \tag{3.78}$$

Using the form of the asymptotic scattering amplitude, the IOS total differential scattering cross section is then determined averaging over the orientation dependence $\theta' o'$ dependence [100], which is given by:

$$I_{IOS}(\theta) = \frac{1}{4\pi} \int_0^{2\pi} do' \int_{-1}^{1} I(\theta|\theta', o')\, d(\cos\theta') \tag{3.79}$$

where the individual differential scattering cross sections for each orientation are expressed using the single channel result for the partial wave phase shifts. The integrand in the IOS total differential scattering equation is:

$$I(\theta \mid \theta', o') = \left| \frac{1}{2ik} \sum_{l=0}^{\infty} (2l+1) \left(e^{2i\eta_l(\theta', o')} - 1 \right) P_l(\cos\theta) \right|^2 \ . \tag{3.80}$$

The IOS approximation provides a simplified procedure for determining the total differential scattering cross sections, while retaining the scattering features due to the anisotropic intermolecular forces. Using the single channel results and the JWKB and Born approximations for calculating the phase shifts, the theoretical scattering cross sections may be calculated efficiently. The orientational averaging of the individual

single channel cross sections is performed numerically using various quadratures. A Gauss-Legendre method [2. 6] is most suitable for the Legendre polynomials expressed in θ'. while a Gauss-Chebyshev procedure [2. 6] is better for the $\cos \mu o'$ functions.

The convergence of the numerical quadratures are tested by increasing the number of points in the integrations. Approximately 32 points were sufficient for the Gauss-Legendre quadrature. while faster convergence for the Gauss-Chebyshev quadrature was obtained with only 5-6 points. Further. a reduction in the numerical effort can be obtained by taking into account the symmetries of the intermolecular potential [97]. For ethylene and allene. the integrations can be carried out using only the first quadrant ($0-\pi/2$ in θ' and $0-\pi/2$ in o'). while acetylene and diacetylene. being linear molecules. only require integration over $0-\pi/2$ in θ' and are independent of o'. In test calculations for ethylene and allene interactions. the fitting the experimental data was observed to be quite insensitive to the o' angle dependence in the intermolecular potential. therefore the analysis of these systems assumed that the scattering cross sections were independent of o'.

The total integral IOS scattering cross section is determined the integration of the IOS differential cross section over all scattering angles.

$$I_{IOS} = 2\pi \int I_{IOS}(\theta)\, d(\cos\theta) \ . \tag{3.81}$$

In general. a single. total integral cross section for each orientation may be calculated using Equation 3.32. The total IOS integral cross section is then determined by performing an average over all orientations as was done for the IOS differential scattering cross section.

Chapter 4

INTERMOLECULAR POTENTIALS

4.1 Introduction

Previous chapters presented the total differential scattering cross sections and the theory required to determine the underlying potential energy surfaces of the atom - molecule and diatom-molecule systems. For the most part, the scattering theory was discussed in terms of spherical potential models. However, the accurate calculation of the total differential scattering cross sections requires anisotropic potential energy surfaces. Under the IOS approximation of the multichannel scattering problem, the scattering dynamics are essentially reduced to a single channel calculation, where individual elastic cross sections for a number of orientations are calculated and then averaged to determine the total differential scattering cross section. This simplification of the scattering dynamics provides a suitable means for the efficient analysis of experimental cross sections while also maintaining a high degree of accuracy.

The input to the IOS calculation is an anisotropic intermolecular potential which depends not only upon the relative distance of separation, but also upon angular coordinates that express the relative orientation between the interacting molecules. In many theoretical and experimental studies of atom-molecule collisions and van der Waals cluster dynamics, it is usually advantagous to expand the intermolecular potential in terms of spherical harmonic functions which reflect the proper rotational symmetries of the interacting monomers. For example, in the scattering formalism, the expansion of the potential in spherical harmonic functions allows the potential coupling matrix elements to be easily evaluated, since integration over the angular

coordinates may be performed analytically.

The determination of accurate potential models requires consistent agreement with the correct theoretical behavior at short, long, and intermediate ranges. The true form of the anisotropic intermolecular potential is based on the knowledge gained from studies of atomic interactions [74]. For two groundstate closed-shell atoms, the interaction potential is repulsive at short range and attractive at long range. The repulsive interaction arises from the exchange and coloumbic forces caused when electronic wavefunctions overlap. So as not to violate the Pauli exclusion principle, electrons in the two atoms tend to avoid one another in space, leading to the improper shielding of positively charged nuclei. Since the overlap area of the electronic wavefunctions decreases exponentially with distance, the repulsive energy is expected to be exponential with distance as well. The long range attraction of the intermolecular potential for two atoms results from dispersion forces. The correlated fluctuating electronic distributions in the two atoms produce induced dipole-induced dipole moment and higher order induced moment interactions. Theoretical models based on second order perturbation theory, predict the long range interaction to follow a inverse power series in the radial coordinate; i.e. $V(r) \propto -1/r^n$ where $n = 6, 8, \ldots$.

For atom-molecule and diatom - molecule interactions, the intermolecular potential is a function of the relative orientation between the molecules. The short range repulsion remains essentially exponential for a particular orientation, but the repulsive parameter may be softer or harder in various orientations depending on the particular molecular structure. Using an atom-C_2H_2 interaction as an example, a side-on approach primarily involves the interaction of the atom with the π electron cloud, while an end-on approach involves the interaction of the atom with a terminal hydrogen. Also, the long range attraction will have an orientation dependence as well. The dispersion contributions are anisotropic due to the difference in polarizabilities parallel and perpendicular to the molecular symmetry axis.

Interactions between molecules at long range also have contributions from induc-

tion and electrostatic forces in addition to dispersion. The electrostatic and induction interactions have orientational symmetries by nature of the definition of multipolar forces [51]. The electrostatic contributions arise from the interaction between the inherent charge distributions of the molecule resulting in permanent multipole–permanent multipole interactions. The lowest multipole orders being dipole-dipole, dipole-quadrupole, and quadrupole-quadrupole moment interactions. The induction energy results from the distortion of the electron cloud distribution of one molecule by the permanent multipole moments of the other molecule. The electric field established by the permanent multipole moments of one molecule induces dipole, quadrupole, and higher order moments in the adjacent molecule. In general, the long range interaction potential can be expressed as the sum of separate dispersion, induction, and electrostatic terms [118, 74] as follows:

$$V_{tot}(R,\theta,o) = V_{elect.}(R,\theta,o) + V_{ind.}(R,\theta,o) + V_{disp.}(R,\theta,o) \ . \qquad (4.1)$$

For two neutral nonpolar closed-shell molecules, the interaction energy is dominated by the dispersion energy. For most part, the induction and electrostatic energy contributions are significantly smaller and can be neglected. The hydrocarbons and N_2 and H_2 all have permanent quadrupole moments. NO and CO have small permanent dipole moments in addition to permanent quadrupole moments. In general, the orientation dependence of the diatomic molecules has been neglected, treating them as structureless spherical partners. The anisotropy of the interactions is more attributable to the larger, more polarizable unsaturated hydrocarbon species C_2H_2, C_2H_4, C_3H_4, and C_4H_2. The presence of the π-electrons in C_2H_2, C_2H_4, C_3H_4, and C_4H_2 leads to increasingly larger polarizability anisotropies for these molecules, and the polarizability anisotropy plays a significant role in determining the anisotropic dispersion energy contributions of these systems. This chapter describes the developement of anisotropic potential energy surfaces that were used to fit the atom-molecule and diatom-molecule scattering systems presented in this thesis.

Section 4.2 describes the spherical model potentials which provide the basis for the development of the anisotropic potential energy surfaces. The orientation dependent potentials are discussed in Section 4.3. Section 4.4 describes the development of the anisotropic C_6 and C_8 dispersion coefficients for atom-linear molecule interactions. Also presented are the electrostatic, induction, and dispersion long range coefficients for diatom-molecule interactions.

4.2 *Spherical Potentials*

The development of the anisotropic potential energy surfaces are based on spherical potential models which have been successful in describing the solid, liquid, and gas properties of atomic rare gas systems [9]. The form of the spherical models have both repulsive short range and attractive long range contributions. In general, one-dimensional models are characterized in terms of the parameters, ϵ and r_m. The well depth, ϵ, defines the minimum interaction energy at the radial minimum position, r_m. In addition, other parameters may be added to the model potentials to adjust both the repulsive energy as well as the of shape of the potential well. Several functional forms for describing the interaction energy appear in the literature [59, 51, 74]. Two basic model potentials of various complexity were used to analyze the scattering data presented in this thesis, a simple Lennard-Jones N-6 model and a more sophisticated Barker potential model.

4.2.1 Lennard-Jones Potential

The Lennard-Jones (LJ) potential is a common model potential that is used primarily to gain a rough estimate of the interaction energy. Many of the combination rules for atomic systems [59] and the pairwise potential models [103] are based on such simplified models. The Lennard-Jones N-6 potential in reduced parameters is given

by:

$$V^*(r^*) = \epsilon\left\{\left(\frac{6}{n-6}\right)r^{*\,-n} - \left(\frac{n}{n-6}\right)r^{*\,-6}\right\} \tag{4.2}$$

where $r^* = r/r_m$, and n is power of the repulsive contribution, which is chosen mostly for convenience. If $n = 12$, the usual LJ 12-6 potential is obtained. The dispersion coefficient can be expressed in terms of the other parameters by $C_6 = n\epsilon r_m^6/(n-6)$. In general, the LJ model tends to over estimate the C_6 term, since it is a strong dependent on the size parameter. The parameters, n, ϵ, and r_m are adjustable in the LJ model.

4.2.2 Barker Potential

A more realistic expression of the interaction energy in both the repulsive and attractive regions is given by the Barker model. Previous studies have used the Barker model in the analysis of both isotropic [12, 11] and anisotropic systems [121, 124]. The Barker potential expressed in reduced parameters is:

$$V^*(r^*) = \epsilon\left\{\exp[\alpha(1-r^*)]\sum_{i=1}^{2}A_i(r^*-1)^i - \sum_{j=0}^{2}\frac{C_{2j+6}^*}{(\delta+r^*)^{2j+6}}\right\} \tag{4.3}$$

where $r^* = r/r_m$ and $C_{2j+6}^* = C_{2j+6}/\epsilon\, r_m^{2j+6}$. α is the exponential decay parameter in the repulsive part of the potential, and A_2 increases the width of the potential well, while A_1 can be expressed in terms of the other parameters. δ is a small fixed value used to avoid a singularity at $r = 0$. The dispersion coefficients, C_6 and C_8, are held fixed and can be found in the literature, or estimated from combination rules and atomic polarizabilities. The adjustable parameters in the Barker model are α, A_2, ϵ, and r_m.

4.3 Anisotropic Models

The anisotropic potentials depend on the intermolecular separation and the relative orientation between molecules. In general, it is convenient to expand the intermolec-

ular potential in terms of real spherical harmonic functions that are invariant to molecular symmetry point group operations. For atom - symmetric top molecule interactions, where the top molecule has a $n > 2$ - fold symmetry axis and a plane of reflection symmetry, the body-fixed axes may be aligned with space-fixed axes to give real expansion functions [52, 54]. If the n-fold symmetry axis is placed along the z space-fixed axis and xz plane corresponds to the reflection plane, the potential can be described in terms of a linear combination of renormalized spherical harmonic functions, $C_{\lambda,\mu}(\theta,o)$ [118] , as follows:

$$\begin{aligned} V(r,\theta,o) &= \sum_{\lambda,\mu} v_{\lambda,\mu}(r) \frac{1}{1+\delta_{\mu 0}} [C_{\lambda,\mu}(\theta,o) + (-1)^{\mu} C_{\lambda,-\mu}(\theta,o)] \\ &= \sum_{\lambda,\mu} v_{\lambda,\mu}(r) P_{\lambda}(\cos\theta) \cos\mu o \end{aligned}$$

where the expression has been simplified in terms of the Lengendre polynomials, $P_{\lambda}(\cos\theta)$, and the $v_{\lambda,\mu}(r)$ are the radially dependent potential expansion coefficients.

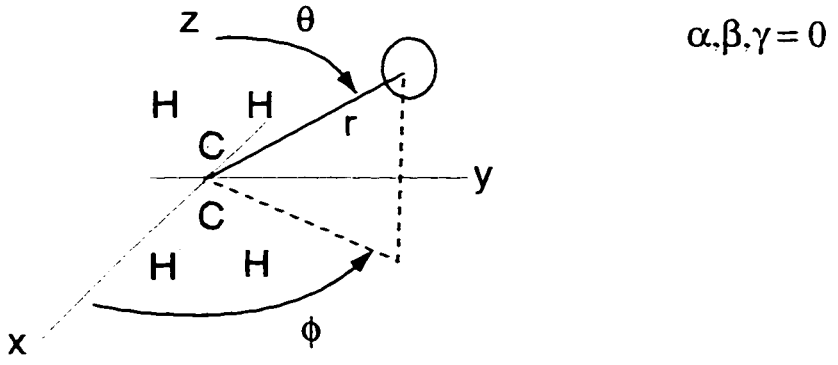

Figure 4.1: Space fixed coordinate representation for atom - ethylene interactions. The xz plane is a plane of symmetry.

Figure 4.1 shows the space-fixed coordinate system used for atom-ethylene interactions. The body-fixed coordinates of the ethylene subunit have been aligned with the spaced fixed coordinates by setting the Euler angles $\alpha, \beta, \gamma = 0$. The intermolecular distance, r, is defined from the ethylene center of mass to the atomic center, and

the orientation of the radial vector is defined by the angles θ and o. θ is the angle between the radial vector and the z space-fixed axis, and o is the angle between the projection of the radial vector on to the xy plane and the positive x space-fixed axis.

For ethylene of the D_{2h} point group, the C_2 molecular symmetry axis is aligned with the z axis and the molecule lies in the yz plane. The potential may then be expanded in even λ and μ terms by:

$$\begin{aligned} V(r,\theta,o) &= v_{0,0} + v_{2,0}P_2(\cos\theta) \\ &+ v_{2,2}P_2(\cos\theta)\cos 2o + v_{4,0}P_4(\cos\theta) \\ &+ v_{4,2}P_4(\cos\theta)\cos 2o + v_{4,4}P_4(\cos\theta)\cos 4o + \ldots \end{aligned} \tag{4.4}$$

For allene of the D_{2d} point group, the C_2 molecular symmetry axis is also aligned with the z axis and the hydrogen atoms lie in diagonal planes intersecting the yz plane. The potential may then be expanded in even and odd λ and even μ terms as:

$$\begin{aligned} V(r,\theta,o) &= v_{0,0} + v_{1,0}P_1(\cos\theta) \\ &+ v_{2,0}P_2(\cos\theta) + v_{2,2}P_2(\cos\theta)\cos 2o \\ &+ v_{3,0}P_3(\cos\theta) + v_{3,2}P_3(\cos\theta)\cos 2o + \ldots \end{aligned} \tag{4.5}$$

For the linear molecules, acetylene and diacetylene, with the $D_{\infty h}$ point group, the molecular symmetry axis is aligned with z axis, and the potential expansion is given in even λ terms of the Legendre polynomials:

$$\begin{aligned} V(r,\theta) &= v_{0,0} + v_2P_2(\cos\theta) \\ &+ v_4P_4(\cos\theta) + v_6P_6(\cos\theta) + \ldots \end{aligned} \tag{4.6}$$

Rather than obtain a fit to the potential coefficients, $v_{\lambda,\mu}$, a method which is known to converge slowly, it is better, and perhaps more intuitive, to expand the potential parameters, ϵ and r_m, of the spherical potential models in the same angular functions. In a first approximation, the o angular dependence of the interactions was neglected

on the assumption that the all the hydrocarbons, regardless of their symmetry, are cylindrically shaped and can be treated as essentially linear molecules[1]. The potential parameters r_m and ϵ expanded in Legendre polymonial are then as follows:

$$\begin{aligned} \epsilon(\theta) &= \epsilon_0 + \epsilon_2 P_2(\cos\theta) + \epsilon_4 P_4(\cos\theta) + \dots \\ r_m(\theta) &= r_{m0} + r_{m2} P_2(\cos\theta) + r_{m4} P_4(\cos\theta) + \dots \end{aligned} \tag{4.7}$$

The dispersion coefficients are also anisotropic and can be expanded in the same Legendre polynomial functions accordingly:

$$\begin{aligned} C_6(\theta) &= C_{60} + C_{62} P_2(\cos\theta) \\ C_8(\theta) &= C_{80} + C_{82} P_2(\cos\theta) + C_{84} P_4(\cos\theta) \ . \end{aligned} \tag{4.8}$$

where $C_{60}, C_{62}, C_{80}, C_{82}$, and C_{84} account for the dipole-dipole and dipole-quadrupole dispersion terms. For atom-linear molecule interactions, the anisotropic coefficients are determined using combination rules, atomic and molecular properties, and a theoretical procedure outlined in the literature [93].

4.4 *Dispersion Coefficients for Intermolecular Potentials*

4.4.1 Isotropic Dispersion

The dispersion energy represents the largest contribution to the interaction potential at long range. For identical closed shell atomic interactions, the dispersion coefficients are purely isotropic. In general, the C_6 term may be estimated using the well known relationship developed by London[64, 3] as follows:

$$C_{6,aa} = \frac{3}{4} \alpha_{0,a}^2 I_a \tag{4.9}$$

where α_a is the static atomic polarizability and I_a is the atomic ionization potential.

[1] A reasonable approximation if the light H atoms are neglected and only the linear C – C bonding framework is considered, which has the appropriate symmetry $\lambda = 0, 2, 4, \dots$.

We can use the same relationship to estimate the isotropic contribution for two non-identical molecules. If we consider the interaction of an atom "a" with a linear molecule "b", the mixed system, isotropic C_6 dispersion coefficient is given by:

$$C_{6,ab} = \frac{3}{2}\bar{\alpha}_{0,a}\bar{\alpha}_{0,b}\frac{I_a I_b}{I_a + I_b} \tag{4.10}$$

where the variables represent the same properties as before, except the average molecular static polarizability has been considered.

A more common form of Equation 4.10 is the geometric combination rule [31], expressed as:

$$C_{6,ab} = \sqrt{C_{6,aa}C_{6,bb}}\,. \tag{4.11}$$

Equation 4.11 is generally preferred if the isotropic C_6 terms for the pure systems are known. These have been determined by various experimental and theoretical investigations for the rare gases (He, Ne, and Ar) [93] and diatomic molecules (H_2, N_2, CO, and NO) [87, 95, 92]. However in the case of the larger hydrocarbon molecules, only the isotropic dipole-dipole dispersion coefficients for C_2H_2 and C_2H_4 are available in the literature [3]. To determine the isotropic C_6 terms for C_3H_4 and C_4H_2, Equation 4.9 was used to develop a scaling relationship. Since C_2H_4 and C_3H_4 are similar double $C-C$ bonded hydrocarbon species, a reasonable estimate for C_3H_4 was obtained in terms of the C_2H_4 C_6 value by:

$$\frac{C_{6,C_3H_4}}{C_{6,C_2H_4}} = \frac{\bar{\alpha}^2_{0,C_3H_4}}{\bar{\alpha}^2_{0,C_2H_4}}\frac{I_{C_3H_4}}{I_{C_2H_4}} \tag{4.12}$$

Similarly, C_2H_2 and C_4H_2 are both triple $C-C$ bonded linear molecules and the isotropic C_6 dispersion coefficient for C_4H_2 was estimated by:

$$\frac{C_{6,C_4H_2}}{C_{6,C_2H_2}} = \frac{\bar{\alpha}^2_{0,C_4H_2}}{\bar{\alpha}^2_{0,C_2H_2}}\frac{I_{C_4H_2}}{I_{C_2H_2}} \tag{4.13}$$

The C_6 scaling law was tested by using the molecular properties for CO_2 and C_2H_2. The estimated C_6 value for CO_2 was found to be in reasonable agreement (5-10%) with more accurate values from the literature [93].

Table 4.1: Atomic and diatomic input properties for estimating atom-molecule dispersion series for Barker potentials. All units are atomic units.

	α_0	C_6	C_8	C_8/C_6	Θ^a	μ^b
He	1.383	1.461	14.17	9.69		
Ne	2.668	6.882	73.87	10.73		
Ar	11.08	66.89	1176.4	17.59		
Kr	16.74	135.1	2580.9	19.10		
Xe	27.29	281.2	7033.5	25.02		
H_2	5.53	12.14	215.2	17.72	0.475	
N_2	11.7	73.4	1825	24.86	-1.13	
CO	13.4	88.4	2616	29.6	-1.85	0.044
NO	11.7	69.0	1725	25.0	-1.33	0.062

[a]Quadrupole moments from ref. [117].

[b]Dipole moments from ref. [51].

Table 4.2: Molecular input properties of hydrocarbon molecules used in estimating the anisotropic dispersion series for Barker potentials. All units are atomic units.

Molecule	$\bar{\alpha}_0$	$\alpha_\perp$	$\alpha_\parallel$	C_6	C_8	Θ_{zz} [a]	$I.P.$ [b]
C_2H_2	23.77	19.5	32.3	231	5585	2.31	0.419
C_2H_4	28.75	24.6	37.1	321	8772	1.21	0.386
C_3H_4	42.52	31.1	65.45	660	23862	3.25	0.367
C_4H_2	49.2	30.6	86.4	900	36933	9.45	0.375

[a]Quadrupole moments from ref. [117, 51].

[b]Ionization Potentials from CRC [105].

Estimates for the isotropic C_8 dispersion coefficients for the atom-molecule interactions were obtained from observations based the atomic C_8/C_6 ratios. To a reasonable degree, the isotropic ratios of the C_8/C_6 for He, Ne, Ar, Kr, and Xe when plotted versus their atomic polarizabilties[2] were observed to follow the linear trend:

$$\frac{C_8}{C_6} = x + y\,(\bar{\alpha}_0) \tag{4.14}$$

where x and y are the fit parameters. The best fit terms in this model were found to be $x = 8.9$ and $y = 0.64$. Using Equation 4.14, the average polarizablities, and the isotropic C_6 terms determined above, the C_8 contributions of the hydrocarbon molecules were estimated. Table 4.1 shows the atomic input properties as well as the C_6 and C_8 values. Also shown are the molecular properties and the C_6 and C_8 terms for the diatomic molecules compiled from various sources. The C_6 and C_8 coefficients for the hydrocarbons are given in Table 4.2 along with the hydrocarbon molecular properties.

[2]All values from ref. [93].

4.4.2 *Anisotropic Dispersion Coefficients*

The isotropic dispersion coefficients required the use of the average static polarizabilities of the hydrocarbon molecules. In comparison, the determination the anisotropic dispersion coefficients, requires the parallel and perpendicular polarizability components of the molecules. For linear and symmetric top molecules, the average static polarizability can expressed in terms of polarizability parallel and perpendicular to the molecular symmetry axis. The average static polarizability is given by:

$$\bar{\alpha}_0 = \frac{1}{3}\left(\alpha_{\parallel} + 2\alpha_{\perp}\right) \tag{4.15}$$

where $\alpha_{\parallel}$ and $\alpha_{\perp}$ are the parallel and perpendicular polarizability components, respectively.

Information from light scattering studies were used to determine the polarizabilty anisotropy, ρ, for most of the molecules [19]. The polarizability anisotropy due to the parallel, $\alpha_{\parallel}$, and perpendicular, $\alpha_{\perp}$, polarizabilities is defined by:

$$\rho = \alpha_{\parallel} - \alpha_{\perp} \, . \tag{4.16}$$

Using Equations 4.15 and 4.16, the individual perpendicular and parallel polarizability components can be expressed in terms of the experimental quantities, $\bar{\alpha}_0$ and ρ, as:

$$\alpha_{\perp} = \frac{1}{3}(3\bar{\alpha}_0 - \rho) \qquad \alpha_{\parallel} = \frac{1}{3}(3\bar{\alpha}_0 + 2\rho) \tag{4.17}$$

As will be presented later, the important quantity for determining the anisotropic coefficients C_{62},C_{82}, and C_{84} is the polarizability ratio , $\alpha_{\perp}/\alpha_{\parallel}$. Table 4.2 shows the derived $\alpha_{\parallel}$ and $\alpha_{\perp}$ values for the hydrocarbon molecules using the information from the literature.

4.4.3 *Atom - Linear Molecule Interactions*

A method developed by Pack [93] for atom -linear molecule systems was used to estimate the mixed dispersion series for all the scattering systems presented in this

thesis. In general this procedure depends on the atomic polarizabilties. the pure isotropic dispersion coefficients of the atoms and molecules. and the molecular polarizabilty anisotropy ratios of the hydrocarbons. Small induction contributions to the second order energy are also included. Pack expresses the anisotropic van der Waals coefficients C_{60}. C_{62}. C_{80}. C_{82}. and C_{84}. in terms of the various properties and rather complicated functions. known as the oscillator strength sums. Only a brief outline of this method is presented here. Table 4.3 shows the estimated anisotropic dispersion series for rare gas atom - hydrocarbon molecule interactions.

The dispersion and induction contributions to the C_6 and C_8 coefficients are treated separately. The C_6 terms are given by:

$$\begin{aligned} C_{60,ab} &= C_{60,ab}(dis) + C_{60,ab}(ind) \\ C_{62,ab} &= C_{62,ab}(dis) + C_{62,ab}(ind) \end{aligned} \tag{4.18}$$

Simliarly. the C_8 terms are given by:

$$\begin{aligned} C_{80,ab} &= C_{80,ab}(dis) + C_{80,ab}(ind) \\ C_{82,ab} &= C_{82,ab}(dis) + C_{82,ab}(ind) \\ C_{84,ab} &= C_{84,ab}(dis) + C_{84,ab}(ind) \end{aligned} \tag{4.19}$$

C_6 Induction Terms

For atom - nonpolar linear molecule interactions. the C_6 terms have no contributions from the induction energy.

C_{60}

$$C_{60,ab}(ind) = 0 \tag{4.20}$$

C_{62}

$$C_{62,ab}(ind) = 0 \tag{4.21}$$

C_8 Induction Terms

For the C_8 terms. the induction terms result from the interaction of the permanent quadrupole moment of the molecule. Θ_b. and the polarizability of the atom. α_a.

C_{80}

$$C_{80,ab}(ind) = 2D_{35,0}(ind) + D_{44,0}(ind) \tag{4.22}$$

$$D_{35,0}(ind) = 0 \quad \text{and} \quad D_{44,0}(ind) = \frac{3}{2}\Theta_b^2\alpha_a \tag{4.23}$$

C_{82}

$$C_{82,ab}(ind) = 2D_{35,2}(ind) + D_{44,2}(ind) \tag{4.24}$$

$$D_{35,2}(ind) = 0 \quad \text{and} \quad D_{44,2}(ind) = \frac{12}{7}\Theta_b^2\alpha_a \tag{4.25}$$

C_{84}

$$C_{84,ab}(ind) = 2D_{35,4}(ind) + D_{44,4}(ind) \tag{4.26}$$

$$D_{35,4}(ind) = 0 \quad \text{and} \quad D_{44,4}(ind) = \frac{9}{7}\Theta_b^2\alpha_a \tag{4.27}$$

C_6 Dispersion Terms

The isotropic term C_{60} is determined from the geometric combination rule in equation 4.11. The ratio of C_{60}/C_{62} is expressed in terms of the polarizability ratio. $\alpha_r = \alpha_\perp/\alpha_\parallel$.

C_{60}

$$C_{60,ab}(dis) = \sqrt{C_{60,aa}(dis)\,C_{60,bb}(dis)} \tag{4.28}$$

C_{62}

$$\frac{C_{62,ab}(dis)}{C_{60,ab}(dis)} = \frac{1}{2}\left[\frac{1-\alpha_r}{1+2\alpha_r} + \frac{1-(\alpha_r)^{\frac{1}{4}}}{1+2(\alpha_r)^{\frac{1}{4}}}\right] \tag{4.29}$$

where $\alpha_r = \alpha_\perp/\alpha_\parallel$.

C_8 Dispersion Terms

The isotropic C_{80} term for the mixed systems is obtained from an average of the C_8/C_6 ratios of the pure interactions and the isotropic C_{60} term. The anisotropic

terms C_{82} and C_{84} are expressed in complicated expressions of the oscillator strength sums, $S_i(k)$, and the anisotropy ratio of parallel and perpendicular excitation oscillator frequencies, $\omega = \omega_{\parallel}/\omega_{\perp} = \sqrt{\alpha_r}$.

C_{80}

$$C_{80,ab}(dis) = 2D_{35,0}(dis) + D_{44,0,1}(dis) + D_{44,0,2}(dis) \tag{4.30}$$

$$D_{35,0}(disp) = 0 \tag{4.31}$$

$$D_{44,0,1}(dis) = \frac{1}{2} C_{60,ab} \frac{C_{80,bb}}{C_{60,bb}} \tag{4.32}$$

$$D_{44,0,2}(dis) = \frac{1}{2} C_{60,ab} \frac{C_{80,aa}}{C_{60,aa}} \tag{4.33}$$

C_{82}

$$C_{82,ab}(dis) = 2D_{35,2}(dis) + D_{44,2,1}(dis) + D_{44,2,2}(dis) \tag{4.34}$$

$$D_{35,2}(dis) = \frac{12}{7}\left[\frac{1}{2}(\epsilon(-2) + \epsilon(-3/2))\right] D_{44,0,2}(dis) \tag{4.35}$$

$$D_{44,2,1}(dis) = \frac{4}{5} \frac{C_{62,ab}}{C_{60,ab}} D_{44,0,1}(dis) \tag{4.36}$$

$$D_{44,2,2}(dis) = \frac{8}{7}\left[\frac{1}{2}(b(-2) + b(-3/2))\right] D_{44,0,2}(dis) \tag{4.37}$$

where

$$\epsilon(k) = \frac{S_3(k) + 2\left(\frac{2}{3}\right)^{\frac{1}{2}} S_4(k)}{1 + 2S_1(k) + 2S_2(k)} \quad \text{and} \quad b(k) = \frac{1 + S_1(k) - 2S_2(k)}{1 + 2S_1(k) + 2S_2(k)} \tag{4.38}$$

C_{84}

$$C_{84,45}(dis) = 2D_{35,4}(dis) + D_{44,4,2}(dis) \tag{4.39}$$

$$D_{35,4}(dis) = \frac{20}{21}\left[\frac{1}{2}(g(-2) + g(-3/2))\right] D_{44,0,2}(dis) \tag{4.40}$$

$$D_{44,4,2}(dis) = \frac{6}{7}\left[\frac{1}{2}(d(-2) + d(-3/2))\right] D_{44,0,2}(dis) \tag{4.41}$$

where

$$g(k) = \frac{S_3(k) - \left(\frac{3}{2}\right)^{\frac{1}{2}} S_4(k)}{1 + 2S_1(k) + 2S_2(k)} \quad \text{and} \quad d(k) = \frac{1 - \frac{4}{3}S_1(k) + \frac{1}{3}S_2(k)}{1 + 2S_1(k) + 2S_2(k)} \tag{4.42}$$

Oscillator Strength Sums

$$\begin{aligned} S_1(k) &= \frac{3}{4}\left(\frac{1}{2\omega}\right)^k \frac{(1+\omega)^{1+k}}{1 + 1/2(\omega^{1-k})} \qquad S_2(k) = \frac{3}{2}\frac{\omega^{1-k}}{1 + 1/2(\omega^{1-k})} \\ S_3(k) &= \frac{3}{4}\frac{1-\omega}{2^k(1 + 1/2\omega^{1-k})} \qquad S_4(k) = \frac{1}{2}\sqrt{\frac{3}{2}}\frac{1}{2\omega^k}\frac{1-\omega}{2^k(1 + 1/2\omega^{1-k})} \end{aligned} \tag{4.43}$$

where $\omega = \sqrt{\alpha_r}$, the square root of the ratio of the perpendicular and static polarizabilities.

Table 4.3: Anisotropic dispersion series for the rare gas-molecule interaction potentials. All units are atomic units.

System	C_{60}	C_{62}	C_{80}	C_{82}	C_{84}
$He - C_2H_4$	22	2.7	404	237	22
$He - C_3H_4$	31	7.3	734	858	144
$He - C_4H_2$	36	12	953	1612	364
$Ne - C_2H_2$	38	6.0	728	519	67
$Ne - C_2H_4$	47	5.9	900	516	46
$Ne - C_3H_4$	67	16	1623	1863	308
$Ne - C_4H_2$	79	26	2098	3497	781
$Ar - C_2H_4$	147	18	3315	1669	150
$Ar - C_3H_4$	210	49	5825	5993	998
$Ar - C_4H_2$	245	81	7471	11226	2509

4.4.4 Diatom - Linear Molecule Interactions

The diatom - hydrocarbon molecule systems have electrostatic and induction contributions to total long range interaction energy in addition to the dispersion energy. Expressions for the orientation dependence of the electrostatic and induction interactions have been previously derived by Buckingham [30]. They are reproduced here to give an indication of the magnitude of the electrostatic and induction terms in comparison to the dispersion energy contributions.

Electrostatic Terms

The electrostatic terms consist of permanent multipole - multipole interactions. The dipole-quadrupole and quadrupole-quadrupole interactions are given by:

$$\begin{aligned} V_{elec} &= \frac{3}{2}\frac{\mu_a \Theta_b}{r^{-4}}\left[\cos\theta_a\left(3\cos^2\theta_b - 1\right)\right] \\ &+ \frac{3}{4}\frac{\Theta_a \Theta_b}{r^{-5}}\Big[1 - 5\cos^2\theta_a - \cos^2\theta_b + 17\cos^2\theta_a\cos^2\theta_b \\ &+ 2\sin^2\theta_a\sin^2\theta_b\cos^2 o + 16\sin\theta_a\cos\theta_a\sin\theta_b\sin\theta_b\cos o\Big]. \end{aligned} \tag{4.44}$$

Induction Terms

The induction terms consist of permanent multipole moment - induced dipole moment interactions. The permanent dipole-induced dipole moment and permanent quadrupole -induced dipole moment interactions are given by:

$$\begin{aligned} V_{ind} &= -\frac{1}{2}\frac{\alpha_b \mu_a^2}{r^{-6}}\left[3\cos^2\theta_a + 1\right] \\ &+ -\frac{1}{6}\frac{\left(\alpha_{\|} - \alpha_{\perp}\right)\mu_a^2}{r^{-6}}\Big[12\cos^2\theta_a\cos^2\theta_b + 3\sin^2\theta_a\sin^2\theta_b\cos^2 o \\ &- 3\cos^2\theta_a - 1 + 12\sin\theta_a\cos\theta_a\sin\theta_b\cos\theta_b\cos o\Big]. \end{aligned} \tag{4.45}$$

Table 4.4 shows the estimated electrostatic, induction, and dispersion coefficients for diatomic molecule - hydrocarbon molecule interactions. The dispersion contributions which have been determined by the same method outlined for the atom-molecule interactions are by far the largest contributions to the total interaction energy at long range. The induction contributions are relatively small and can be ignored for the most part. The electrostatic contributions are larger than the induction terms, but still quite small in magnitude compared to the dispersion contributions. In the analysis of the scattering data, the electrostatic interactions have been ignored. However, it is important to note that the $1/r^4$ and $1/r^5$ dependence of the electrostatic dipole-quadrupole, and quadrupole-quadrupole interactions will affect the total interaction potential for intermediate ranges because they fall off less quickly than $1/r^6$. If the orientational average of the diatom is considered, since in the experiments , all orien-

Table 4.4: Electrostatic, induction, and dispersion series coefficients for diatomic-molecule interaction potentials. All units are atomic units.

	Dispersion					Electrostatic		Induction	
System	C_{60}	C_{62}	C_{80}	C_{82}	C_{84}	$C_{\mu_a\Theta_b}$	$C_{\Theta_b\Theta_a}$	$C_{\alpha_b\mu_a^2}$	$C_{\nu_b\mu_a^2}$
$H_2 - C_2H_4$	62.4	7.9	1428	725	74				
$H_2 - C_3H_4$	89.5	21	2515	2587	449.5				
$H_2 - C_4H_2$	104.5	34.5	3234	4834	1106				
$N_2 - C_2H_4$	153.5	19.6	4031	1824	160		-1.37		
$N_2 - C_3H_4$	220	51.6	6900	6413	1043		-3.67		
$CO - C_2H_2$	143	22	3949	2010	263	0.102	-4.27	0.046	0.024
$CO - C_2H_4$	168.5	21.5	4824	2044	177	0.053	-2.24	0.056	0.024
$CO - C_3H_4$	241.5	56.6	8153	7155	1153	0.143	-6.01	0.082	0.066
$NO - C_2H_2$	126	19.7	3198	1738	231	0.143	-3.07	0.091	0.049
$NO - C_2H_4$	149	19	3919	1770	156	0.075	-1.63	0.11	0.048
$NO - C_3H_4$	213	50	6710	6227	1016	0.202	-4.32	0.16	0.132

tations of the diatomic molecule are equally probable, the electrostatic contributions completely cancel. In contrast, in the case of the induction energy, the averaging over the diatom orientation leaves rather small $1/r^6$ contributions that may simply be added to the isotropic C_{60} dispersion coefficients if desired. Given that the esimated uncertainty in the dispersion coefficients is greater than 10%, the induction terms are more or less insignificant.

Chapter 5

SCATTERING ANALYSIS

5.1 Summary of Scattering Features

The determination of intermolecular potentials from molecular scattering experiments requires the analysis of resolved diffraction and rainbow oscillations in the experimental differential scattering cross sections. The general procedure for the extraction of potential energy surface information is to: 1) assume a particular model potential with adjustable fitting parameters, 2) calculate the theoretical scattering cross section, and 3) compare the theoretical prediction to the experimentally observed scattering cross section. In most cases, refinement of the potential parameters leads to a suitable agreement between the theoretical and experimental results. In addition, if complementary experimental data is used to constrain some parameters in the analysis, usually an improved potential energy surface can be determined.

Previous studies of atomic and weakly anisotropic systems have shown that the presence of the diffraction and rainbow oscillations can be used to determine the potential energy surface with good certainty. In particular, high frequency diffraction oscillations primarily provide information on the scale of the potential, while rainbow oscillations mostly provide information on the strength of the interaction. The angular spacing of the diffraction maxima are sensitive to the radial position of the potential minimum, and the angular position of the rainbow peak is related to the potential well depth.

The origin of the quantum interference features can be described in significant detail using the semiclassical approach, where wavelike particles are considered to

follow classical scattering trajectories. Classically, collisions originating from several different impact parameters may be deflected to the same scattering angle for systems with attractive-repulsive potentials. If we associate a wavelength with each classical deflection, interference effects must be considered. Since the particles travel different path lengths, the relative phase differences between the scattered waves lead to constructive and deconstructive oscillations in the scattering amplitudes.

The classical scattering theory presented in Chapter 3 showed a typical example of a deflection function for an attractive-repulsive potential, where three impact parameters, b_1, b_2, and b_3, lead to scattering at the same angle. In reference to Figure 3.2, small impact parameters (b_1) probe the repulsive short range interaction, while large impact parameters (b_2 and b_3) probe the attractive long range part of the potential.

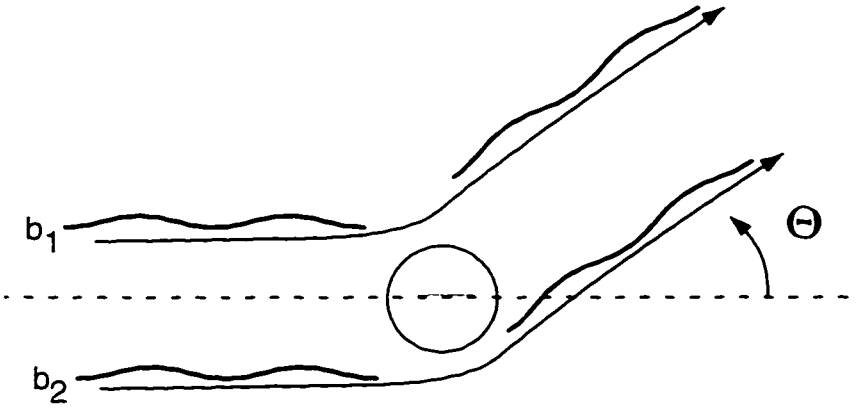

Figure 5.1: Interferences between scattered particle waves resulting from repulsive b_1 and attractive b_2 collision gives rise to diffraction oscillations.

Interference between waves scattered from the repulsive and attractive parts of the potential give rise to fast diffractive structure in the differential cross section. As shown in Figure 5.1, particles with trajectories b_1 and b_2 (or b_3) travel comparably different paths leading to relative phase differences between the scattered waves that either constructively or deconstructively interfere depending on the scattering angle.

If one considers an average impact parameter, $b_0 = (b_1 + b_2)/2$, assuming that the attractive and repulsive contributions tend to cancel for this trajectory, the angular spacing of the diffraction maxima be related to the scale of the potential, or more intuitively, the position of the radial minimum, $b_0 \approx r_m$.

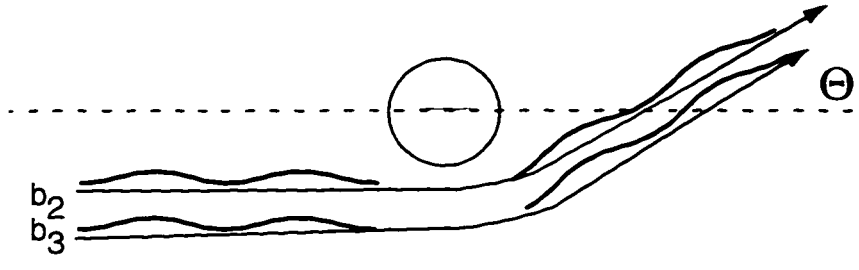

Figure 5.2: Interferences between scattered particle waves resulting from attractive collisions b_2 and b_3 give rise to rainbow oscillations.

Interference between the waves scattered from the attractive part of the potential give rise to slow rainbow structure in the differential cross section. As shown in Figure 5.2, the similar paths traveled by the closely spaced trajectories b_2 and b_3 result primarily in constructive interference at the scattering angle. As the impact parameters become closer together, much larger angular deflections are needed to cause a 2π change of phase between the scattered waves, therefore usually only a single rainbow oscillation is observed in thermal scattering experiments.

For diffraction oscillations, the center of mass angular spacing of the diffraction maxima, $\Delta\theta$, is related to the potential radial minimum, r_m, by:

$$\Delta\theta \approx \frac{\pi}{kb_0} = \frac{\pi}{kr_m} \tag{5.1}$$

where k is the associated wave vector at the relative collision energy, $E = 1/2\mu g^2$. The form of Equation 5.1 is analogous to Fraunhofer diffraction from optics. However, rather than the diffraction of a light wave by an aperture, in molecular scattering we observe the diffraction of a matter wave caused by the interaction potential. The

reduced wave vector, k, is strongly dependent on the reduced mass of the system. In general, the diffraction oscillations for small reduced mass systems, such as those involving He and H_2, have much greater angular spacing compared to large reduced mass systems for the same relative collision energy. The extremely fast diffraction oscillations for rather large reduced mass systems can be difficult to resolve with typical experimental angular resolutions ($\approx 1°$).

For the rainbow oscillations, the position of the rainbow maximum, θ_R, is approximately related to the spherical potential well depth, ϵ, by:

$$\theta_R \approx \frac{2\epsilon}{E} \tag{5.2}$$

where E is the relative collision energy, and the factor of 2 results from the assumption of a LJ 12-6 interaction potential. For most van der Waals systems at thermal energies, the ratio $E/\epsilon \simeq 5 - 10$, allowing resolved rainbow oscillations to be observed only for large (heavy) reduced mass systems, such as those involving Ar. For very weak interactions the rainbow peak lies inside the forward scattering, an angular range which is not measured in most differential scattering experiments.

Equations 5.1 and 5.2 are most applicable to spherical interactions, but they can provide qualitative guidance in the analysis of anisotropic systems. The rainbow and diffraction oscillations in total differential scattering measurements of molecular systems are significantly damped by the potential energy surface anisotropy. Previous experimental and theoretical studies of linear and non spherical molecules have shown that the damping of the scattering features in total differential scattering experiments can be used to extract information on the anisotropy of the potential energy surface to a high degree of accuracy.

In an initial study using IOS calculations to investigate He and Ar-CO_2 interaction potentials, Pack observed theoretically that the damping of the diffraction oscillations are mostly attributed to the anisotropy in the radial position minimum, while the damping of the rainbow oscillations is primarily related to the anisotropy

in the well depth [96]. Over the years. Keil and co-workers have measured the total differential scattering of He from several diatomic (N_2. O_2. CO. and NO) [65] and polyatomic molecules (CH_4. NH_3. H_2O. SF_6. CO_2. N_2O. and C_2N_2)[65. 99]. For the diatomic and spherical top molecules systems only central potentials were obtained from the analysis of the scattering data. However. for the long linear molecule systems involving CO_2. N_2O. and C_2N_2. the pronounced damping allowed the estimation of potential radial and angular anisotropies. Danielson et. al. has investigated He scattering from several hydrocarbons C_2H_2.C_2H_4. C_2H_6. CHF_3 obtaining anisotropic potentials [40. 41]. Using similar methods. Este et al. have developed anisotropic potential models for H atom - CH_4.C_2H_2. C_2H_6.C_3H_8. from total differential scattering experiments [42]. Others have studied H_2 scattering from several of the same diatomic and spherical top molecules already mentioned [67].

Pack obtained anisotropic potentials for Ar and Kr - SF_6 from the damping of rainbow oscillations in the the total differential scattering cross sections [97]. Yang measured the total differential scattering of He. H_2. N_2. and Ar from C_2H_2 and observed both the damping of diffraction and rainbow oscillations [26. 126. 124]. For the heavier Ar and N_2 -C_2H_2 systems. Yang used structural information obtained from spectroscopy to constrain the radial potential minimum position during the fitting of rainbow oscillations. since no diffraction oscillations were resolved in the scattering cross sections. In the case of by Ar- C_2H_2. an improved potential energy surface was obtained which agreed with both spectroscopic and scattering data. in contrast to the existing model surfaces which were valid for only one particular set of data[127]. Later analysis by Yang and co-workers of the Ar- C_2H_2 interaction using *ab initio*. spectroscopic. and scattering data have refined the potential surface still further. These studies demonstrate. importantly. that using existing experimental information in the fitting of total differential scattering data helps ensure confidence in obtaining a unique potential energy surface.

Table 5.1 shows a summary of the scattering systems investigated in this thesis.

Listed are the reduced masses, associated wavevectors, and relative collision energies[1] for each atmospheric gas-hydrocarbon molecule interaction. Also, identified are the observed scattering features in the total differential scattering cross sections. Based on these observations, it is possible to classify the results based on the observed scattering features and the type of interactions involved. In general, the light reduced mass systems (He and H_2), with the smallest associated wavevectors (large deBroglie wavelengths) exhibit fast diffraction oscillations, while the the heavy reduced mass systems (N_2, CO, NO, and Ar), with the largest associated wavevectors (small deBroglie wavelengths) reveal only rainbow oscillations. For the "medium" reduced mass systems involving Ne, both scattering features are simultaneously observed in the differential scattering cross sections. The rare gas-unsaturated hydrocarbons systems involve interactions dominated only by dispersion forces, while the diatomic molecule systems also contain interactions dependent on electrostatic and inductive forces.

---

[1]Calculated using the most probable velocities obtained from the TOF analysis.

Table 5.1: Summary of Scattering Features

System	μ amu	k A^{-1}	Energy Kelvin	Energy cm^{-1}	Feature[a]	Reference
$H_2 - C_2H_4$	1.88	8.3	889	617	diff.	
$H_2 - C_3H_4$	1.92	8.4	896	623	diff.	
$H_2 - C_4H_2$	1.94	8.5	898	624	diff.	
$He - C_2H_4$	3.50	11.0	836	581	diff.	[41]
$He - C_3H_4$	3.64	11.3	848	589	diff.	
$He - C_4H_2$	3.70	11.4	847	588	diff.	
$Ne - C_2H_2$	11.37	21.3	958	666	diff./rain.	
$Ne - C_2H_4$	11.73	21.9	983	683	diff./rain.	[123, 102, 56, 32, 61]
$Ne - C_3H_4$	13.42	24.2	1045	726	diff./rain.	
$Ne - C_4H_2$	14.39	25.2	1060	737	rain.	
$N_2 - C_2H_4$	14.00	25.9	1155	802	rain.	
$N_2 - C_3H_4$	16.47	29.4	1262	877	rain.	
$CO - C_2H_2$	13.48	25.1	1124	781	rain.	[13, 76, 77]
$CO - C_2H_4$	14.00	25.9	1156	803	rain.	
$CO - C_3H_4$	16.47	29.4	1263	878	rain.	
$NO - C_2H_2$	13.93	25.8	1151	800	rain.	
$NO - C_2H_4$	14.48	26.7	1184	823	rain.	[33]
$NO - C_3H_4$	17.14	30.4	1301	904	rain.	
$Ar - C_2H_4$	16.47	26.7	1044	725	rain.	[15, 56, 123, 61, 102, 32]
$Ar - C_3H_4$	20.00	30.9	1150	799	rain.	
$Ar - C_4H_2$	22.22	33.0	1183	822	rain.	[16]
$He - Ar$	3.64	10.9	790	550	diff.	[10]

[a]diff. = diffraction oscillation, and rain. = rainbow oscillation

Also listed in Table 5.1 are references compiled from the literature, listing sources of relevant information that may be used in the analysis of the scattering data. In general, the references include: previous scattering measurements; various theoretical studies of potential energy surfaces; and, most importantly, IR and microwave spectroscopic information on the complementary dimer clusters. Most of the literature has focused on studies concerning the smaller hydrocarbon systems (C_2H_2, C_2H_4), while very little information exists on the interactions of rare gas atoms and diatomic molecules, N_2, CO, and NO, with C_3H_4 and C_4H_2. Previous total differential scattering studies have involved the scattering of light probe particles, He and H_2. In contrast, spectroscopic experiments have focused mainly on the interactions of polar molecules or strongly interacting atoms, the most notable being HF, NH_3, H_2O, and Ar, with several hydrocarbon molecules. As a result, complementary sets of experimental data from both scattering and spectroscopy exist only for a few number of systems. In particular, experimental information on nonpolar molecular interactions is much less abundant in comparison to the so called hydrogen bonding studies.

The systems listed in Table 5.1 represent a class of van der Waals systems involving the interaction between a rare gas atom, or an essentially nonpolar diatomic molecule, and a larger, cylindrically shaped, unsaturated hydrocarbon molecule. Neglecting the small electrostatic and inductive energy contributions, these interactions are assumed to be dominated by dispersion forces. Further, the sequential $C-C$ rigid bonding frameworks and the π electronic structures of each of the hydrocarbon molecules is expected to contribute significantly to the size and shape anisotropies in these systems.

To aid the analysis of such a large number of scattering systems, it is useful to separate the results into three classes: 1) light interactions (He and H_2), 2) heavy interactions (Ne and Ar), and 3) diatomic interactions (N_2, CO, and NO). By application of Equations 5.1 and 5.2 many general trends and indications of the molecular anisotropy can be identified in the scattering data.

5.1.1 *Light Interactions*

Figures 5.3 and 5.4 show the differential scattering of He and H_2, respectively from each of the unsaturated hydrocarbon molecules, where each cross section has been scaled by an arbitrary factor for clarity. The He results show 3-4 resolved diffraction oscillations with an approximate spacing of 3° for each of the C_2H_4, C_3H_4, and C_4H_2 molecules. The damping of the cross sections is most significant at large scattering angles. The length of the hydrocarbon has a significant effect on the diffraction structure. The smaller ethylene is the least damped system, while the longer C_3H_4 and C_4H_2 much more damped, indicating a larger relative anisotropy in these systems. The interaction strength for most He interactions is approximately 30-40 K., so no obvious rainbow structure appears in angular range the scattering measurements.

Figure 5.4 shows the H_2 scattering from each of the hydrocarbon molecules. Similar trends in the damping of the diffraction oscillations is observed at large scattering angles and as the length of the hydrocarbon increases. An interesting damping pattern is obvious in the H_2-C_3H_4 system, where the second oscillation is almost completely damped, and for the H_2-C_4H_2 system, the diffraction structure is almost completely quenched at all angles. In comparison to the He results, the H_2 results show a greater number of oscillations (5-6) and a larger angular spacing ($4 - 5°$) between diffraction maxima. These changes are consistent with the expected changes in the interaction strength and reduced mass of H_2 systems. The interaction strength for most H_2 systems is approximately 100 K, and the reduced mass of the system has decreased essentially two-fold. No apparent rainbow structure can be identified in the H_2 scattering results.

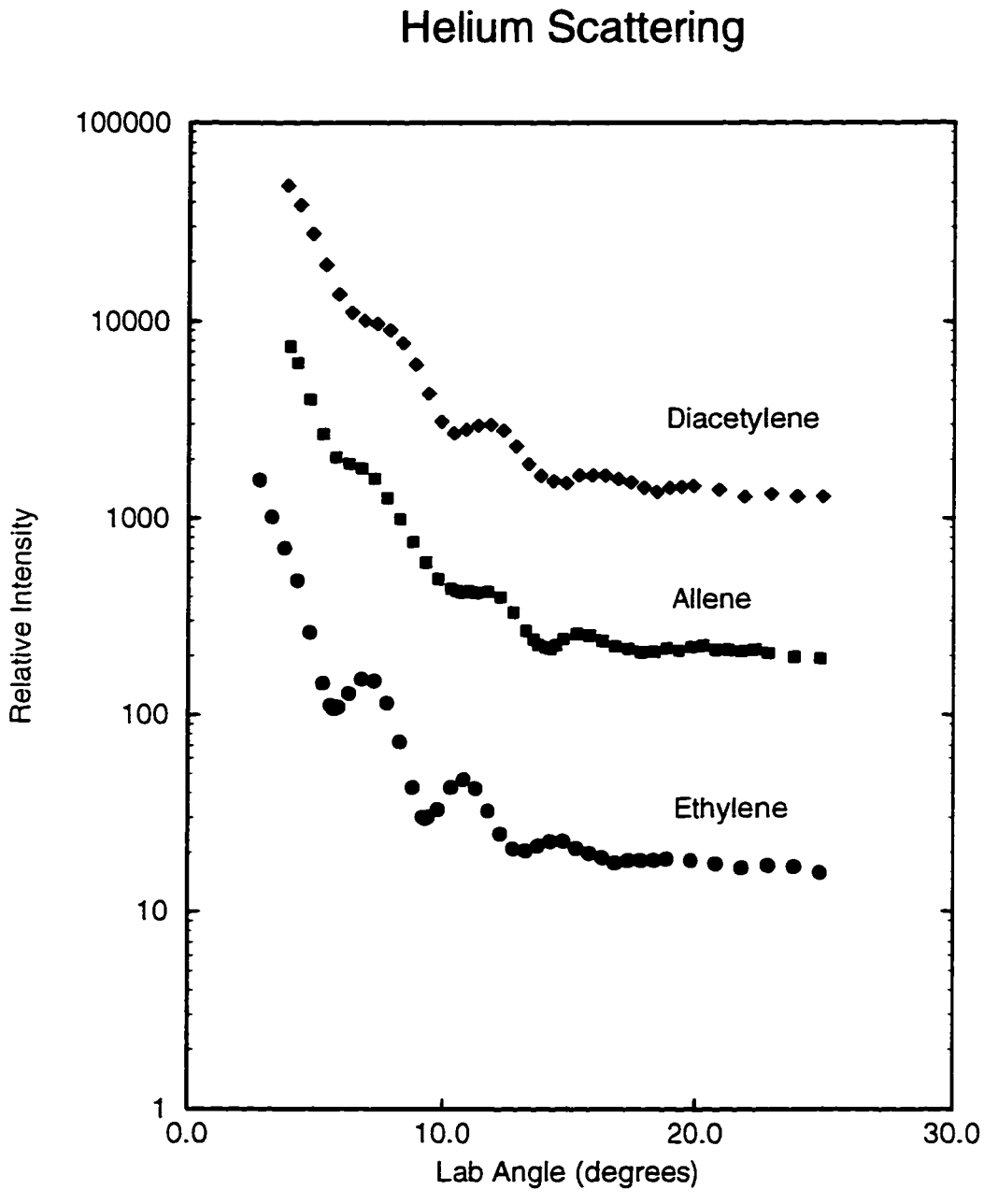

Figure 5.3: Helium scattering from C_2H_4, C_3H_4, and C_4H_2.

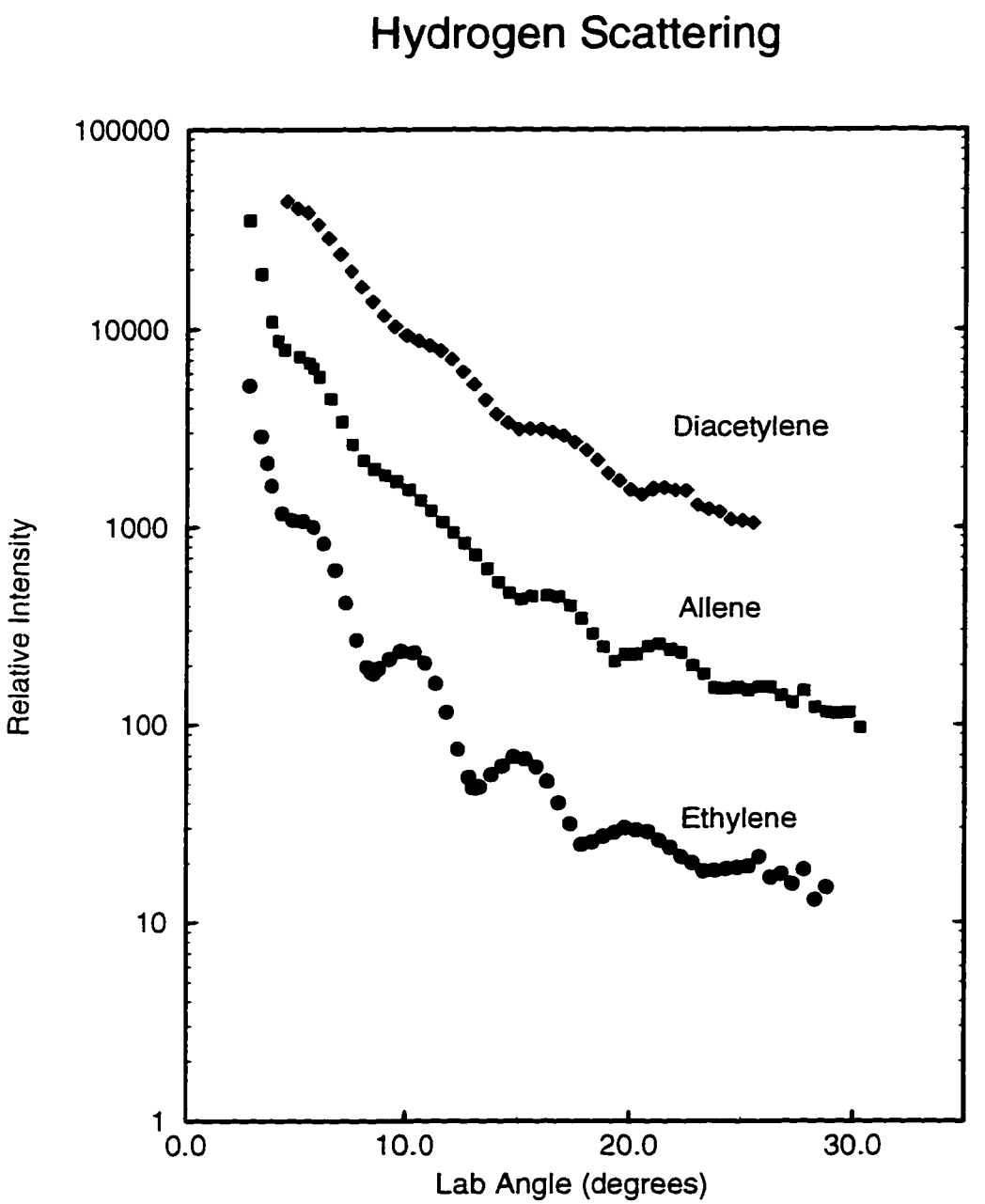

Figure 5.4: Dihydrogen scattering from C_2H_4, C_3H_4, and C_4H_2.

5.1.2 *Heavy Interactions*

Figures 5.5, 5.6, and 5.7 show the differential scattering of Ne and Ar atoms from each of the hydrocarbon molecules. These heavier reduced mass systems primary show rainbow oscillations, since the closely spaced diffraction oscillations are difficult to resolve given the angular resolutions of the experiments. Figure 5.5 shows the resolved rainbows for the Ne scattering systems, where scattering intensities have been weighted by an angular dependent factor $(\sin(\theta)\theta^{4/3})$ to more clearly show the scattering features. An obvious trend emerges: as the size of the hydrocarbon increases, the rainbow peak position moves to larger angles and the rainbow amplitude increases. Both effects indicate an increasing interaction strength for the more polarizable hydrocarbon molecules.

Close examination of the Ne-C_2H_2 result shows the presence of fast diffractive structure at smaller scattering angles. To examine this structure, the angular resolution of the experiment was improved by placing the bolometer in position A, and the scattering cross sections for the Ne-C_2H_2, C_2H_4, and C_3H_4 systems were remeasured as shown in Figure 5.6. The high resolution Ne scattering exhibits both scattering features, but covers a much smaller angular range due to a lower signal-to-noise ratio. As observed at low resolution, the rainbow oscillations shift to larger scattering angles as the hydrocarbon size increases. At high resolution the fast diffraction structure $(\Delta\theta \sim 1.5^\circ)$ is resolved but highly damped in all systems, barely noticeable in the Ne-C_3H_4 cross section. The presence of both damped diffraction and rainbow oscillations, provides complete information for determining the anisotropy in these systems.

Figure 5.7 shows the Ar-C_2H_4, C_3H_4, C_4H_2 scattering results. No apparent diffraction oscillations were resolved in the total differential scattering cross sections at either detector position. Compared to the Ne scattering the rainbow structure is more significantly damped and rainbow peak appears at much greater angles, both features increasing with the size of the hydrocarbon. In the case the Ar-C_4H_2 systems, the

damping almost completely precludes an obvious assignment of the rainbow peak, but the scattering at larger angles implies an interaction strength that is much greater than any of the systems already discussed. The very large damping in the Ar scattering cross sections indicate qualitatively, a large anisotropies in the well depths for these systems. However, contributions to the damping caused by inelastic scattering effects cannot be completely ruled out.

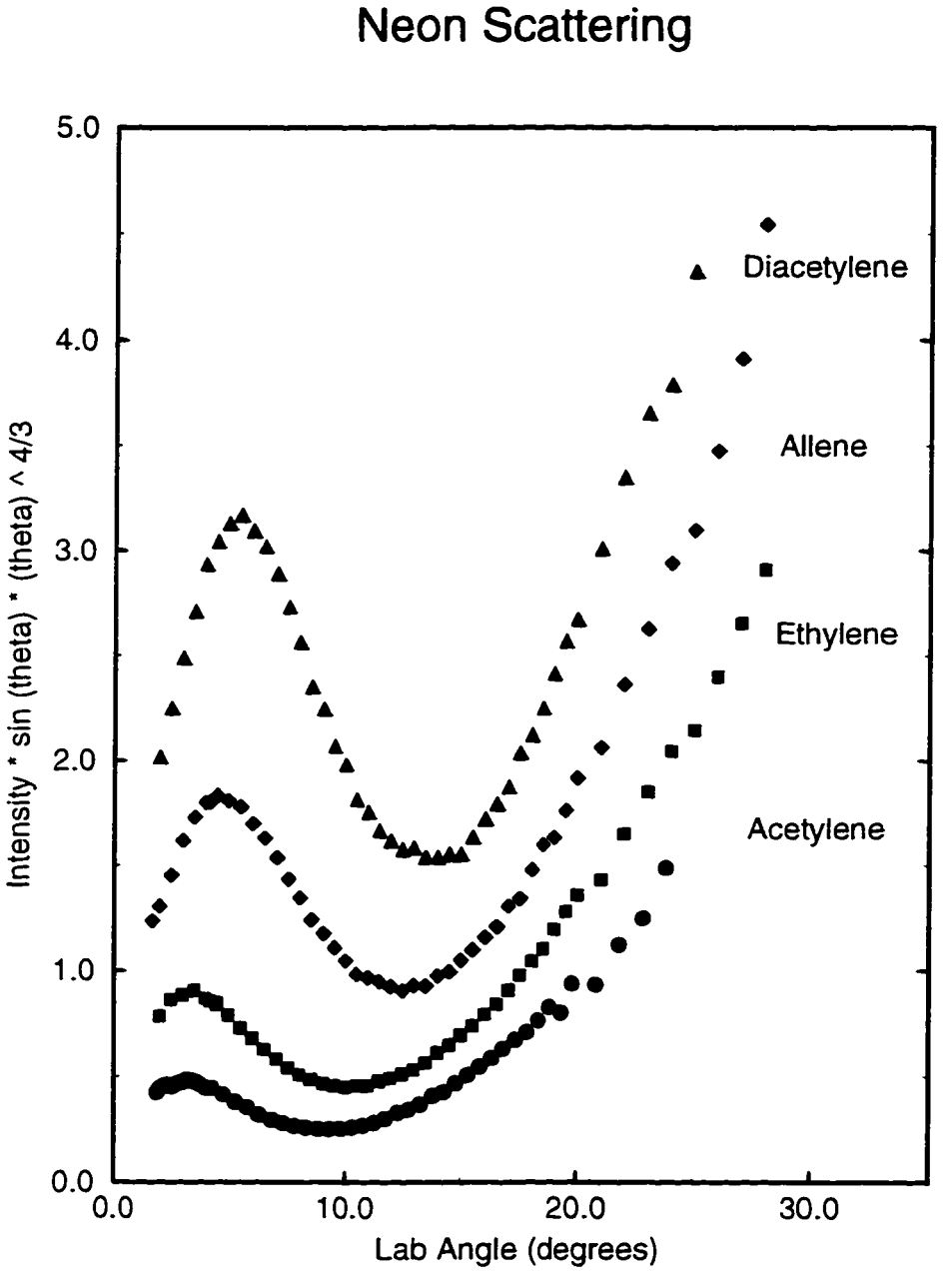

Figure 5.5: Ne scattering from C_2H_2, C_2H_4, C_3H_4, C_4H_2 with detector in near, low resolution position.

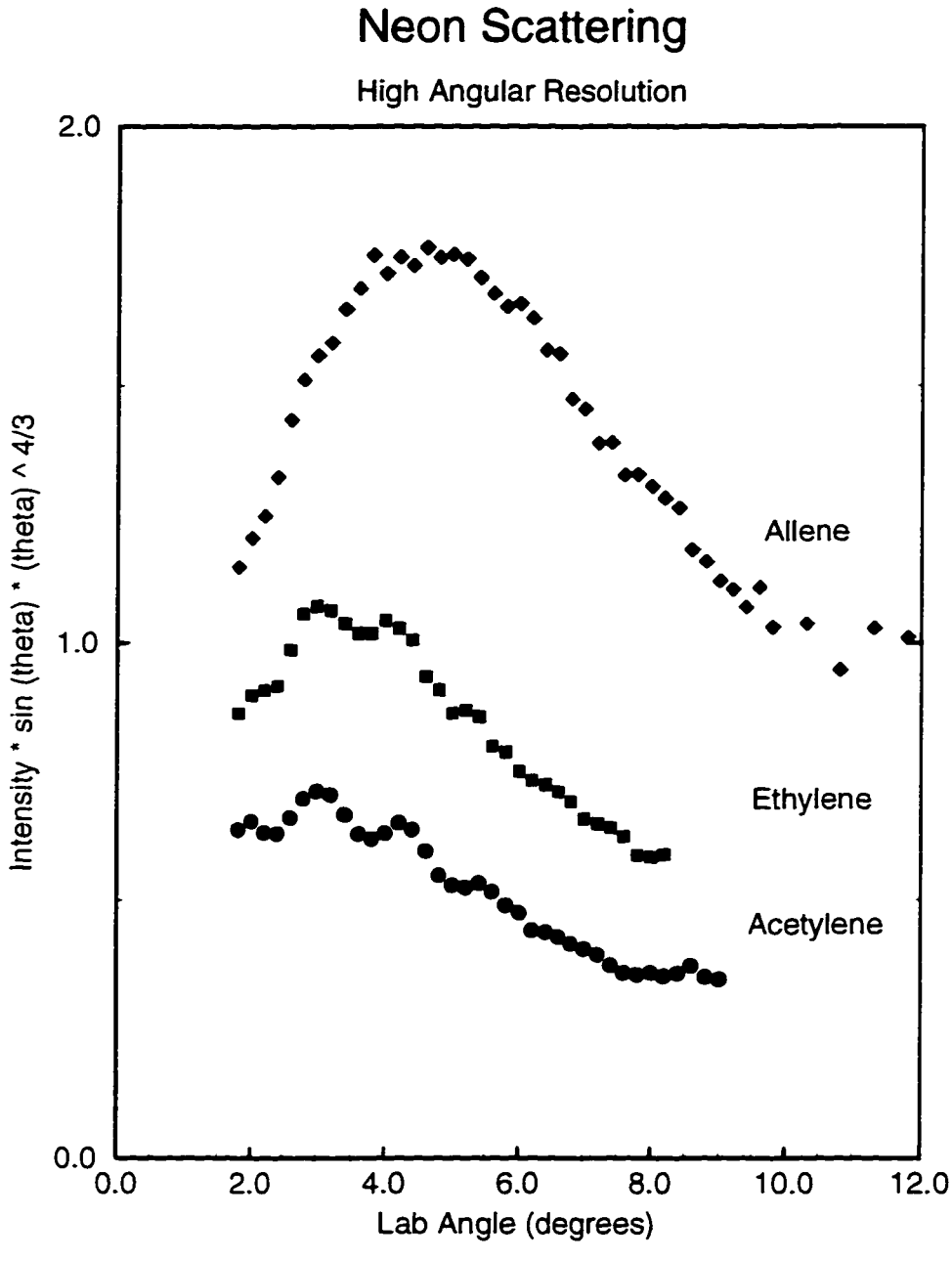

Figure 5.6: Ne scattering from C_2H_2, C_2H_4, and C_3H_4 with detector in far, high resolution position.

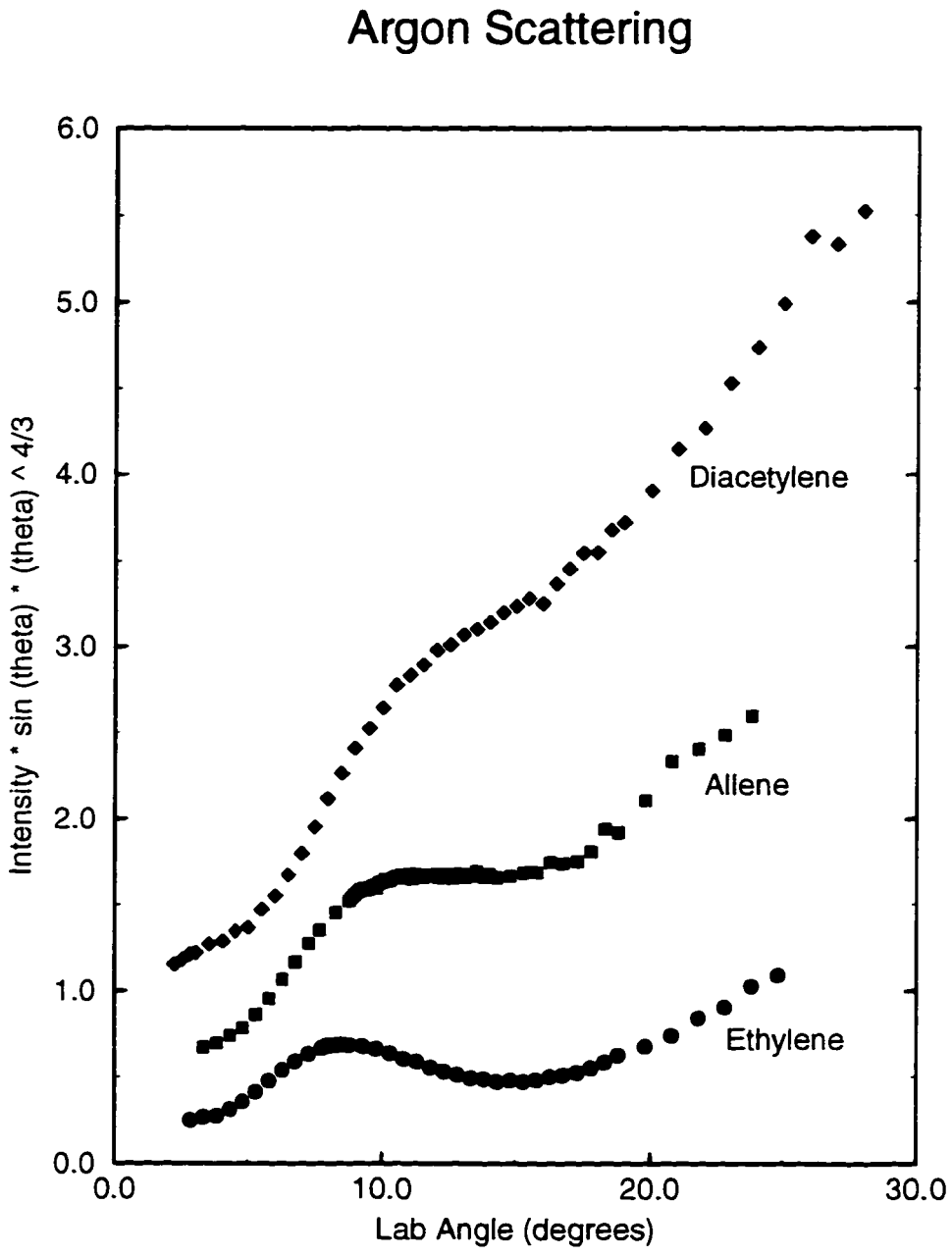

Figure 5.7: Argon scattering from C_2H_4, C_3H_4, and C_4H_2.

5.1.3 ***Diatomic Interactions***

Figures 5.8, 5.9, and 5.10 show the total differential scattering cross sections for N_2, CO, and NO, respectively. In general, all the diatomic interactions with the various hydrocarbons exhibit only broadened rainbow oscillations. For each probe case, as the polarizability of the hydrocarbon target increases, the rainbow maximum shifts to larger angles, again indicating a more attractive, interaction for the the more polarizable hydrocarbon molecules. If we compare the positions of the rainbows for a fixed target interaction the same trend is true. For example, the lab angle peak positions appear at 8.3°, 9.3°, and 8.5° for N_2, CO, and NO with ethylene, respectively.

Further, if we compare the shapes of the rainbows for the C_2H_2, C_2H_4, and C_3H_4 results for each diatomic probe case, we see a consistent trend for the acetylene scattering cross sections to be more damped than the ethylene and allene cross sections at large scattering angles, and the allene cross sections are considerably more damped than those for ethylene. In many of the systems, the actual rainbow peak is difficult to assign. However, the broadened shapes of rainbows are strongly indicative of the anisotropy in these systems.

From high resolution IR spectroscopy, CO and N_2 are known to form linear complexes with acetylene [13, 76, 77], while information on the NO-C_2H_4 dimer from predissociation spectra [33], indicates that NO-C_2H_4 interaction is T-shaped. Considering the scattering results in context to the existing spectroscopic information, perhaps preliminary conclusions may be drawn as to the structural properties of the diatom-hydrocarbon complexes. Based on the pattern of the total differential scattering data alone, the diatom-acetylene systems appear to be linear, while the diatom-ethylene and allene systems are most likely T-shaped. Nevertheless, a full IOS analyis of the scattering data needs be carried out to test the validity of this hypothesis.

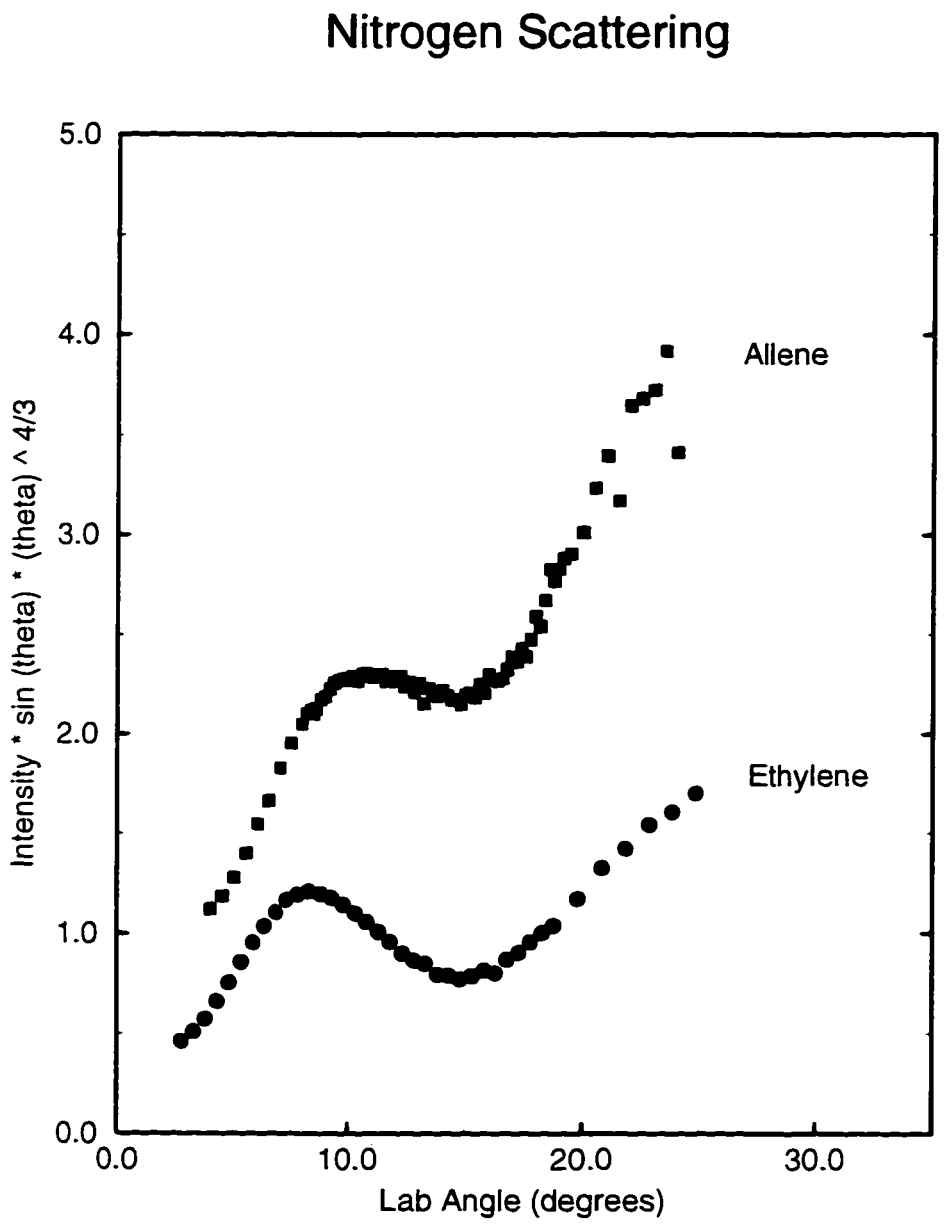

Figure 5.8: Nitrogen scattering from $C_2H_4$and C_3H_4.

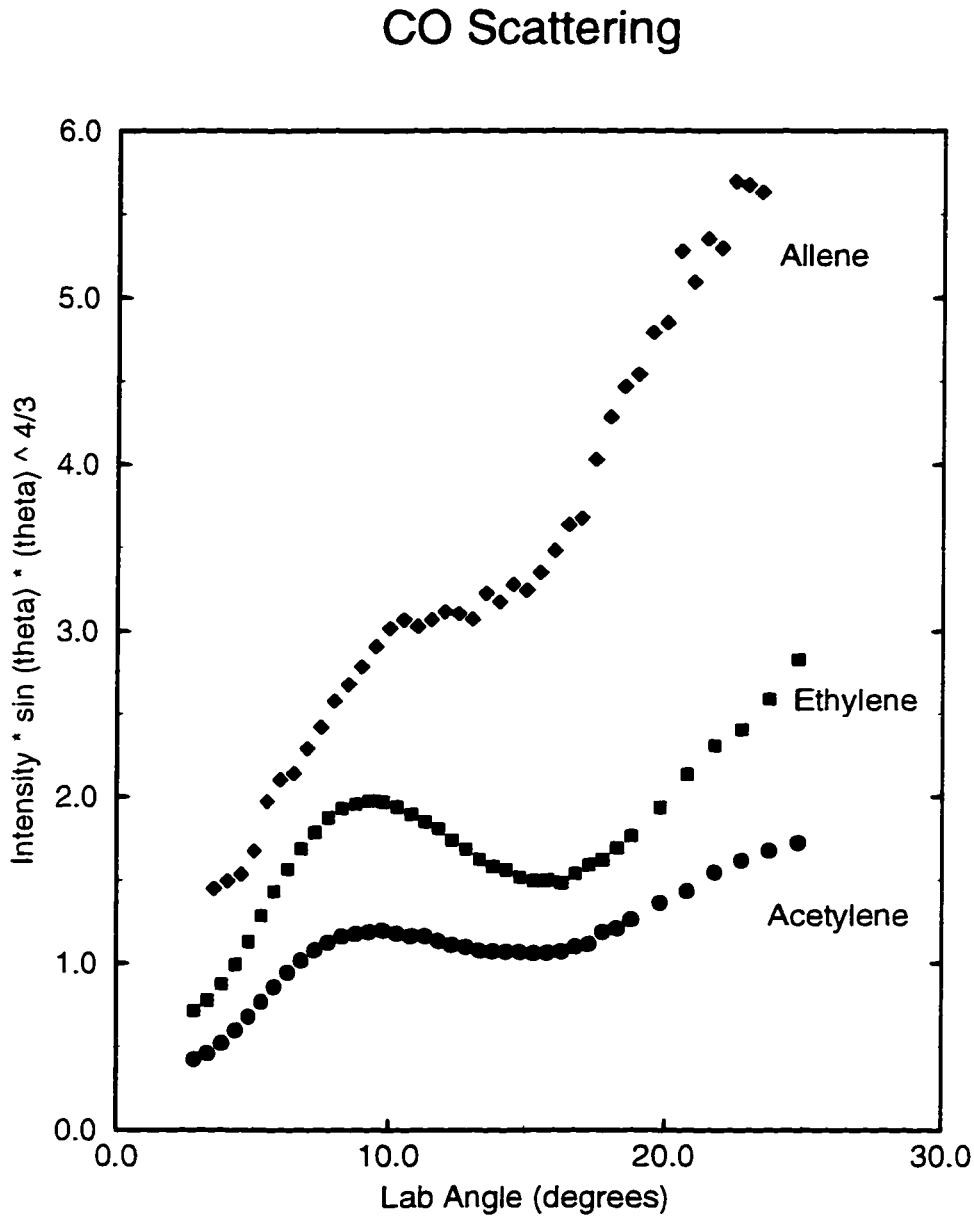

Figure 5.9: Carbon monoxide scattering from C_2H_2, C_2H_4, and C_3H_4.

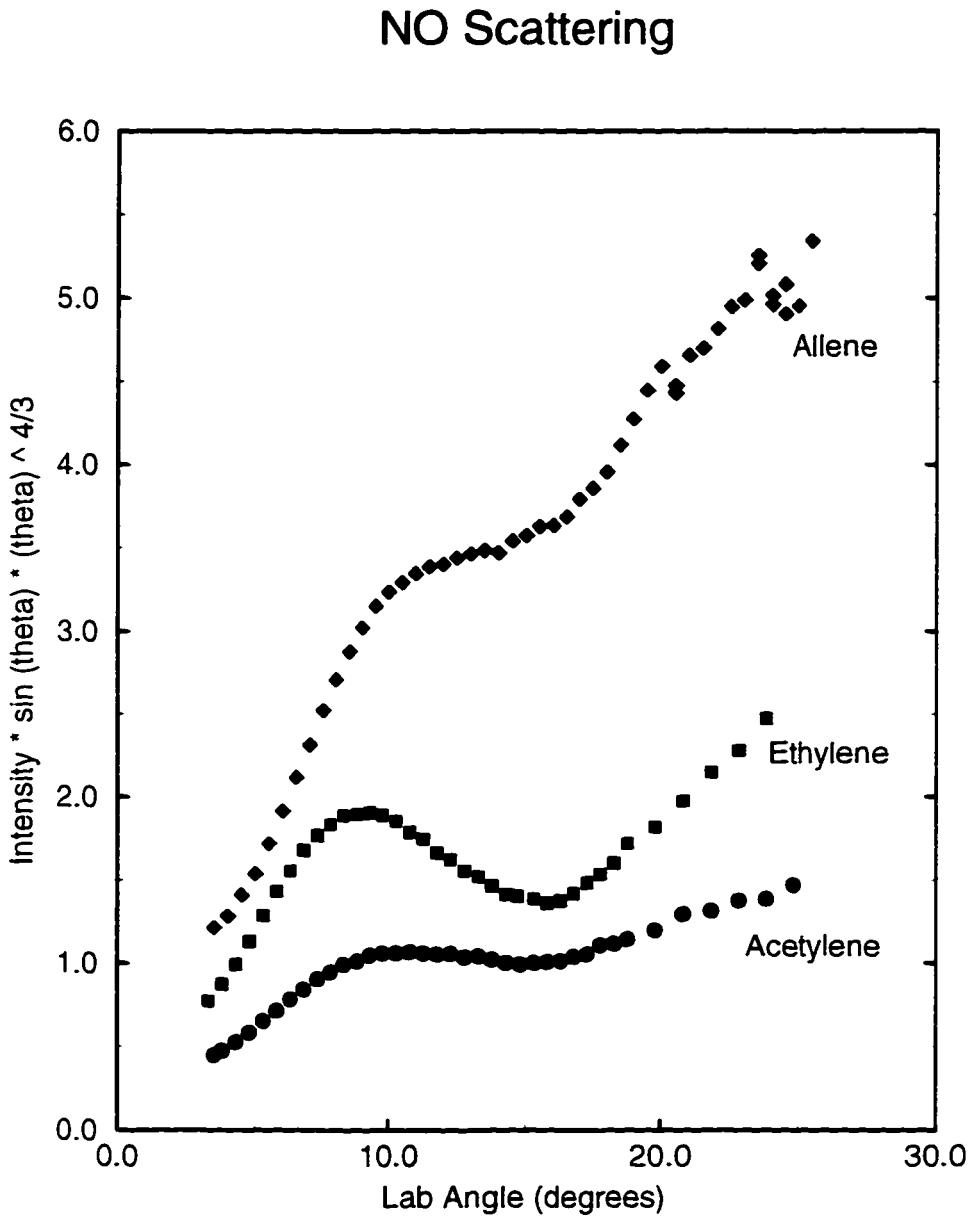

Figure 5.10: Nitric oxide scattering from C_2H_2, C_2H_4, and C_3H_4.

5.2 *Experimental Averaging*

While the damping of the scattering features is mostly due to the anisotropy of the potential energy surfaces, additional damping also arises from the experimental energy and angular resolutions. To a certain degree, the effect of the experimental averaging has been reduced by the use of supersonic molecular beams, collimating apertures, and a small detector size. Despite this, the full extent of the experimental damping must be accounted for, in order to more accurately extract the potential surface anisotropy from the differential scattering cross sections.

The determination of the anisotropic potential energy surface results from a "best-fit" comparison of an experimentally averaged, theoretical differential cross section to the experimentally observed results. In general, the theoretical cross section must be transformed from the center-of-mass (CM) frame to the laboratory (LAB) frame and averaged over the velocity distributions, the scattering volume, and the detector size before comparison to the experimental results can be made.

In an idealized experiment, the number of particles scattered per unit time to a detector situated at θ_{lab} and o_{lab} and subtending the solid angle $d\Omega_d$, is given by:

$$dI(\theta_{lab}, o_{lab}) = n_1\, n_2\, g\, I^{\circ}(\theta_{lab}, o_{lab})\, d\Omega_d\, dV_s \tag{5.3}$$

where n_1 and n_2 are the primary and secondary beam number densities, g is the relative velocity defined by the initial source velocities, v_1 and v_2, and dV_s corresponds to the infinitesimal scattering volume defined by the crossed beams. The important quantity, $I^{\circ}(\theta_{lab})$, is the differential cross section in the LAB frame, which is related to the theoretical differential scattering cross section in the CM frame by:

$$I^{\circ}(\theta_{lab}, o_{lab}) = J(d\omega, d\Omega)\, I(\theta_{cm}, o_{cm}) \tag{5.4}$$

with $J(d\Omega, d\omega)$ being the jacobian transforming the CM to t LAB frame solid angles, $d\omega$ and $d\Omega$, respectively.

5.2.1 *CM to LAB Transformation*

The transformation of the theoretical cross section from the center-of-mass reference frame to the laboratory reference frame is most easily understood in terms of the Newton diagram. Figure 5.11 shows a typical Newton diagram for the in-plane ($\theta_{lab} = 180°$) scattering of a light particle (m_1) from a heavy particle (m_2). v_1 and v_2 are initial velocity vectors intersecting at the LAB scattering center with an angle ζ, defining the relative velocity, $\mathbf{g} = |\mathbf{v_1} - \mathbf{v_2}|$. The initial CM velocity vectors u_1 and u_2 intersect at the CM origin, which is displaced from the LAB origin by the center-of-mass velocity, v_m. The LAB scattering angle is defined by the angle between the initial and final LAB velocity vectors, v_1 and v_1'. Likewise, the CM scattering angle is defined by the angle between the initial and final CM velocity vectors, u_1 and u_1'.

In the scattering process, the total relative collision energy must be conserved. For an elastic scattering event, this implies that the initial and final velocity vectors in the CM frame are equal, $u_1 = u_1'$ and $u_2 = u_2'$. Figure 5.11 depicts the conservation of energy for particle 1 by a solid circle of radius u_1 centered at the CM origin, and similarly, the conservation of energy for particle 2 by a dashed circle of radius u_2 at the same CM origin. It is important to notice that as the position of the detector sweeps through angles $0 - \theta_{lab}$ in the LAB frame, there is one corresponding CM angle for the scattering of particle 1. Particle 2, however, is not scattered into the range of LAB angles shown. Further, the final LAB velocity of particle 1 increases throughout the range of LAB angles, as indicated by the position where v_1' cuts the Newton sphere. For scattering systems where the lighter particle, $m_1 < m_2$, is detected, the LAB and CM scattering angles are similar, $\theta_{lab} \approx \theta_m$, and an unambiguous scattering transformation exists between the CM and LAB angles. This is the case for the scattering of light particles such as He and H_2.

In the detection of the heavier particle, the CM to LAB transformation is more complicated. Figure 5.12 shows a typical Newton diagram for the in-plane scattering

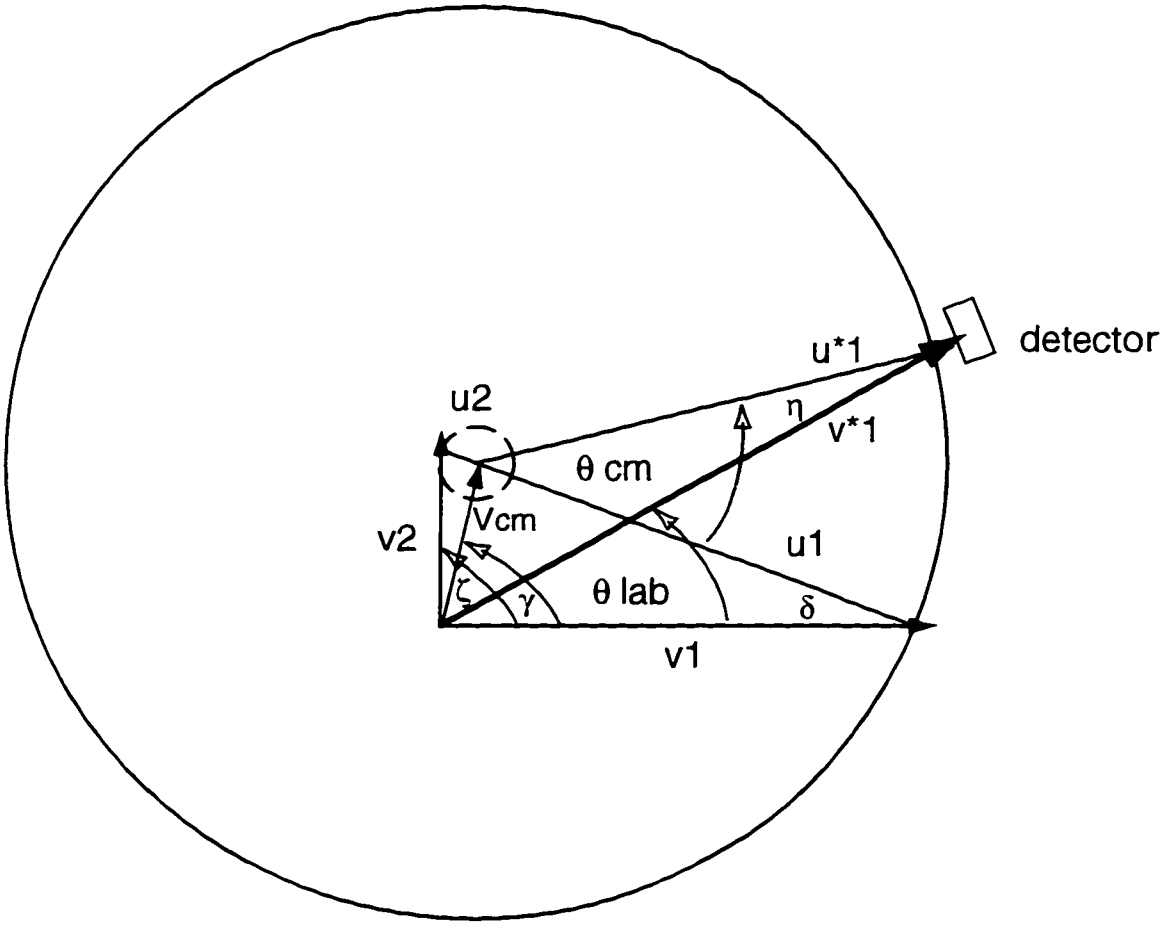

Figure 5.11: Newton Diagram for Elastic Scattering - Light Particle Detection

of a heavier particle (m_1) from a lighter particle (m_2). The depicted symbols correspond to the same velocities and angles as mentioned in the previous figure. However in this case, several important differences appear. No longer is there an unambiguous scattering event, since more than one CM angle contributes to the scattering at a given LAB angle. Notice there are two scattering contributions for the particle 1 and only one from particle 2. This complicates the analysis since the bolometer is only sensitive to the total flux hitting the surface and not the particle's identity. Therefore, a separate CM differential scattering cross sections must be calculated for each contribution that reaches the detector. Although, the backward scattering of particle 1 with much slower velocities can be neglected, since the bolometer is less sensitive to slower moving particles.

In Figure 5.12, it is also important to note that the corresponding range of CM angles is much greater than the range of LAB angles covered by the detector. Therefore, the compression of the many CM angles into LAB frame contributes to the damping observed in the experimental cross sections. For scattering systems where the heavier particle, $m_2 < m_1$, is detected the LAB angles are approximately half as large as the CM angles, $\theta_{lab} \leq 2\theta_{cm}$. This case applies mostly for the Ar-hydrocarbons systems. The compression of CM angles into the LAB frame and the numerous scattering contributions makes the direct interpretation of the LAB frame scattering features difficult. Any conclusions about the potential parameters drawn from the spherical model analyses are qualitative at best.

Thus far only elastic scattering contributions have been discussed in the analysis of the scattering data. For inelastic scattering events, the internal energy of the molecules may change during the collision process. The conservation of energy implies that the CM velocity must change accordingly with the internal state excitation or de-excitation of the molecule. The final CM velocity for an inelastic scattering event

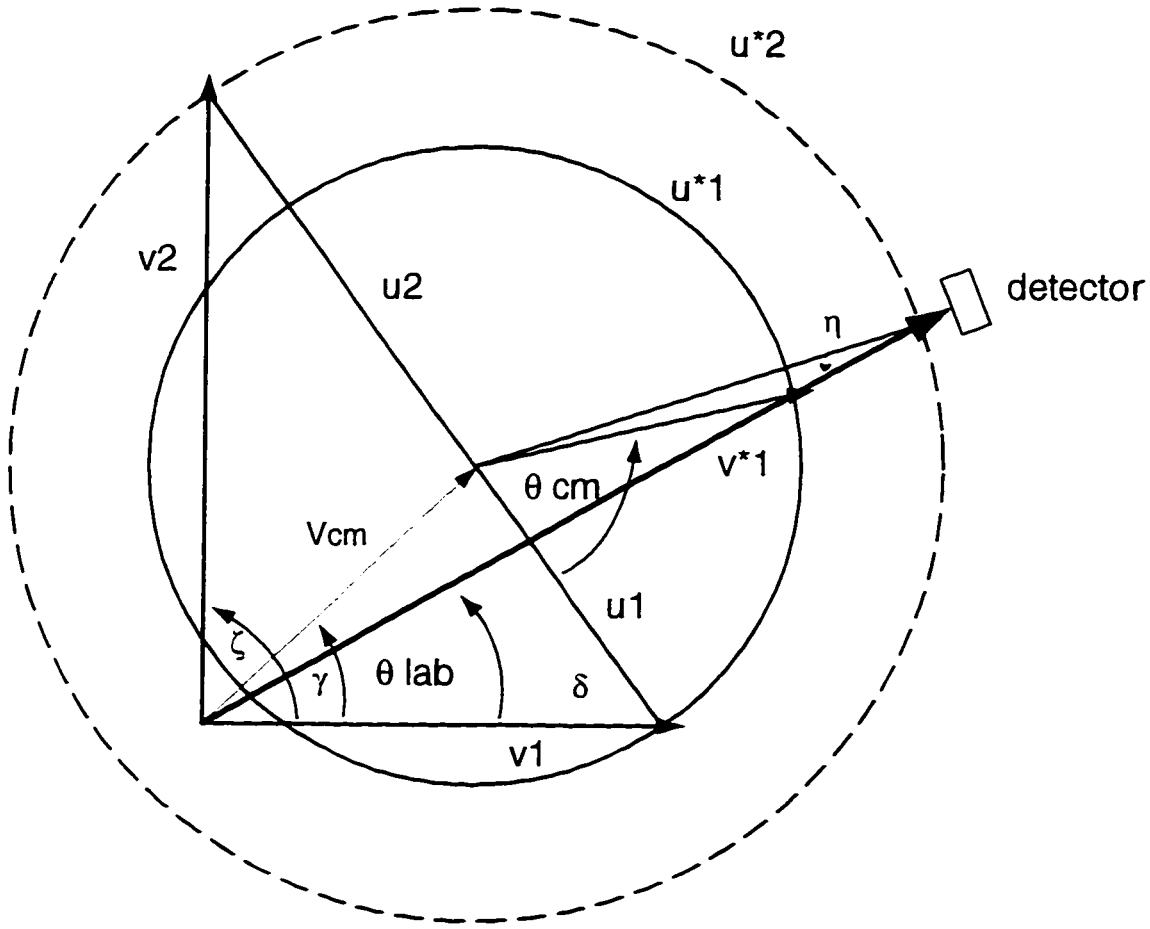

Figure 5.12: Newton Diagram for Elastic Scattering-Heavy Particle Detection

is given by:

$$\frac{u_i^*}{u_i} = \lambda = \left(1 - \frac{\Delta E}{E}\right)^{\frac{1}{2}} \tag{5.5}$$

where $E = 1/2\mu g^2$ and $\Delta E = E_{j'k'} - E_{jk}$. λ is the known as the CM velocity stretching ratio, allowing the inelastic Newton spheres to be calculated from the fractional energy transfer. For rotational excitation of the target molecule $\lambda < 1$, while for de-excitation $\lambda > 1$. Obviously, the elastic scattering condition is when $\lambda = 1$.

Figure 5.13 shows a Newton diagram for the inelastic scattering of the Ar-C_4H_2 system, considering only rotational excitation of the diacetylene molecule. The solid circles indicate the elastic scattering of both particle 1 (Ar) and particle 2 (C_4H_2), while the dashed circles represent the final rotational states $j' = 10$, 20, and 50 for the diacetylene molecule. The most obvious feature is that for a given LAB angle, there are several scattering contributions from both elastic and inelastic scattering events which reach the detector, each having a different CM transformation. Due to the small rotational constant of C_4H_2 there are many accessible rotational channels which need to be accounted for. However, the separation of the elastic and inelastic scattering contributions requires a very sophisticated analysis, which is beyond the scope of this thesis. In a first approximation, under the assumption that the damping effects are dominated by elastic collisions at small angles, only an IOS analysis of the total scattering cross sections were carried out. A reasonable approach, given the unavailability of potential energy surface information for the many of the molecular systems.

In addition, the inelastic Newton diagram indicates the origin of the large Δj inelasticities that were theoretically predicted by Yang [127]. In Figure 5.13, the detector position eclipses the side of the $j' = 50$ Newton sphere, where θ_{cm} angle approaches zero for a finite LAB scattering angle. Consequently, this kinematic effect implies that sharp inelastic scattering features may be observed at small LAB scattering angles. The classical interpretation is that these features result from large

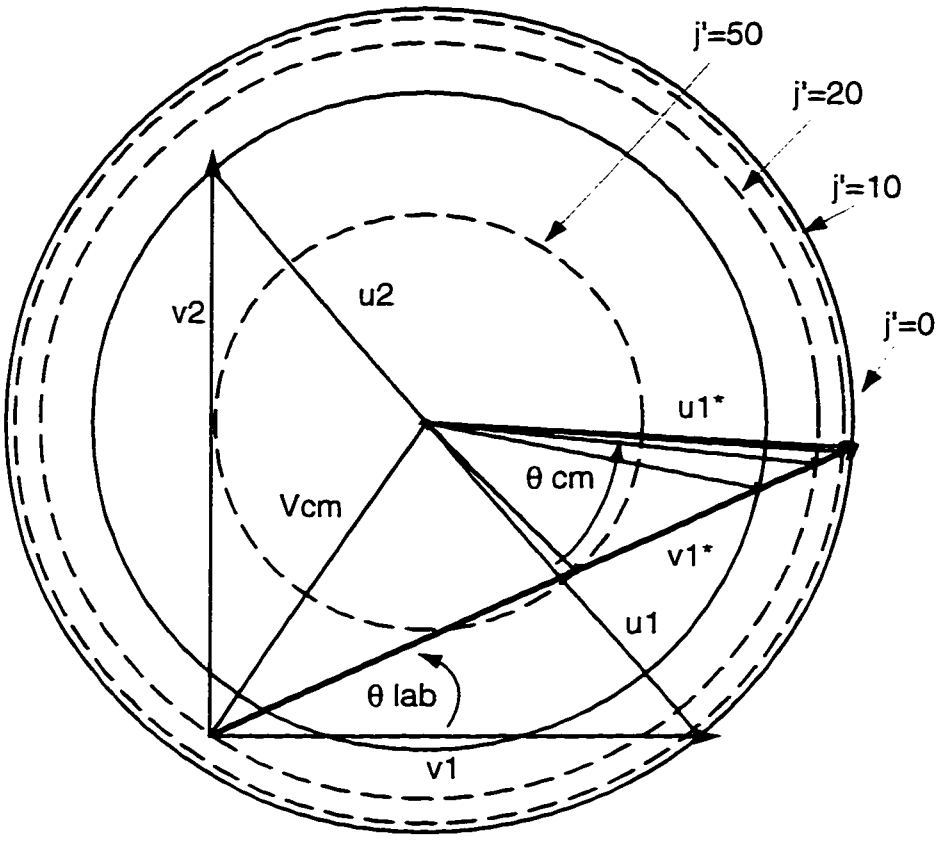

Figure 5.13: Newton Diagram for Inelastic Scattering Ar from Diacetylene.

impact parameter "tipping" collisions which cause large rotational state transitions but are only minimally deflected to small angles. Unfortunately, no such sharp inelastic scattering features were observed in any of the measured scattering cross sections. As yet, no experimental evidence exists to suggest that such novel rotationally inelastic features are indeed real. Additional state-selective experiments or time of flight methods would have be used in order to distinguish between the elastic and inelastic contributions in the total differential cross sections. Resolved rotational state information would be invaluable for determine the anisotropic potentials for these larger molecular systems, especially in the repulsive region.

The elastic and inelastic Newton diagrams indicate the complexity of the scattering dynamics and the basis of the CM to LAB transformation. From any of the Newton diagrams, the ratio solid angles in the two reference frames can be determined. The jacobian for the transformation from the CM to LAB frame is given by:

$$J(d\omega, d\Omega) = \left(\frac{u_1^*}{v_1^*}\right)^2 \frac{1}{|\cos\eta|} \tag{5.6}$$

where η is defined by the angle between the final velocity vectors u_1^* and v_1^*.

In the analysis, rather than calculate the full differential cross section over the full CM angular range, we only determine the differential scattering cross section for the CM angles which correspond to the experimentally observed LAB angles. Extensive derivations of the CM to LAB transformation procedures for the differential scattering cross section measurements have been presented in the literature [57], as well as by previous workers in our laboratory [22, 21]. A review of the important relationships presented in those source is given here for clarity.

In general, all the transformation properties can be expressed in terms of the initially known quantities such as: the particle masses (m_1 and m_2), particle velocities (v_1, v_2, g, u_1, u_2, and v_{cm}), and angular variables (θ_{lab}, γ, δ, and ζ). The final laboratory velocity of either particle is determined in terms of the LAB frame stretching velocity ratio, $\Lambda = v_i^*/v_i$ using the equation:

$$\Lambda = \left(\frac{v_{cm}}{v_i}\right) D \pm \left[\left(\frac{v_{cm}}{v_i}\right)^2 \left(D^2 - 1\right) + \lambda^2 \left(\frac{u_i}{v_i}\right)^2\right]^{\frac{1}{2}} \tag{5.7}$$

where

$$D = \cos(\gamma - \theta_{lab}) \ . \tag{5.8}$$

The jacobian transforming CM solid angle to the corresponding LAB solid angle in Equation 5.6 is expressed in terms of the initial laboratory and center-of-mass variables by :

$$J(d\omega, d\Omega) = \frac{\Lambda^3}{\lambda} \frac{v_i^2}{u_i^2} |\cos\delta + \lambda[(u_i/v_i)(C + \Lambda B) + A]|^{-1} \tag{5.9}$$

where the subscript indicates the jacobian for the detection of either particle 1 or 2.

The CM angles corresponding to each LAB angle for in-plane scattering ($\sigma_{lab} = 180$) are determined using:

$$\tan\theta_m = \Lambda \frac{v_i}{u_i} \frac{(B - A^2)^{\frac{1}{2}}}{[1 + \Lambda (u_i/v_i) A]} \tag{5.10}$$

where

$$A = \cos(\theta_{lab} + \delta) - \cos\delta/\Lambda \tag{5.11}$$

$$B = \sin^2\theta_{lab} + C^2 \tag{5.12}$$

$$C = \cos\theta_{lab} - 1/\Lambda\ . \tag{5.13}$$

Once the theoretical differential scattering cross section has been calculated in the CM frame, it is transformed to the LAB frame via the jacobian, and has to be averaged over the velocity distributions, scattering volume, and detector size before comparison to the experimental results. In addition, all contributions to the total scattering signal must be considered. The integration of Equation 5.3 over all the experimental variables, considering all scattering contributions, is given by:

$$I_{AVE}(\theta_{lab}) = \sum_i \int d\Omega_d \int dV_s \int dv_1 \int dv_2\ f(v_1)\ f(v_2)\ \frac{g}{v_1}\ I^{\circ}(\theta_{lab})\ D(v^*) \tag{5.14}$$

where the $1/v_1$ has been added to account for non-stationary target molecules, and $D(v^*)$ is the velocity dependent bolometer detection sensitivity.

The bolometer detection efficiency is proportional to the total energy released by the incident scattered flux. The predominate contributions to the detection efficiency result from the absorption energy, E_a, due to the condensation of particles on the bolometer surface and translational kinetic energy $1/2\ m_i v_i^{*2}$ energy. The detector response function is expressed as:.

$$D(v^*) \propto E_a + \frac{1}{2} m_i v_i^{*2}. \tag{5.15}$$

For the non-condensible particles, primarily He, the translational kinetic energy is the dominate contribution to the detector response, while for more condensible species such as Ar, N_2, CO, and NO, the surface adsorption energy may dominate. Previous workers have investigated the bolometer detection response function [22, 121, 124] for various systems. In general, only the translation kinetic energy dependence has been considered for most analyses, since the surface adsorption energies of most incident species are not accurately known. The effect of neglecting the surface adsorption energy release of the condensible particles may result in a over estimation of the scattering contributions at angles greater than the rainbow angle, which is most sensitive the repulsive part of the potential energy surface. Previous investigations which considered all cases for the detection efficiency have concluded that the position of the rainbow peak is largely unaffected by the choice of the detection response. Based on these previous findings, only the final translational kinetic energy of the particles has been considered in the analysis of the scattering data presented here. In order to keep the proper units of the calculated scattering cross section, the detection efficiency is weighted by the average kinetic energy as:

$$D(v^*) = \left(\frac{v_f^*}{v_i^*}\right)^2 . \tag{5.16}$$

The detector response for each LAB angle is then calculated using the initial velocity information and the stretching ratio, Λ given earlier.

The actual averaging procedure for Equation 5.14 is carried out in two procedures by separating the velocity dependent variables from the apparatus geometrical variables. The theoretical differential scattering cross section is first energy averaged over the velocity distributions of the two beams before the angular averaging over the detector size and scattering volume is carried out. The full extent of the averaging procedures concerning the molecular beam apparatus has been described in detail elsewhere [22, 21]. However, since this procedure plays a large role in the success of determining anisotropic potentials from the total differential scattering cross sections.

a brief outline of the experimental averaging is worth reviewing here.

5.2.2 *Energy Averaging*

Rather than perform the velocity averaging over the individual velocity distributions, it is more convenient to conduct the velocity averaging in the corresponding CM variables. Since the scattering dynamics depend only upon the relative collision energy, the velocity integration variables v_1 and v_2 may be transformed to the variables g, ζ, and δ where the velocity averaging is transformed by:

$$\int dv_1 \int dv_2 \rightarrow \int d\zeta \int dg \int d\delta \tag{5.17}$$

and the CM variables in terms of the LAB velocities can be obtained from the Newton diagram as:

$$v_1 = \frac{g \sin(\zeta + \delta)}{\sin \zeta} \quad \text{and} \quad v_2 = \frac{g \sin \delta}{\sin \zeta} . \tag{5.18}$$

and the jacobian of the transformation is given by:

$$J_v(v_1, v_2, \delta \mid g, \zeta, \delta) = \frac{g}{\sin \zeta} . \tag{5.19}$$

As mentioned earlier in the Experimental Methods, the supersonic velocity distributions of the primary and secondary beams have the form:

$$f(v)dv = Nv^3 \exp\left[\frac{-(v - v_s)^2}{v_\alpha^2}\right] dv . \tag{5.20}$$

Since the relative velocity is a function the angle between the LAB velocities ζ, the energy averaging must performed over the non-orthogonal collisions due to the angular divergence of the secondary beam. The average over ζ is carried out assuming the secondary beam angular divergence follows a Gaussian distribution as:

$$s(\zeta) = \exp\left[-\ln 2 \left(\frac{\pi/2 - \zeta}{\Delta/2}\right)^2\right] \tag{5.21}$$

where Δ is the full width at the half maximum.

Using the transformation properties and CM velocity variables, the velocity averaged differential scattering cross section may be expressed as:

$$\bar{I}_v(\theta_{lab}) = \frac{1}{N_v} \int d\zeta \int dg \int d\delta \; f(g,\delta,\zeta) \; J_v(v_1, v_2, \delta \mid g, \zeta, \delta) \; s(\zeta) \; I^\circ(\theta_{lab}) \qquad (5.22)$$

where $1/N_v$ expresses the proper normalization integral for the energy averaging procedure, and $f(g,\delta,\zeta)$ includes the transformed velocity distributions and bolometer detection efficiency.

The integration of Equation 5.22 is performed using Gauss-Chebyshev numerical quadratures in g, δ, and ζ. The integration limits for g and δ are determined by the 10% velocity cutoff points obtained using the stream velocities and velocity widths of the primary and secondary beams, while ζ integration limits are determined by the secondary beam angular divergence. The covergence of the integrations are tested by increasing the number of quadrature points for each variable. Usually 7-9 points in each variable give an adequate smoothing, which will be discussed later for the He-Ar test results.

5.2.3 Angular Averaging

After the energy averaging, the differential scattering cross section must be averaged over the geometrical variables defining the detector size and the finite scattering volume. The angular averaging of the energy averaged cross section is given by :

$$I_{AVE}(\theta_{lab}) = \int d\Omega_d \int dV_s \; \bar{I}_v(\theta_{lab}) \qquad (5.23)$$

The solid angle may be expressed in terms of the detector size variables α and h, where α represents the lateral position on the bolometer surface, and h is the bolometer surface height above and below the plane of the plane of the crossed beams. Figure 5.14 shows the relevant parameters for the angular averaging procedure. The solid angle expressed in terms of the two geometric variables is given by:

$$d\Omega_d = w(\zeta, h, \alpha) \; d\alpha \; dh \qquad (5.24)$$

where

$$w(\zeta, h, \alpha) = a^2 \cos\alpha \left(a^2 + h^2 \cos^2\alpha\right)^{-\frac{3}{2}} \tag{5.25}$$

and

$$a = R - z\cos\theta_{lab} \tag{5.26}$$

and

$$z = L_2 \tan(\pi/2 - \zeta) \tag{5.27}$$

Since the primary beam was initially assumed to have no width, the scattering volume integration becomes one dimensional ($dV_s \rightarrow dz$), where the distance z indicates the scattering zone position along the direction of the primary beam. The angular averaging is then determined by:

$$I_{AVE}(\theta_{lab}) = \frac{1}{N_a} \int dz \int d\alpha \int dh\ w(\zeta, h, \alpha)\ I_v(\theta_{lab} + \alpha) \tag{5.28}$$

where $1/N_a$ is the normalization factor, and the integration over the horizontal bolometer width is included by modifying the LAB angles by α.

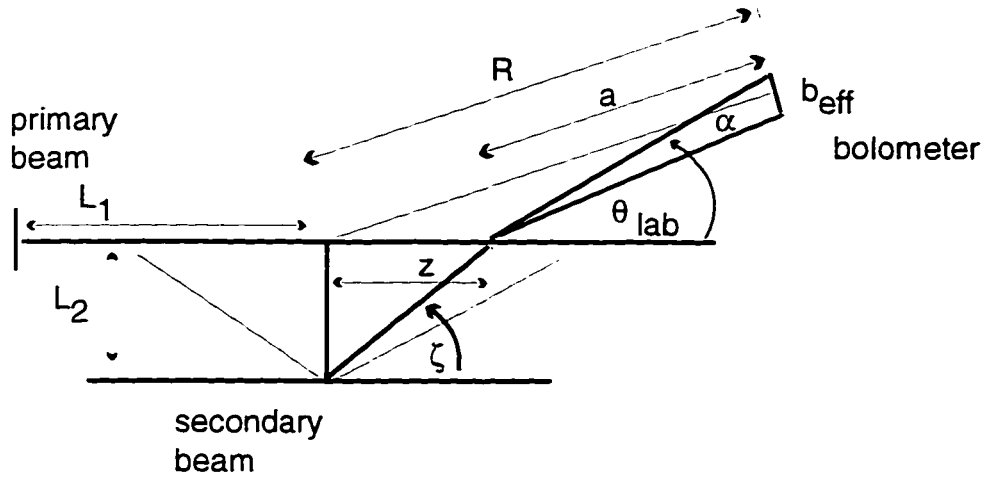

Figure 5.14: The geometric variables for angular averaging procedure over the scattering volume and detector size

The previous work conducted in our lab showed that the integral over the detector height may be performed analytically, since the out-of-plane averaging contributes little to the full averaging procedure[22]. Further, it was also found that the assumption of zero angular divergence for the primary beam did not allow for adequate smoothing of the cross sections at small angles [21]. In order to avoid further integrations over the scattering volume, the primary beam divergence was included into the integration over the detector size. The projection of the primary beam angular divergence at the scattering center was used to determine "effective" bolometer dimensions. Considering these modifications, the integration over the detector height is then given by:

$$\int dh\ w(\zeta, h, \alpha) = h_{eff} \cos\alpha \left(a^2 + h_{eff}^2 \cos^2(\alpha)/4\right)^{-\frac{1}{2}} \tag{5.29}$$

with

$$h_{eff} = h_0 + 2L_1 \tan(\Delta/2) \tag{5.30}$$

and where h_0 is the actual bolometer height, and the second term indicates the projection of the primary beam angular divergence onto the detector height.

Similarly, the detector width was modified to account the primary beam divergence. The "effective" bolometer width is given by:

$$b_{eff} = b_0 + 2L_1 \tan(\Delta/2)\cos\theta_{lab} \tag{5.31}$$

where b_0 is the actual bolometer width. The modification of the bolometer width, thus increases the range of the α integration in Equation 5.28.

The angular average integration is carried out using a 4-point Gauss-Legendre quadrature for both variables. Table 5.2 shows the various experimentally important distances which define angular divergences, the scattering volume, and the angular resolutions characteristic of the molecular beam apparatus.

Table 5.2: Experimentally important distances defining scattering volume, angular divergences, and angular resolution of total differential scattering experiments.

Property	Symbol	Primary Beam	Secondary Beam	Detector
nozzle-dia.	d_0	50 μm.	50 μm.	
1st. skim. dia.	d_1	400 μm.	800 μm.	
2nd. skim. dia.	d_2	1.0 mm.		
nozzle-skim. dist.	s	10 mm.	10 mm.	
skim.-scat. center dist.	L	100.0 mm.	20.2 mm.	
ang. diverg.-FWHM	Δ	1.0 deg.	5-6 deg.	
scat. center-detect. dist.	R			B - 152 mm.
				A - 652 mm.
bolometer dimensions	$b_0 \times b_0$			2 mm. $\times$ 6 mm.

5.2.4 *Statistical Fitting*

After the full energy and angular averaging procedure, the experimental and the theoretical IOS differential scattering cross sections are compared in terms of the minimized sum of the squared deviations between the two results. The statistical comparison of the experimental and theoretical differential cross sections is determined by the quantity:

$$S = \frac{1}{N} \sum_i \left[\frac{I_{AVG}(\theta_i) - \beta I_{EXP}(\theta_i)}{\beta I_{EXP}(\theta_i)} \right]^2 \tag{5.32}$$

where β is a scaling factor for the experimental data and N are the number of experimental data points.

In general, the "least-squares" quantity is evaluated for several potential parameter sets until a "best-fit" to experimental results has been obtained. In order to remove any bias in the final outcome of the potential energy surface parameters, a

re-iterative algorithm based on the Simplex minimization method [104] was used to adjust the parameters. The initial choice of potential parameters are based on either existing experimental data or previous theoretical calculations as mentioned. In general, several hundred iterations for various potential parameter sets are carried out before the converged values are obtained. The use of the Simplex minimization procedure is invaluable for determining accurate anisotropic potential energy surfaces from the severely damped differential scattering cross sections, since, in general, the large number of experimental averages dramatically affect the efficiency of the calculation. A robust automated minimization procedure greatly increases the certainty in regards to the uniqueness of the intermolecular potentials determined by purely empirical methods.

5.2.5 Helium - Argon Differential Scattering

The role of the experimental averaging may be assessed through the calibration of the apparatus parameters and the analysis methods by measurement of an atomic system which has no molecular anisotropy. The He-Ar differential cross section exhibits fast diffractive oscillations which are quenched to some degree depending on the energy and angular averaging. Using an accurately known potential for the He-Ar interaction from the literature [10], the sensitivity of the experimental averaging procedures on the damping of the observed scattering features can be determined within the accuracy of the experimental measurements.

Figure 5.15 shows the results of analysis for the He-Ar differential scattering cross section measured in both the high and low angular resolution configurations. Both measurements show very well-resolved diffraction oscillations of considerable amplitude compared to the molecular scattering systems. The results of the analysis using the Aziz potential are shown by the solid lines. In general, several angular and energy averages are necessary to fully account for the damping of the diffraction oscillation in the atomic system. Usually 7-9 quadrature points for each energy integration variable

are required to get the desired smoothing. The only difference between the fitting procedures for the high and low He-Ar differential cross sections, is the magnitude of the adjustable apparatus parameter which defines the effective bolometer size. In order to obtain the adequate smoothing in the high angular resolution case, the projection of the primary beam divergence was increased two-fold in comparison to the value used in the low resolution results. Nevertheless, excellent fitted results for both He-Ar cross sections were obtained over the complete angular range measured for the majority of the experiments. The accurate characterization of the experimental damping due to the averaging procedures greatly improves the confidence in the determined anisotropic potential energy surfaces for the atmospheric gas-hydrocarbon molecule systems presented in this thesis.

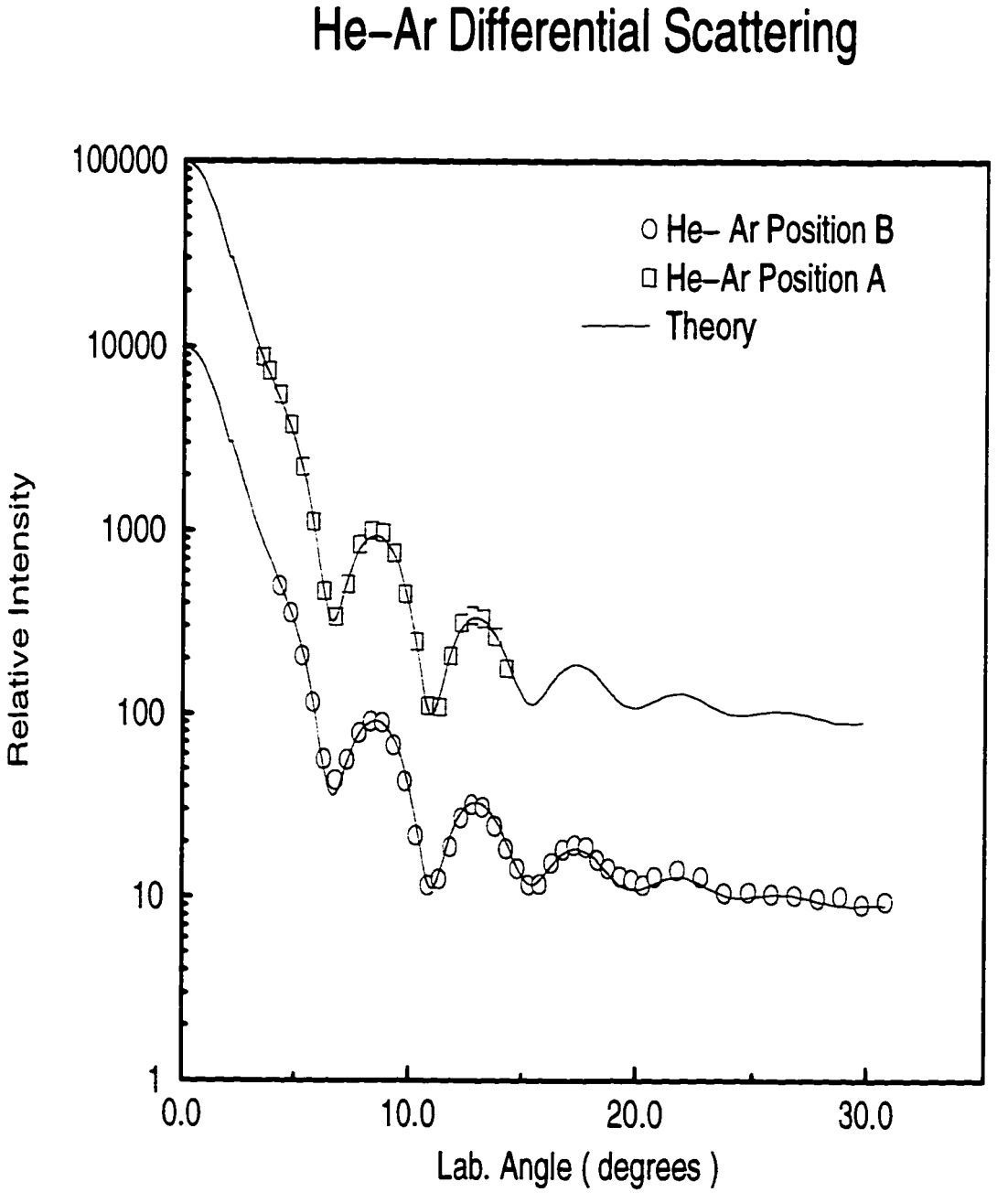

Figure 5.15: Differential scattering cross sections for He-Ar interaction with the detector in positions A and B. Data points are the experiments, and the solid lines are the single-channel calculations using Aziz potential [10] and the full experimental averaging procedures.

Chapter 6

RESULTS

The intermolecular potentials of twenty-one atmospheric gas-unsaturated hydrocarbon systems were determined empirically from a best fit to the corresponding total differential scattering cross sections. In general, the scattering data does not provide complete information sensitive to all ranges of the potential energy surface for all the systems studied in this thesis. As indicated previously, the light reduced mass systems in general exhibit fast diffraction oscillations which are most sensitive to the scale of potential, or the radial minimum position, r_m, while the heavy reduced mass systems show mostly a single rainbow oscillation which is most sensitive to the interaction strength of the potential, or the well depth, ϵ. The damping of the diffraction and rainbow oscillations provide information on the potential energy surface size and shape anisotropies respectively. For atom-cylindrical molecule systems, a convenient measure of the relative anisotropies is obtained by comparing the differences in the interactions for orientations parallel and perpendicular to the molecular symmetry axis. Thus $\Delta r_m = r_{m,\|} - r_{m,\perp}$ and $\Delta\epsilon = \epsilon_\| - \epsilon_\perp$ define the relative size and shape anisotropies, respectively.

Although some of the systems contain diatomic and / or nonlinear hydrocarbon molecules, all of the systems were treated as atom-linear molecule type interactions with the dominant attractive contributions arising solely from dispersion forces. This approximation may be more or less severe depending on the particular scattering system. However, given the number of experimental averages required to smooth the theoretical cross sections, as well as the additional computational effort required to include multiple degrees of freedom in the interactions, we feel this assumption and

approach to the analysis is valid. The results indicate that reasonable interaction potentials may be determined using the IOS analysis of total differential scattering cross sections for larger molecular systems. While not of the level of full spectroscopic accuracy, we hope these results will provide a basis for more advanced calculations such as cluster bound-states, van der Waals stretching and bending frequencies, and rotationally inelastic scattering transition probabilities. In any event, the determined potential energy surfaces for the atmospheric gas-unsaturated hydrocarbon molecules presented here are the first step in determining full multidimensional intermolecular potentials for larger van der Waals molecules and clusters.

The potential energy surface results are presented in three sections based on the types of interactions and the dominant scattering features. Section 6.1 presents the results for the light reduced mass systems involving the He and H_2 interactions. The results for the heavy reduced mass systems involving the Ne and Ar interactions are presented in the Section 6.2. The results of the diatomic interactions are presented in Section 6.3. As a general summary, the results of the IOS analysis indicate that the Lennard - Jones potentials are rather inflexible and lead to more anisotropic interactions compared to the Barker model interactions. More confidence is placed on the determined Barker model potential results, despite having an additional adjustable parameter, because of the better characterization of the anisotropic long range interaction forces. In each section, examples providing indications of the scattering feature damping due to the potential energy surface anisotropy are presented, as well as some discussion as to the sensitivity of the determined potential results due to actual potential form and parameterization.

6.1 Light Interactions – He *and* H_2

The total differential scattering cross sections of the helium and hydrogen scattering systems exhibit fast diffraction oscillations which are increasingly damped in ampli-

tude as the length of the hydrocarbon target increases. The damping of the diffraction oscillations should provide information about the potential size anisotropies in these scattering systems. While no discernible rainbow scattering was observed in the He and H_2 scattering cross sections, the amplitude and number of resolved diffraction oscillations is greater for the more strongly interacting hydrogen systems, indicating that some information on the attractive potential may be determined.

The intermolecular potentials of He and H_2 - hydrocarbon systems have been investigated previously using scattering experiments. As mentioned earlier in the Analysis section, Yang determined anisotropic potentials from total differential scattering measurements for He and H_2 with C_2H_2 [124, 126, 26]. The He-C_2H_2 system was similar to the results measured earlier by Danielson et. al. [40, 41]. In previous work, Danielson also determined the interaction potential for the He-C_2H_4 system [41]. Further, using similar methods Scoles and coworkers have investigated H atom scattering from several alkanes, such as methane, ethane, and propane [42], which might have similar size anisotropies to the unsaturated systems. To the best of out knowledge, the results presented here are the first type of potential energy surface information yet available for He and H_2- unsaturated hydrocarbon molecule interactions, with the exception of the He-C_2H_4 system.

6.1.1 Helium - Ethylene, Allene, and Diacetylene Results

Spherical model potentials were incapable of describing the total differential scattering cross sections over the full measured angular range. In general, anisotropic terms up to P_2 in the potential minimum and well depth were needed to give adequate fits to the experimental data, although the sensitivity of the fit is less sensitive to inclusion of the well depth anisotropy. An example of the quality of the fitted results using Barker model is shown in Figure 6.1. The best-fit lines indicate an excellent agreement to the experimental results even for the most damped systems.

Table 6.1 shows the determined potential parameters for a Lennard Jones N-6

potential and and two equivalent of Barker potential models. The most obvious feature presented in the table is the increase in the r_{m2} parameter as the length of the hydrocarbon increases. The He-C_2H_4 is shown to be the more spherical system compared to other results, and the relative differences in r_{m2} parameters correspond roughly to an increase by half a carbon-carbon bond length. The Lennard Jones results, in particular, fit the results less well as measured by the fitting statistic. Further, comparison of the different potential forms shows that the Lennard Jones potential seem to underestimate the well depths compared to the Set-A Barker model findings, although the shape anisotropies and the size parameters are quite similar in the two models.

Comparison of the two parameter sets for the Barker model shows significant differences in the well depth ϵ_2 and A_2 terms. In Set B the well depth is completely isotropic and the width of the potential well has increased considerably in comparison to Set A. The differences between the Barker model parameter sets for each hydrocarbon systems is more clearly illustrated in Figure 6.2, which depicts the repulsive and attractive regions of the Barker potentials in both the parallel (180 degrees) and perpendicular (90 degrees) orientations. The most significant comparison is the consistent agreement between both Barker potentials in the perpendicular orientations for all interactions. For the parallel orientations, the two sets agree much less in the repulsive region with Set A being softer for all interactions compared to Set B. For the parallel orientations in the attractive region, the two sets have large variability in the well depths and position of the radial potential minima.

The large variability in the potentials for the parallel orientations is however consistent with the IOS weighting due to the Gauss-Legendre quadrature, which gives larger weights to the perpendicular orientations compared to the parallel orientations. Therefore one might expect less sensitivity (a larger variability) in the results for the parallel interactions in all systems as well as a consistency in the results for the perpendicular orientations. Interestingly, the relative size anisotropies, Δr_m, seem to be

conserved between Sets A and B, especially for the He-C_4H_2 interaction (approximately 1.5Å) despite having much different r_{m0} and r_{m2} terms. Further refinement of the potential results could be obtained using SCF *ab initio* calculations to constrain the repulsive interactions for these lighter systems systems.

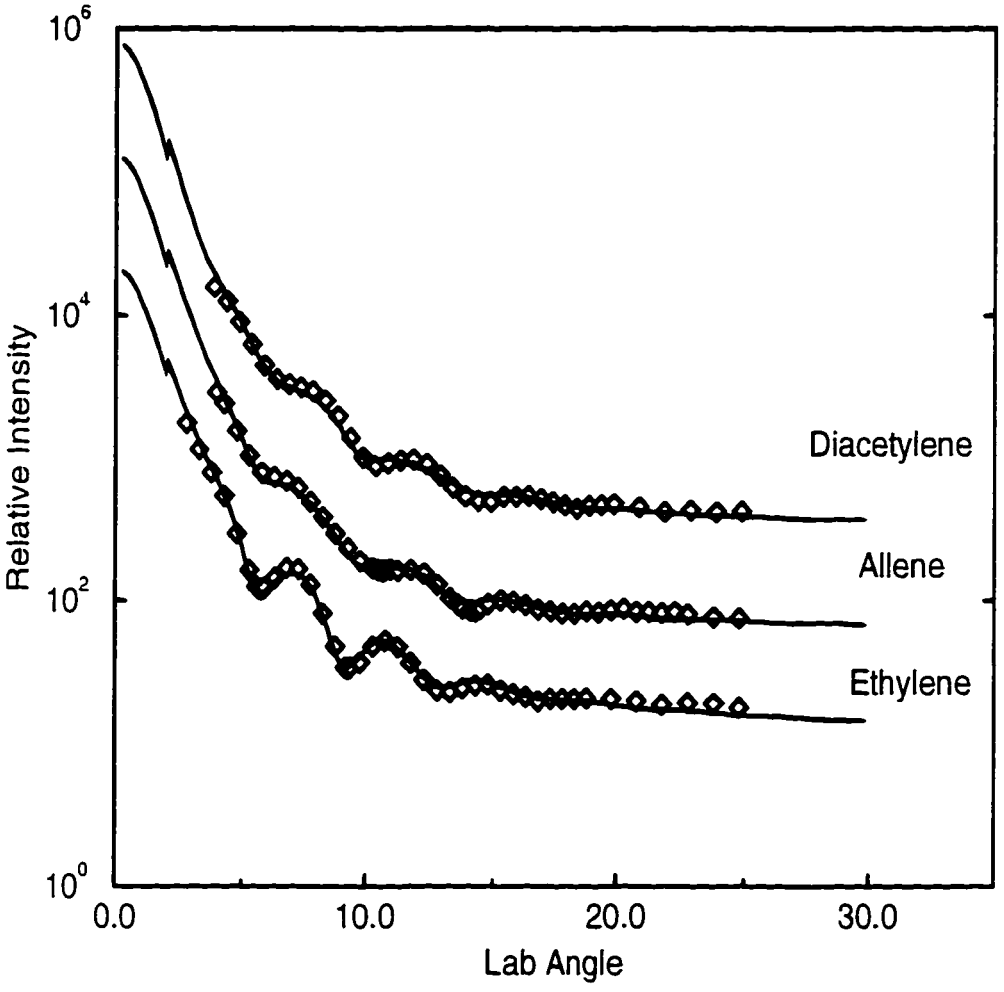

Figure 6.1: Barker Model Potential for He - C_2H_4, C_3H_4, and C_4H_2. Line is best-fit from IOS analysis.

Table 6.1: Summary of Lennard - Jones and Barker Potential Parameters for He with C_2H_4, C_3H_4, and C_4H_2.

Lennard-Jones Parameters		He C_2H_4	He C_3H_4	He C_4H_2	Barker Parameters		Set A He C_2H_4	Set A He C_3H_4	Set A He C_4H_2	Set B He C_2H_4	Set B He C_3H_4	Set B He C_4H_2
r_{m0}	$(\AA)$	3.98	3.95	4.27	r_{m0}	$(\AA)$	3.98	3.97	4.3	3.90	3.92	4.13
r_{m2}	$(\AA)$	0.61	1.07	1.90	r_{m2}	$(\AA)$	0.61	1.05	1.85	0.49	1.02	1.55
ϵ_0	(K)	29	34	36	ϵ_0	(K)	32	35	37	31	34	38
ϵ_2	(K)	-17	-10	-20	ϵ_2	(K)	-15	-15	-20			
N		12	24	25	α		11.5	12.5	13.3	11.9	13.3	14.2
					A_2		5	40	30	14	100	80
S_{fit}	$\times 10^3$	6.3	6.7	6.0	S_{fit}	$\times 10^3$	6.0	5.7	5.2	5.6	4.8	5.9

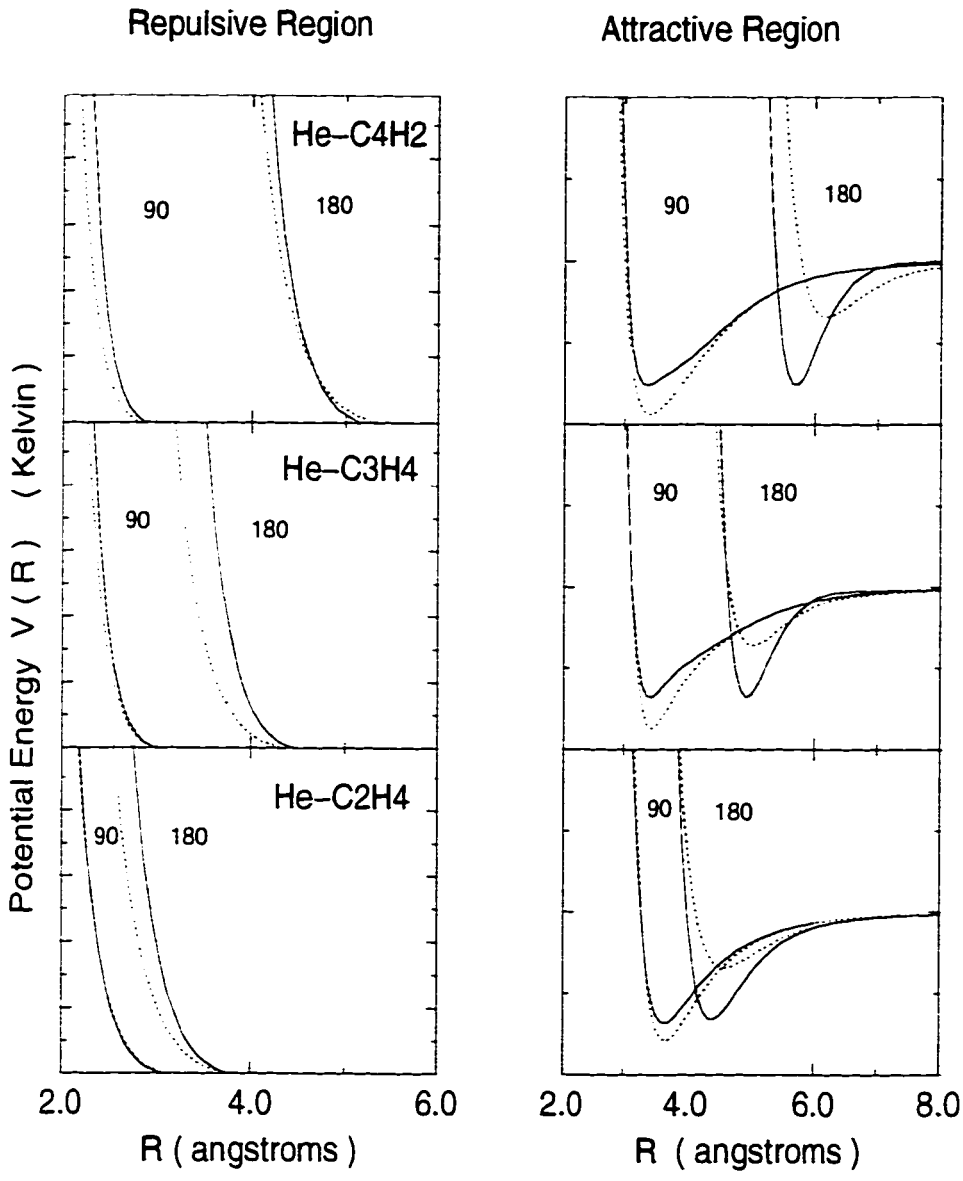

Figure 6.2: Comparison of Set A and B Barker potentials for He-X interactions in perpendicular and parallel orientations. Dashed line is set A and solid line is set B. Scale of the repulsive region is from 200 to 1200 K., and the scale of the attractive region is from -50 to 50 K.

6.1.2 Hydrogen - Ethylene, Allene, and Diacetylene Results

Similar to the He results, the H_2 total differential scattering cross sections cannot be adequately fit using spherical potential models. In contrast to the He results, no sensitivity to the potential well depth anisotropy was observed. For all the interactions only the isotropic ϵ_0 term was adequate to fit the data, while the size anisotropy was included included by expanding r_m up to the P_2 terms as in the He systems. Figure 6.3 shows the fitted total differential scattering cross sections using Barker model potentials. Once again excellent fits have been obtained to the experimental data, even for the interesting damping pattern of the H_2-C_3H_4 system.

Table 6.2 shows the determined potential parameters for the Lennard Jones and Barker potential forms. The size parameters r_{m0} and r_{m2} for the H_2 interactions are very similar to the He interaction parameters given previously. In contrast, the interaction strength has increased greatly for the H_2 results.

Comparison of the H_2-X Lennard Jones and Barker model parameters shows the size parameters are very agreeable between the two potential forms. The Lennard Jones potentials however in general have larger well depths and more steeply repulsive interactions compared to the Barker potentials, indicated more strongly correlated parameters in the rather simple Lennard Jones model.

To demonstrate the sensitivity of the scattering data to the potential energy surface anisotropy, it is interesting to compare the experimental differential scattering cross sections to results calculated using effective spherical model potentials. Figure 6.4 shows the IOS analysis results for the total differential scattering cross sections calculated using only the isotropic Barker potential model terms ϵ_0 and r_{m0} given in Table 6.2. The spherical model results are clearly not adequate for reproducing neither the damping of the scattering amplitudes nor the phase of the observed diffraction oscillations. Sufficient agreement is only qualitatively obtained for the C_2H_4 system at small angles. At larger scattering angles, the calculated results are completely out

Table 6.2: Summary of Lennard - Jones and Barker Potential Parameters for H_2 with C_2H_4, C_3H_4, and C_4H_2.

Lennard-Jones Parameters		H_2			Barker Parameters		H_2		
		C_2H_4	C_3H_4	C_4H_2			C_2H_4	C_3H_4	C_4H_2
r_{m0}	(Å)	3.91	3.90	4.08	r_{m0}	(Å)	3.97	4.01	4.10
r_{m2}	(Å)	0.52	1.05	1.67	r_{m2}	(Å)	0.56	1.13	1.59
ϵ_0	(K)	92	150	162	ϵ_0	(K)	90	132	146
ϵ_2	(K)				ϵ_2	(K)			
N		14	27	28	α		8	12	10
					A_2		9	28	24
S_{fit}	$\times 10^3$	6.3	7.8	5.0	S_{fit}	$\times 10^3$	4	7	1.7

of phase with respect to the experimental diffraction oscillations. The addition of only one additional parameter, r_{m2} gives the results presented in Figure 6.3.

The unique damping pattern of the H_2 experimental scattering cross sections can be understood by examination of the underlying, individual orientational contributions to the total IOS differential scattering cross section. Figure 6.5 shows the contributions to the total IOS scattering cross sections from the parallel and perpendicular orientations. The dotted line indicates the more strongly weighted contribution for the perpendicular orientation, while dashed line indicates the less significant contribution from the parallel orientation. The frequency of the oscillations in the two orientations indicates strongly the differences in the size of the interactions, larger interactions having much higher frequency oscillations. Considering that the total IOS differential scattering cross section is an average over all orientations, it is interesting to see that the relative frequencies and phases of the diffraction oscillations resulting from the different orientations leads directly to the unique damping pattering of the scattering cross sections. The small increase in the r_{m2} parameter for the H_2-C_3H_4

system causes a phase mismatch between the parallel and perpendicular orientations, quite clearly leading to the quenching of the second and fifth diffraction oscillations. For the H_2-C_4H_2 system, the almost complete damping of the diffraction oscillations at all angles results from the rather significant phase mismatches from the high and low frequency oscillations.

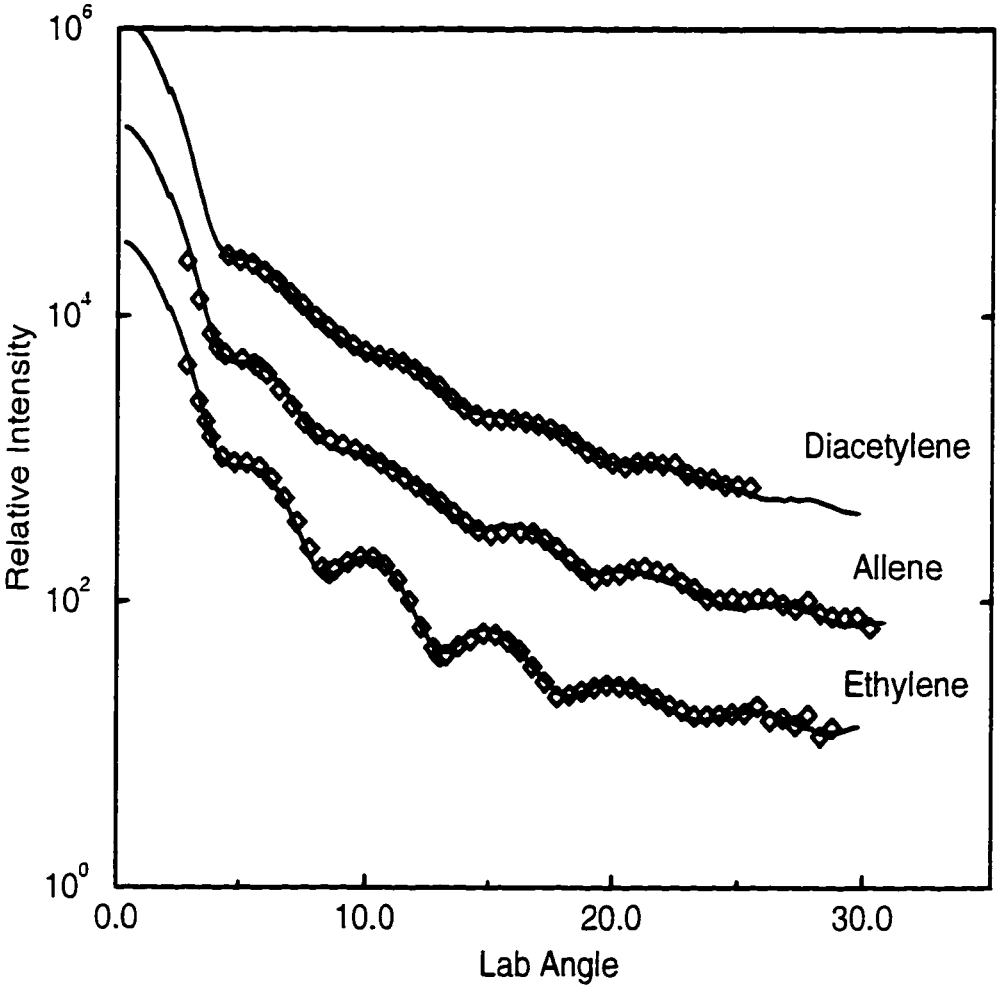

Figure 6.3: Barker Model Potential for H_2 - C_2H_4, C_3H_4, and C_4H_2. Line is best-fit from IOS analysis.

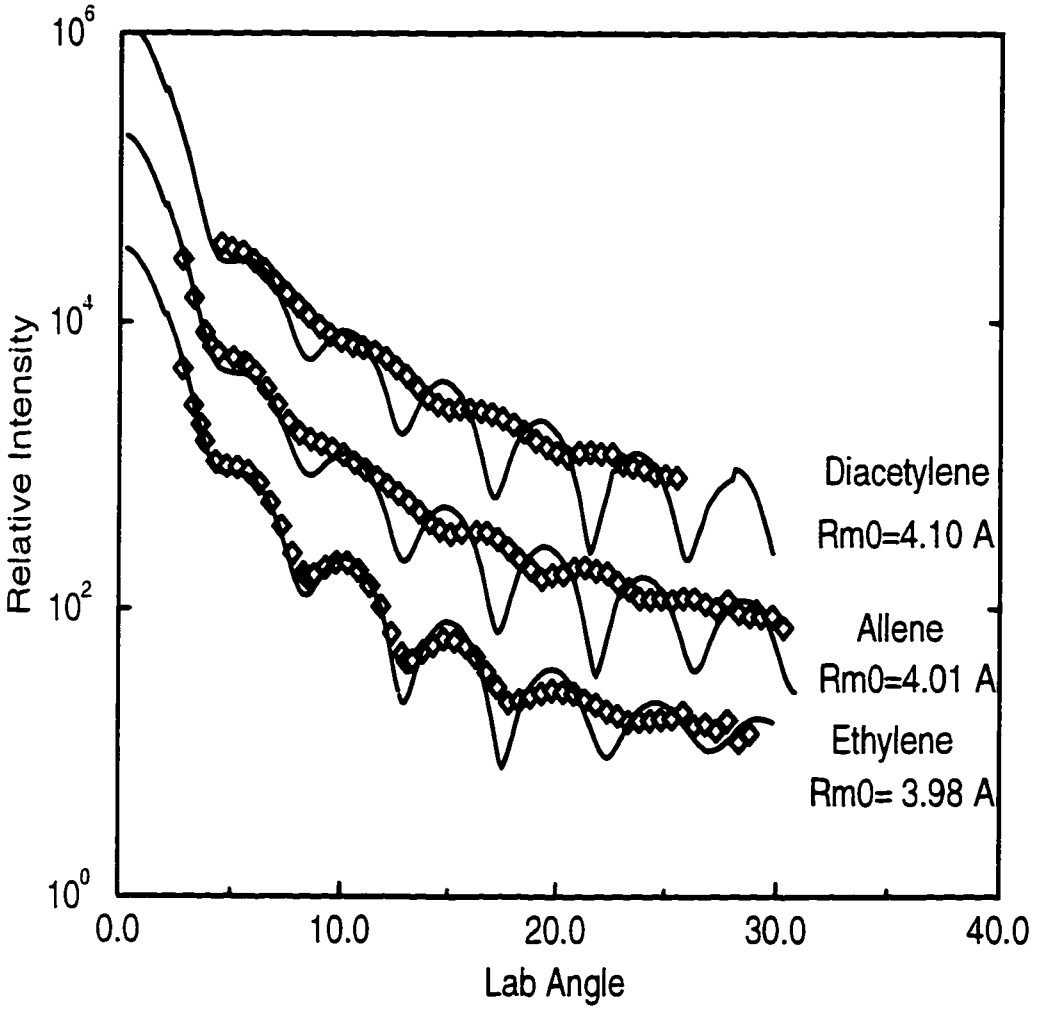

Figure 6.4: Spherical Barker Model Potential for H_2 - C_2H_4, C_3H_4, and C_4H_2 interactions. Line is best-fit from IOS analysis. Spherical model is only sufficient at very small angles, at large angles the fit curve oscillations are completely out of phase with respect to experiment.

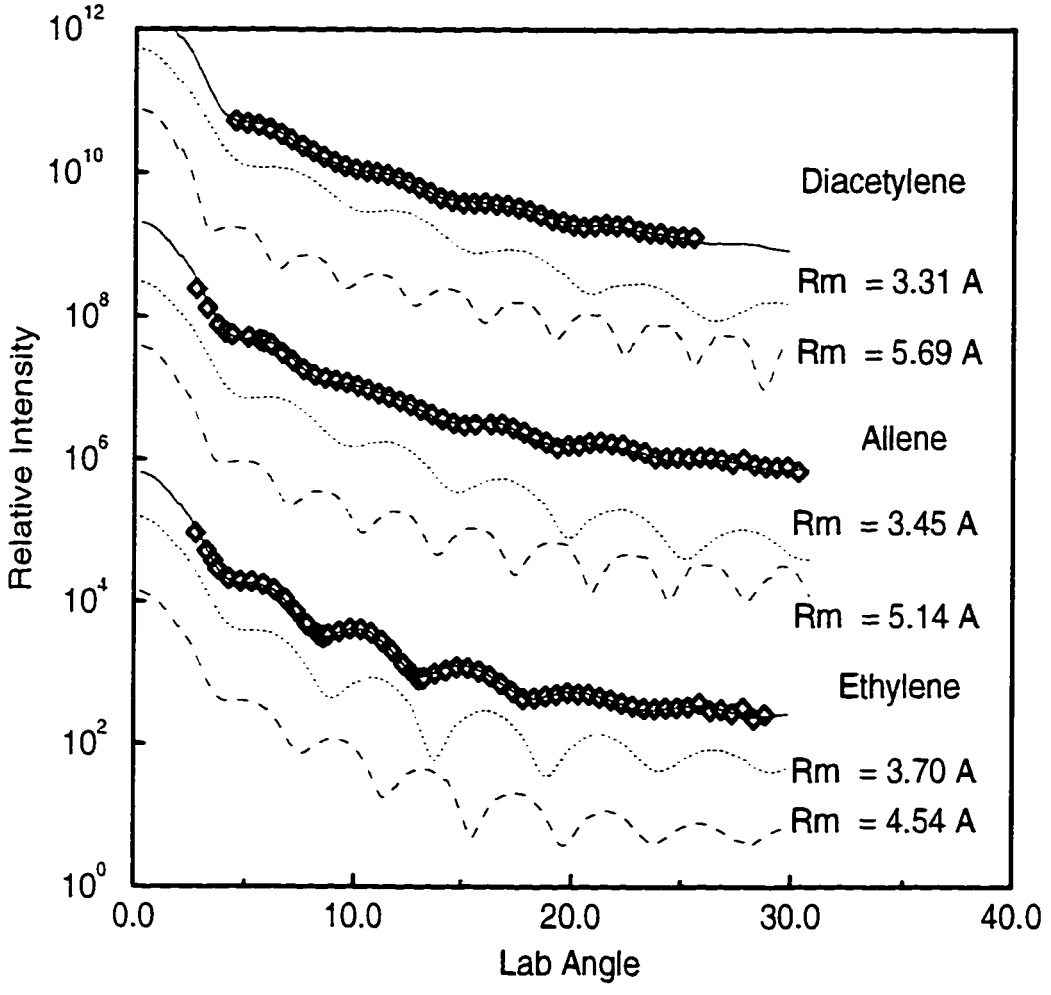

Figure 6.5: Perpendicular and parallel orientation contributions to full IOS calculation. Solid line is full IOS calculation, dotted line is perpendicular contribution, and dashed line is parallel contribution.

6.2 *Heavy Interactions* – Ne *and* Ar

The total differential scattering cross sections of the Ne and Ar - hydrocarbon systems exhibit rainbow oscillations, providing information primarily on the well depth anisotropies. However, the Ne scattering cross sections were also measured at high angular resolution revealing resolved diffraction oscillations at small angles. The Ne and Ar total differential scattering cross sections in general do not provide enough information to completely determine the interaction potentials over the full intermolecular range. For the heavy reduced mass systems the analysis was aided by considering complementary experimental data from other sources.

The intermolecular potentials for Ne and Ar - hydrocarbon molecule interactions have been investigated primarily by spectroscopic methods for the ethylene systems. Several vibrational predissociation studies have been carried out for the Ne-C_2H_4 and Ar-C_2H_4 complexes [56, 32, 61, 123, 102]. Tiller has presented a theoretical calculation of the IR spectrum of the Ne-C_2H_4 system using a qualitative atom-atom potential. High resolution rotationally-resolved near-IR spectra for the Ar-C_2H_4 [15] and Ar-C_4H_2 [16] van der Waals complexes have also been previously determined, which provide more specific structural information on the global minimum position of the complexes. The most extensive investigations on any Ar-unsaturated hydrocarbon system have concerned the prototypical Ar-C_2H_2 system, which has been studied using scattering experiments [26, 124], near IR spectroscopy [14], and *ab initio* calculations [125, 11].

6.2.1 Neon - Acetylene, Ethylene, Allene, and Diacetylene Results

The total differential scattering cross sections for the Ne-hydrocarbon systems in both the high and low angular resolution cases represent two independent experimental data sets for determining the interaction potentials. Figures 6.6 and 6.7 show the results for the low and high resolution measurements, respectively, using Barker model

potentials. In general, the high resolution experiments were used to determine the size anisotropies for the C_2H_2, C_2H_4, and C_3H_4 systems by expanding the radial minimum position up to P_2 terms. For the low resolution measurements, the potential size parameters were held fixed and only the well depth parameters were allow to vary. The high amplitude rainbow oscillations present at small scattering angles proved mostly insensitive to inclusion of well depth anisotropy in both sets of experiments.

The determined Barker potentials for the Ne-hydrocarbon interactions from both the high and low angular resolution scattering experiments are presented in Table 6.3. Comparison of the potential parameters shows clearly the consistency between two data sets, which were each determined through separate analyses using different experimental averaging procedures as calibrated by the He-Ar differential scattering measurements. The size parameters are reasonable in comparison to the previous He and H_2 interactions. The size parameters for the Ne-C_4H_2 system are mostly artificial, but based mostly on the trends observed in the results of other the determined potentials.

In general, the high resolution experiments give smaller well depth interactions, most probably as a result of insufficient smoothing of the cross sections at small angles. Systematic errors in the calculated cross sections may result at small angles due to the angular averaging procedure. This artifact is most clearly illustrated in the fitted low resolution differential scattering cross sections shown in Figure 6.6. The improper experimental averaging may give rise to the lower consistency in the A_2 potential parameters between the separate potential results.

For comparative purposes, the complete Barker interaction potentials are presented as contour surface plots in Figure 6.8. The repulsive contours for the each system are given in solid lines, while the attractive negative energy contours are given in dashed line. The density of the negative energy contours indicate clearly the larger interaction strengths for the more polarizable hydrocarbon systems, with Ne-C_4H_2 system having the broadest contours. The increased spacing between the contours

Table 6.3: Summary of Barker Potential Parameters for Ne with C_2H_2, C_2H_4, C_3H_4, and C_4H_2, for high and low resolution cases.

Barker Parameters		Ne C_2H_2		Ne C_2H_4		Ne C_3H_4		Ne C_4H_2
		low	high	low	high	low	high	
r_{m0}	(Å)	3.85	3.85	3.90	3.90	3.95	3.95	4.05
r_{m2}	(Å)	0.75	0.75	0.75	0.75	1.25	1.25	1.65
ϵ_0	(K)	80	76	86	84	100	98	105
ϵ_2	(K)							
α		12	10	12	13	12	13	12
A_2		25	17	12	14	47	45	32
S_{fit}	$\times 10^3$	4	1.7	2.1	1.0	3.1	1.1	1.5

in the perpendicular orientations indicate the broadening of the potential wells for interactions with the larger A_2 parameters. Perhaps the lack of experimental measurements on the corresponding van der Waals dimer complexes for the Ne containing systems validates these findings. Due to the isotropic nature of interactions one might expect the dimers to be very weakly bound species with large amplitude non-rigid dynamics, making accurate determination of the rotationally-resolved IR spectra quite difficult.

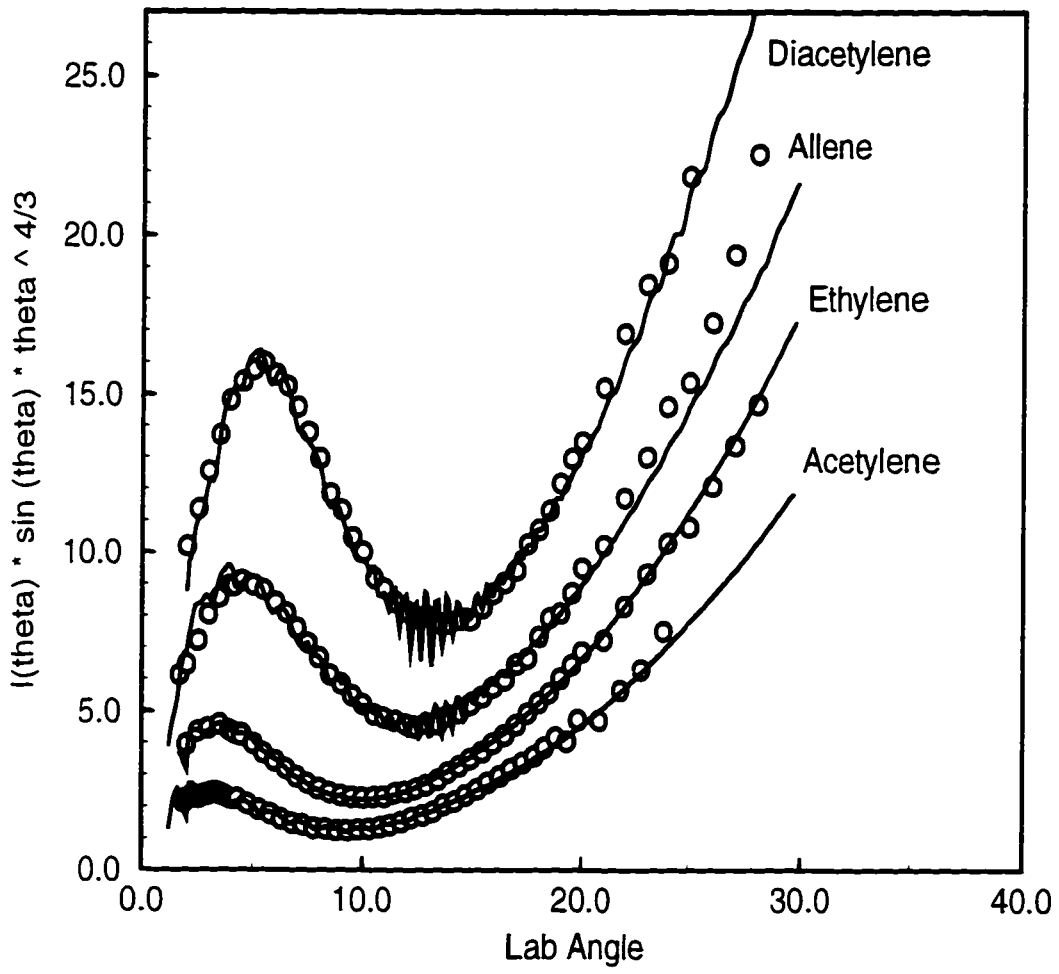

Figure 6.6: Barker potentials for Ne - C_2H_2, C_2H_4, C_3H_4, and C_4H_2 interactions at low angular resolution. Line is best-fit from IOS analysis.

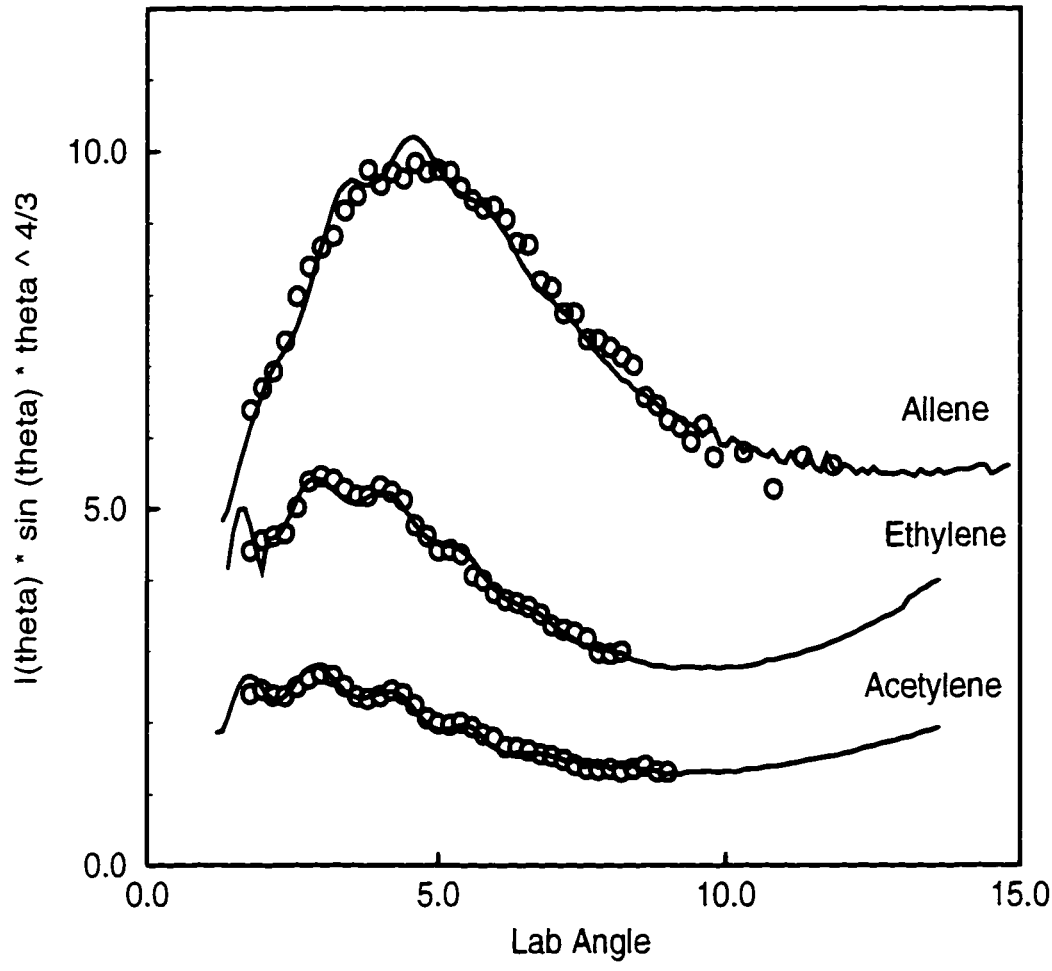

Figure 6.7: Barker Potentials Ne - C_2H_2, C_2H_4, and C_3H_4 interactions at high angular resolution. Line is best-fit from IOS analysis.

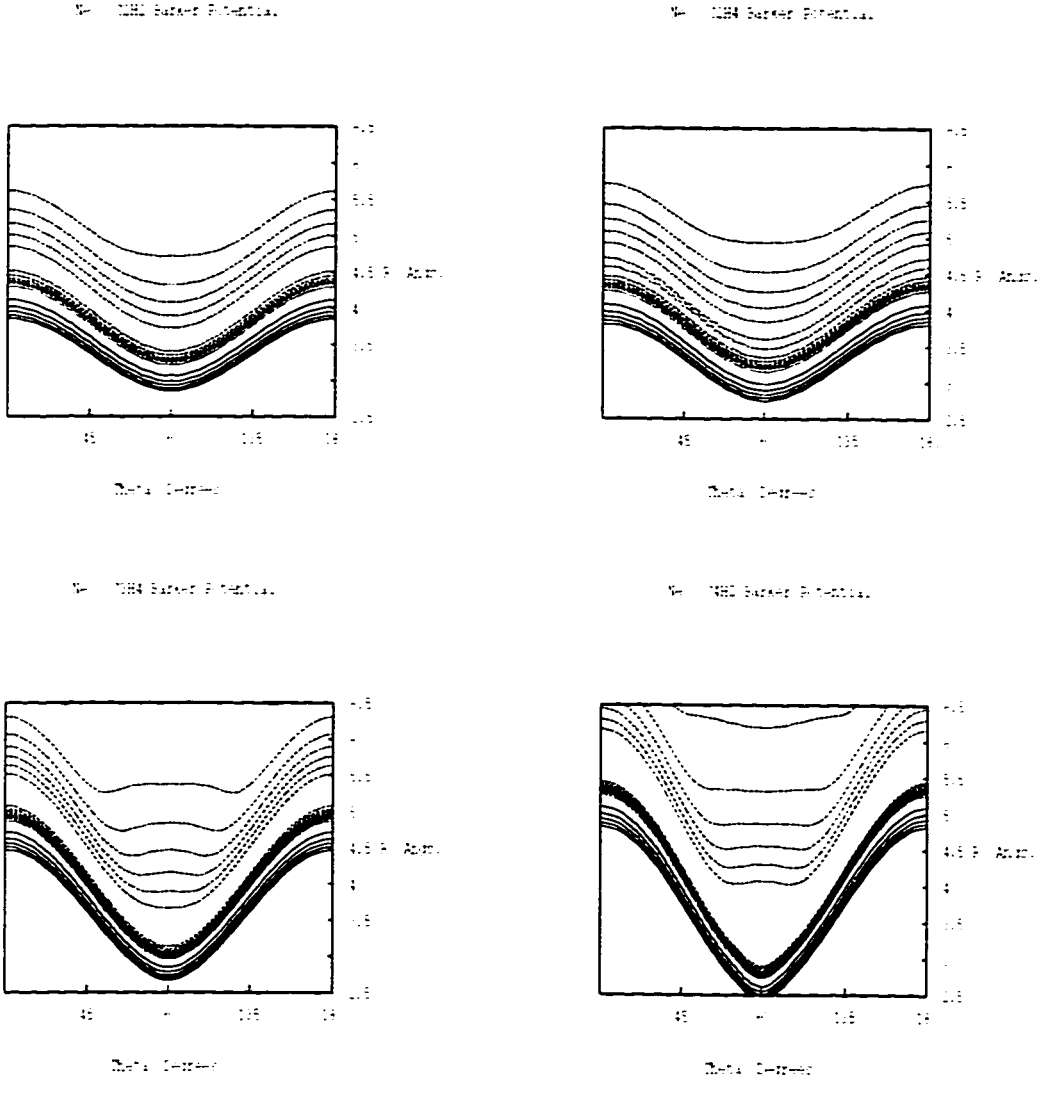

Figure 6.8: Contour Plots of Barker Potentials for Ne Interactions. Solid lines are repulsive contours 1000, 800, 600, 400, and 200 K, from innermost curve, respectively. Dotted line is the zero energy contour, and dashed lines are attractive contours -25, -37.5, -50, -62.5, -75, -87.5, and -100 K, respectively, outward.

6.2.2 Argon - Ethylene, Allene, and Diacetylene Results

The total differential scattering cross sections for the Ar-hydrocarbon systems exhibit the most severely damped rainbow oscillations of any of the interactions investigated in this thesis. The significant damping of the rainbow interactions indicates much greater shape anisotropies for Ar-hydrocarbon interactions. Unfortunately, no resolved diffraction oscillations were observed in the scattering experiments, precluding any information on the potential size anisotropies for these interactions. The high resolution spectroscopic experiments of Miller and co-workers [15, 16] were used to constrain the size parameters of the Ar-C_2H_4 and Ar-C_4H_2 interaction potentials during the fitting process. The trends observed in the determined potential data from the other systems were used to assign reasonable size parameters for the Ar-C_3H_4 system. In general several polynomial expansion terms in the well depths were required in order to obtain adequate fits to the damped rainbow oscillations in the total differential scattering cross sections. The number of expansion terms generally increased with the overall size of the hydrocarbon target molecule.

The fitted results using Barker model potentials are presented in Figure 6.9. The solid lines indicate the total scattering due to both the probe and target scattering contributions. At larger scattering angles, the calculated differential scattering contributions tend to increase more dramatically due to the more significant secondary beam contributions. Therefore the total scattering cross sections are considered to be least accurate in this angular range.

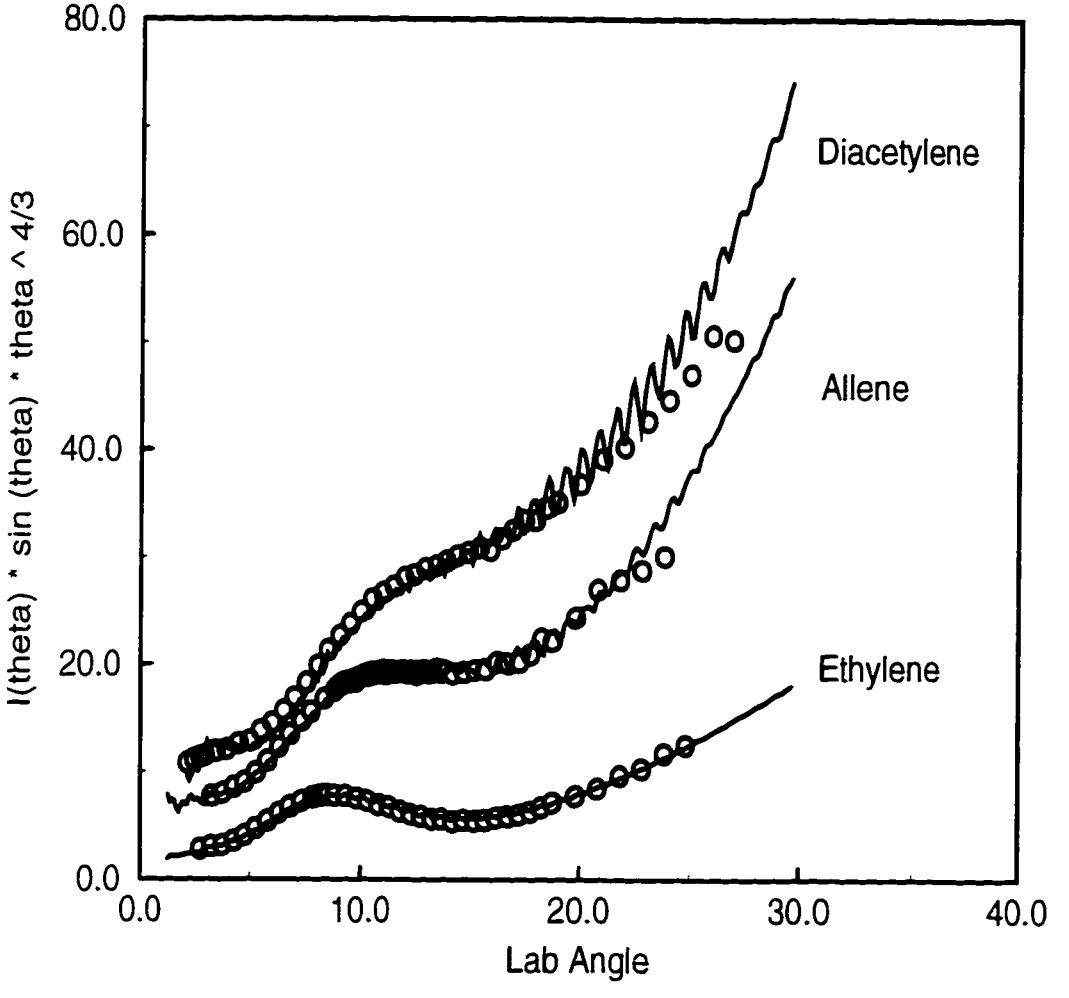

Figure 6.9: Ar Scattering from C_2H_4, C_3H_4, and C_4H_2. Line is best-fit from IOS analysis using Barker potential.

The determined potential parameters for both the Lennard-Jones and Barker models are presented in Table 6.4. The Barker potentials give significantly better agreement to the experimental data as indicated by the fitting statistic. The most obvious trend observed is the number of potential expansion terms in the well depths for larger molecular systems. The choice of the number of potential terms was determined by including additional terms in the fitting procedure in order to give the best agreement to the experimental differential scattering cross sections.

To illustrate the sensitivity of the scattering data to the potential shape anistropy, it is interesting to compare the results calculated using only the isotropic well depth ϵ_0 and the size parameters r_{m0} and r_{m2}. Figure 6.10 shows the spherical model results do not provide sufficient fits to the experimental data. In general the isotropic potential model results underestimate the scattering contributions at small angles and overestimate the scattering amplitude near the rainbow peak positions. The smaller C_2H_4 system shows qualitatively the best agreement with the isotropic well depth model results. The worst agreement is for the C_4H_2 system, which required most expansion terms in order to give good fits to the experimental data.

The damping of the rainbow oscillations can be understood by considering the individual contributions to the total IOS differential scattering cross sections. Figure 6.11 shows the individual scattering contributions for the perpendicular and parallel orientations in the total IOS differential scattering cross section. The upper dotted lines show the perpendicular orientations, while the dashed lines indicate the parallel scattering contributions. Also listed are the well depths for the two particular orientations. The solid lines indicate the full theoretical IOS differential scattering cross sections. Considering the relative weighting of the individual IOS contributions, as mentioned before in the H_2 results, it is easy to see how the individual contributions from the different orientations lead to damping of the rainbow features in the scattering data. The larger relative well depth anisotropies for the more polarizable hydrocarbon systems lead to increased damping of the rainbow oscillations at larger

scattering angles. This most clearly illustrated by the results of the Ar-C_4H_2 system.

Table 6.4: Summary of Lennard - Jones and Barker Potential Parameters for Ar with C_2H_4, C_3H_4, and C_4H_2.

Lennard-Jones Parameters		Ar C_2H_4	Ar C_3H_4	Ar C_4H_2	Barker Parameters		Ar C_2H_4	Ar C_3H_4	Ar C_4H_2
r_{m0}	(Å)	4.2	4.3	4.3	r_{m0}	(Å)	4.2	4.3	4.3
r_{m2}	(Å)	0.5	1.05	1.35	r_{m2}	(Å)	0.5	1.05	1.35
ϵ_0	(K)	210	228	284	ϵ_0	(K)	202	211	251
ϵ_2	(K)	-61	-86	-170	ϵ_2	(K)	-74	-97	-155
ϵ_4	(K)	38	97	59	ϵ_4	(K)	20	72	91
ϵ_6	(K)		-18	-24	ϵ_6	(K)		-12	-18
ϵ_8	(K)			50	ϵ_8	(K)		-14	41
N		13.5	25	22	α		9.0	11	13
					A_2		3	25	30
S_{fit}	$\times 10^3$	12	3	25	S_{fit}	$\times 10^3$	1.4	0.7	3.9

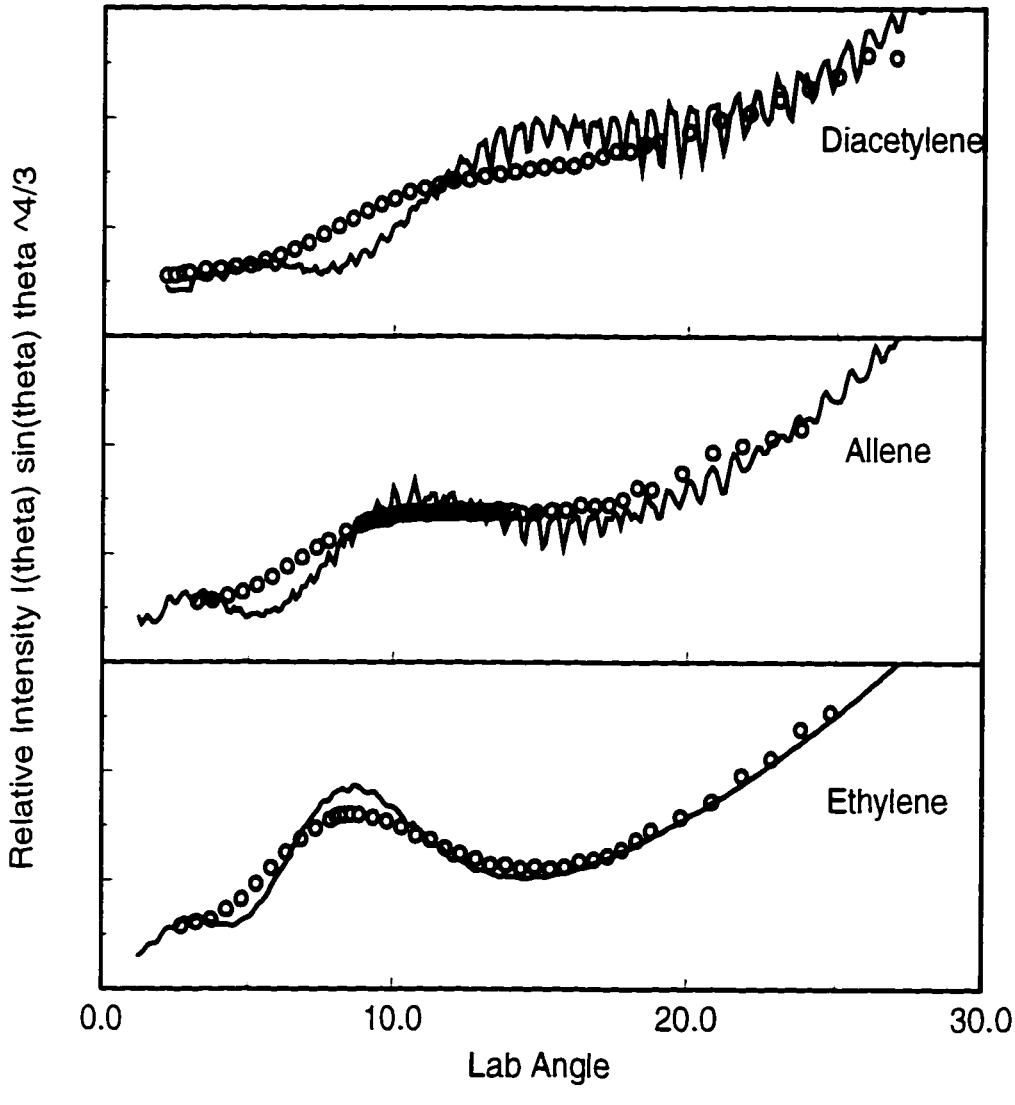

Figure 6.10: Spherical Barker Model Potential for Ar - C_2H_4, C_3H_4, and C_4H_2 interactions. Line is best-fit from IOS analysis. Spherical models can not provide adequate damping to fit experimental data.

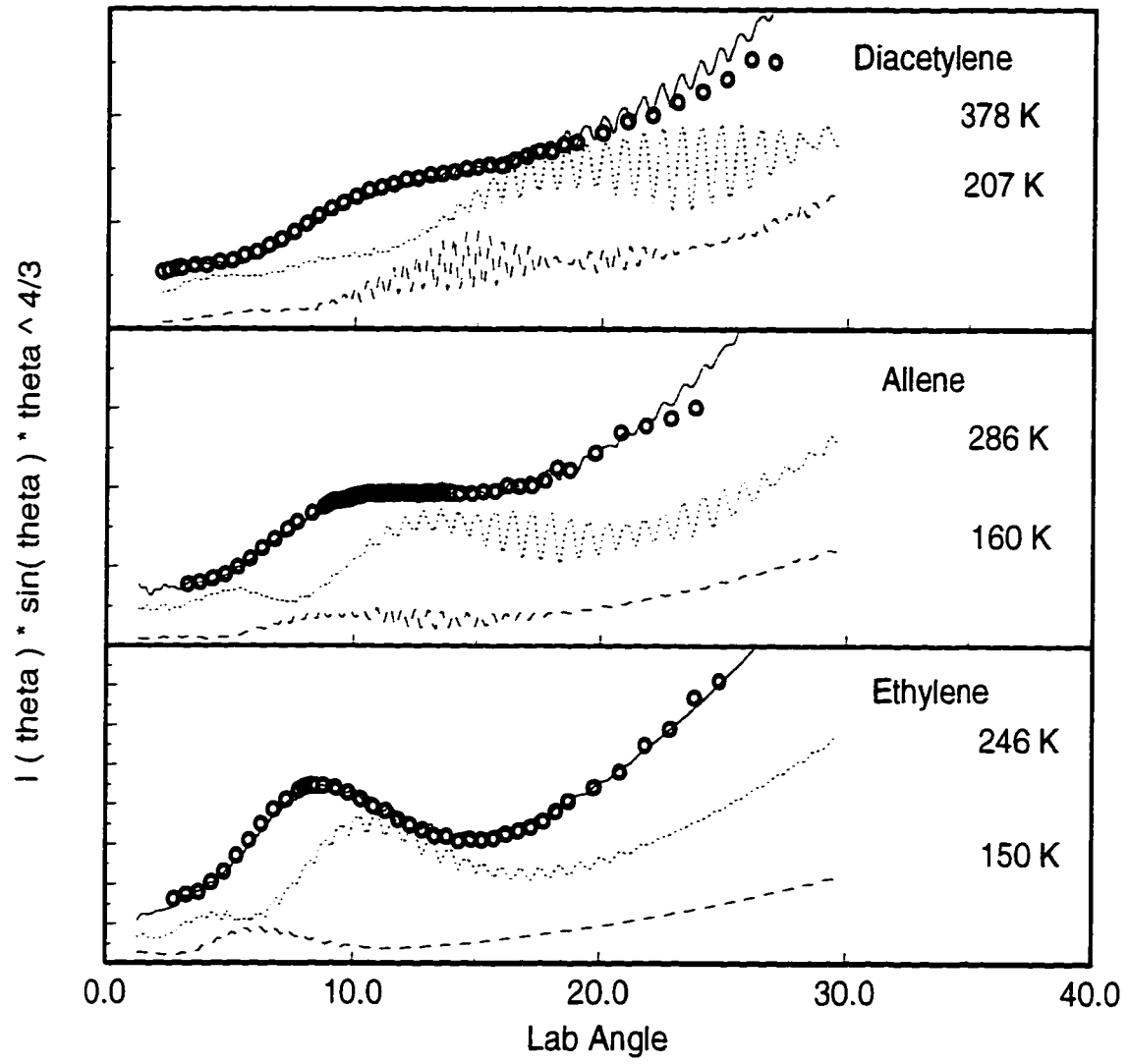

Figure 6.11: Perpendicular and parallel orientation contributions to full IOS calculation. Solid line is full IOS calculation, dotted line is perpendicular contribution, and dashed line is parallel contribution.

Due to the large number of potential expansion terms for the Ar-hydrocarbon interactions, the relative shape anisotropies are more difficult to classify. In order to more clearly show the detailed shapes of the Ar-hydrocarbon interactions, the determined Lennard Jones and Barker potentials are presented as contour plots in Figure 6.12. The left column indicates the Lennard-Jones potentials, while the Barker potentials are presented in the right column. In each column, the molecular systems are listed in descending order from C_2H_4 to C_4H_2. As before, the solid contours indicate the repulsive contours, while the dashed lines show the attractive negative energy contours. The plots clearly indicate that all the interaction potentials have more stable T-shaped geometries as indicated by the sharply localized potential contours in the perpendicular orientations. The Ar-C_4H_2 systems show the most interesting shapes as expected considering the greater number of potential terms for these systems.

Comparison of the two columns shows that the Lennard Jones potentials are more repulsive compared to the Barker models as indicated by the greater density of repulsive contour lines. Further, the attractive contour lines in the Lennard-Jones potentials appear to be more anisotropic compared to the Barker model results due to the more sharply varying contours.

To better distinguish the difference in the potential shape anisotropies between the two potential models, it is useful to compare the interaction energies for all the systems at the radial minimum positions for both potential models. Figure 6.13 shows the potential slices for the Ar-C_2H_4, C_3H_4, and C_4H_2 systems. Clearly, the two plots show that Lennard-Jones potentials are more sharply shaped as function of the orientation as well as having deeper well depths in the T-shaped configuration. The largest differences between the Lennard Jones and Barker models are at the parallel orientations.

Surprisingly, the interaction strengths shown for the perpendicular orientations in the Ar-C_2H_4 and C_4H_2 Barker model results are consistent with predictions based on *ab initio* calculations for the interaction strengths of these systems by Miller [15] and

Bemish [16]. Miller estimated the perpendicular well depth for the Ar-C_2H_4 system to be approximately 250 K., which is in excellent agreement with the Barker potential result of 246 K. For the Ar-C_4H_2 complex Bemish estimates the dissociation energy at the perpendicular orientation to be approximately 398 K., which is in reasonable agreement Barker model result of 378 K.

The high resolution spectra for the Ar-C_4H_2 system measured by Bemish also predicted a sufficiently more rigid complex in comparison to the floppy Ar-C_2H_2 and Ar-C_2H_4 complexes that were observed in earlier studies. The *ab initio* results of Bemish also predict the presence of secondary potential minima around the 60° and 140° orientations. Both the Barker and Lennard Jones models are in qualitative agreement with these predictions. More experimental investigation on the Ar-unsaturated hydrocarbon systems needs to be performed in order to better characterize the intermolecular potentials. Also, more accurate *ab initio* calculations would be helpful for refining the potential energy surface parameters in these systems, a procedure which has been successfully applied in the case of the Ar-C_2H_2 system [125].

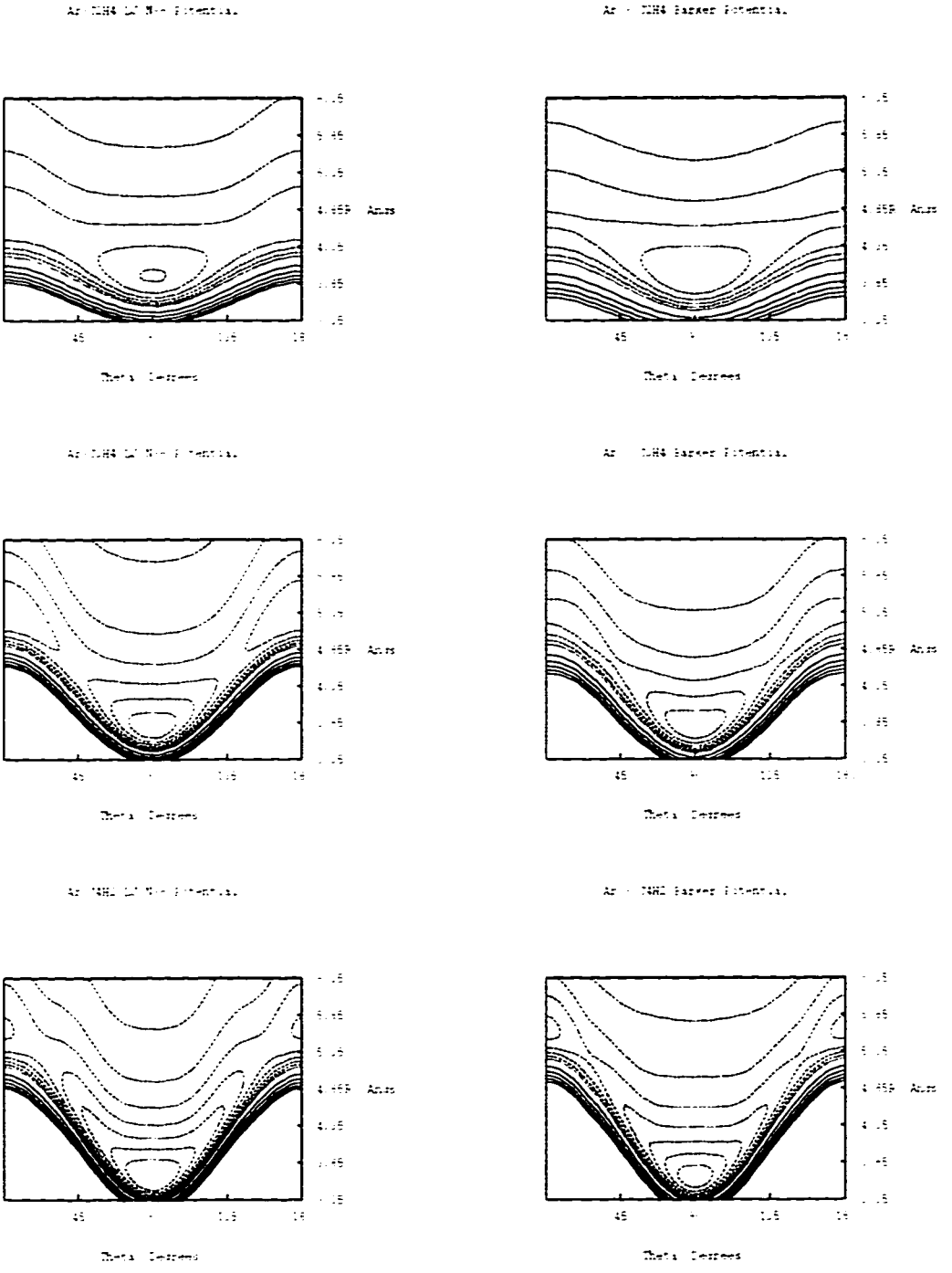

Figure 6.12: Contour Plots of Lennard Jones and Barker Potentials for Ar Interactions. Solid lines are repulsive contours 1000, 800,600,400, and 200 K, from innermost curve, respectively. Dotted line is the zero energy contour, and dashed lines are attractive contours -50, -100, -150, -200, -250, -300, -350, -400 K, respectively, outward.

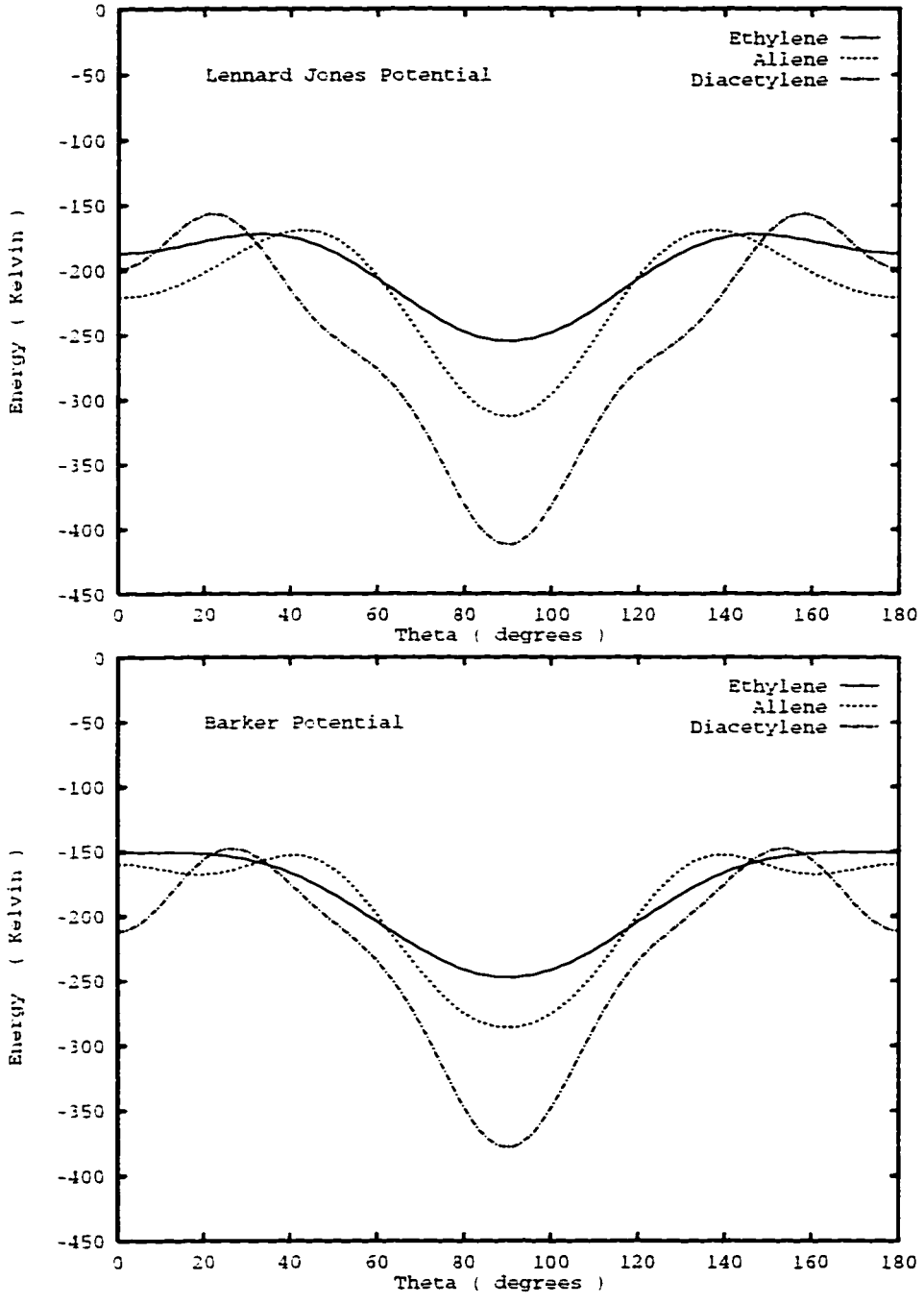

Figure 6.13: Comparison of Lennard-Jones and Barker interaction energies at r_m for Ar-X systems. Upper plot shows Lennard-Jones interactions while lower curve shows Barker interactions.

6.3 *Diatomic Interactions* – N_2, CO, *and* NO

The total differential scattering cross sections of the diatom-hydrocarbon molecule systems exhibit only single broadened, damped rainbow oscillations. The potential size parameters for these systems are estimated primarily based on the Ar-hydrocarbon systems as well as the few existing sources of experimental information obtained from the spectroscopic investigation of the complementary van der waals dimers. Further, no tests were performed to characterize the affect of neglecting of the electrostatic and inductive contributions to the total interaction potentials. As a result, the determined potential energy surfaces for the diatom-hydrocarbon systems presented here are for most part qualitative. Nevertheless, quite interesting results for the shape anisotropies of these systems have been observed in the IOS analysis of the total differential scattering cross sections.

Previously existing spectroscopic studies have been carried out for the N_2 and CO-C_2H_2 dimers, indicating that these bimolecular complexes have more stable linear configuration [13, 77, 76]. Yang has also investigated the N_2-C_2H_2 interaction potential via total differential scattering experiments finding similar consistent results to the spectroscopic measurements [127, 124]. Vibrational predissociation spectra of the NO-C_2H_4 dimer implies that the complex is T-shaped similar to the observation of the Ar-C_2H_4 results [33]. To our knowledge, no van der Waals complexes for any of the other diatom-hydrocarbon systems have been studied to date. Further, the total differential scattering cross sections have not been previously reported.

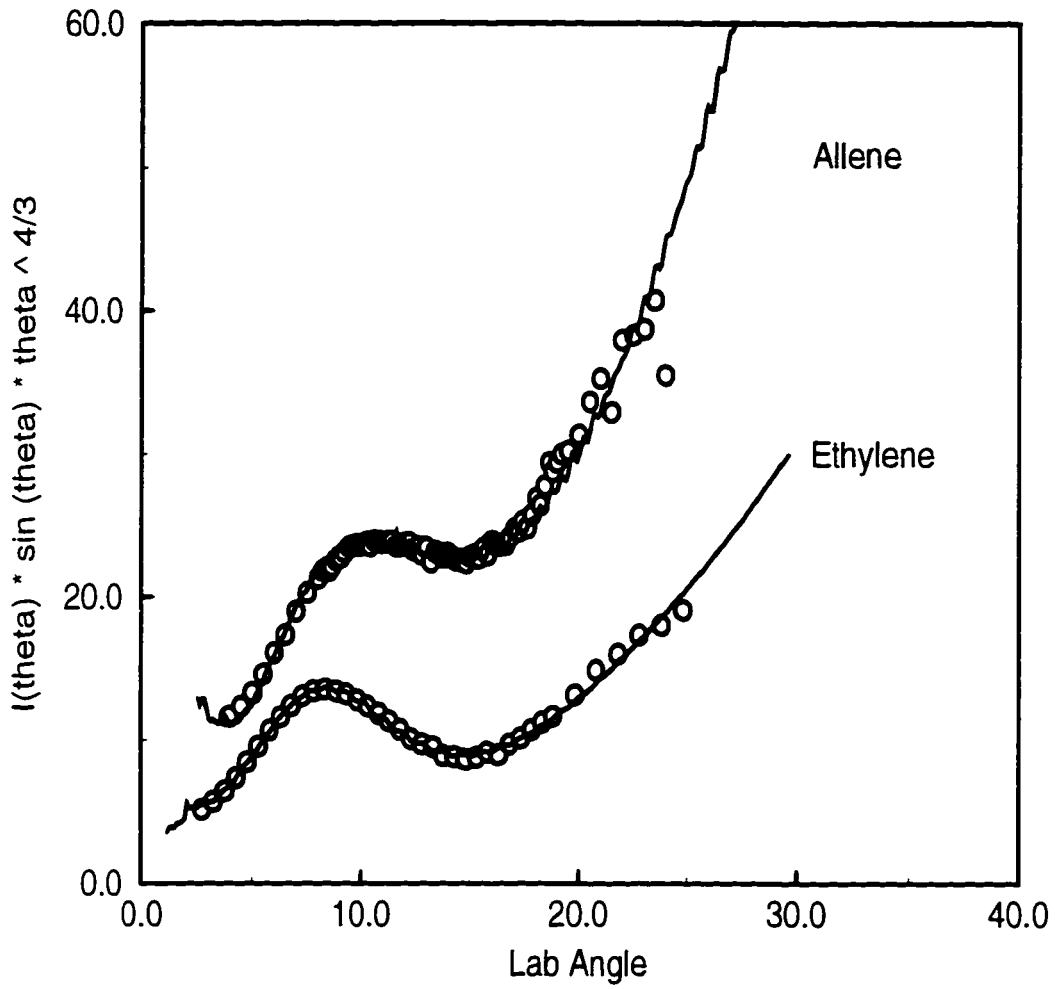

Figure 6.14: Barker Model Potential for N_2 - C_2H_2, C_2H_4, and C_3H_4. Line is best-fit from IOS analysis.

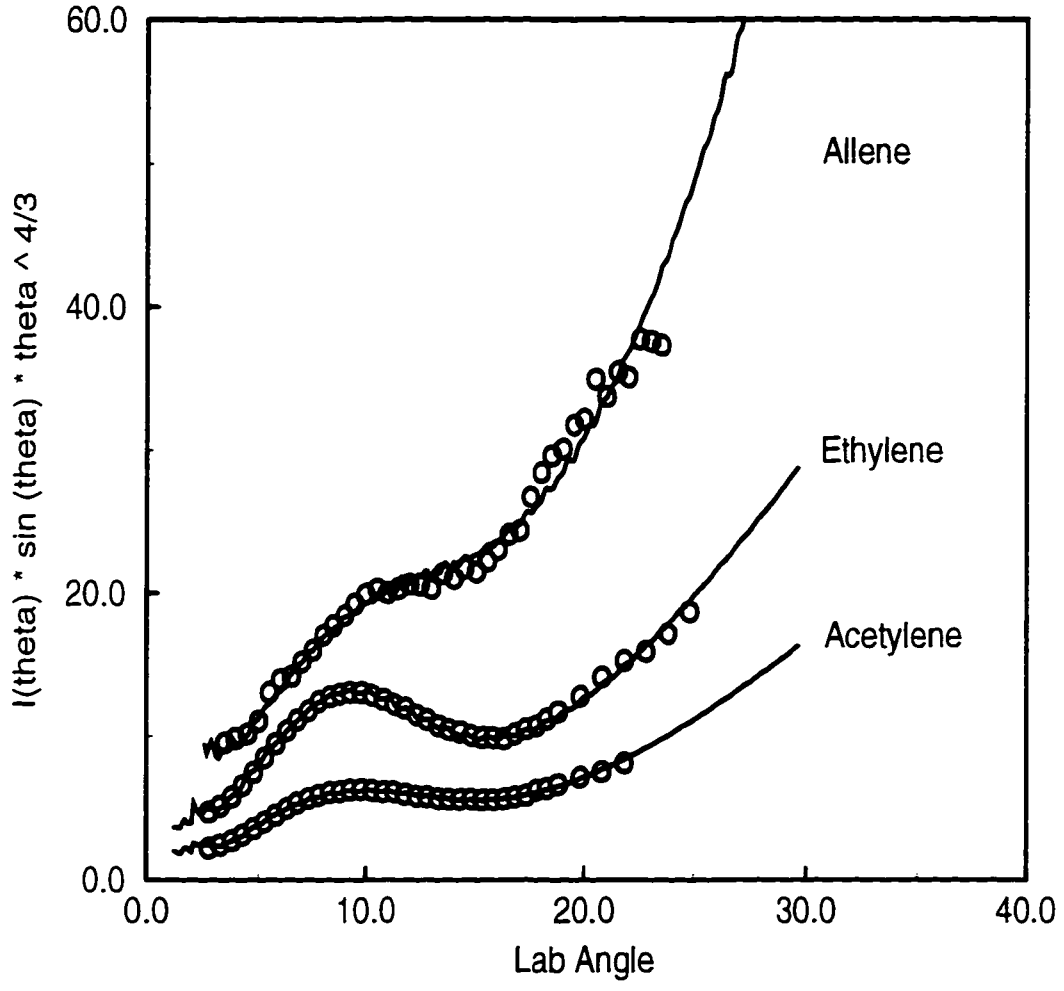

Figure 6.15: Barker Model Potential for CO - C_2H_2, C_2H_4, and C_3H_4. Line is best-fit from IOS analysis.

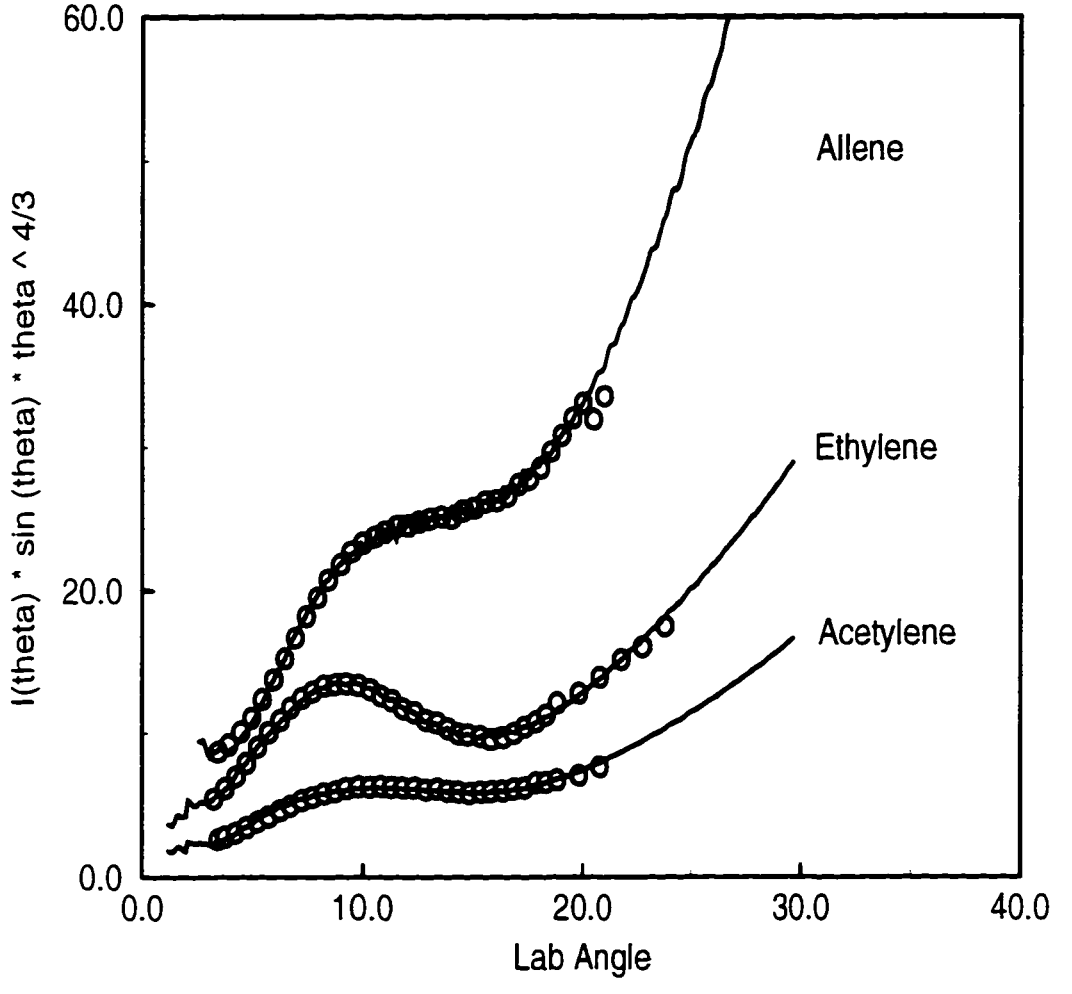

Figure 6.16: Barker Model Potential for NO - C_2H_2, C_2H_4, and C_3H_4. Line is best-fit from IOS analysis.

As mentioned before, the uniquely shaped damping of the rainbow oscillations in the total differential scattering cross sections seem to indicate that the diatom-C_2H_2 systems have more stable linear configurations, while the diatom-C_2H_4 and C_3H_4 systems have more stable T-shaped geometries. Surprisingly, this prediction is supported by the results of the fitted potential energy surfaces for these systems. Figures 6.14, 6.15, and 6.16 show the best fit IOS total differential scattering cross sections for the N_2, CO, and NO scattering systems, respectively. Reasonable fits were obtained for the majority of the experimental results, although the CO-C_3H_4 system appears to be in least agreement, mostly likely due to the poorer quality of the experimental data for this system.

The results of the determined Barker potential parameters are given in Table 6.5. In general, fewer potential parameters for the diatomic systems, in contrast to the Ar systems, were needed to obtain accurate fits to the experimental data. The most obvious difference between the determined potentials is the sign of the ϵ_2 parameters. Positive ϵ_2 values lead to more stable linear interactions, while negative ϵ_2 have more stable T-shaped geometries. So as not to bias the analysis based on the previous spectroscopic predictions, other combinations of ϵ_2 and ϵ_4 of various signs and magnitude were used. However, the no adequate fits to the experimental results could be obtained which would imply that neither the C_2H_4 nor the C_3H_4 potentials prefer more stable linear configurations. Likewise, for the C_2H_2 potentials, no accurate fits were obtained to the experimental data which would indicate the acetylene potentials prefer T-shaped geometries.

Table 6.5 shows that as the size of the hydrocarbon molecule increases, so does the magnitude of the ϵ_2 and A_2 parameters. However, the isotropic well depths ϵ_0 are similar in all sets of potential parameters. The C_2H_4 potentials have generally softer repulsive potentials compared to both the C_2H_2 and C_3H_4 systems.

Table 6.5: Summary of Barker Potential Parameters for N_2, CO, NO with C_2H_2, C_2H_4, and C_3H_4.

Barker Parameters		C_2H_2		C_2H_4			C_3H_4		
		CO	NO	N_2	CO	NO	N_2	CO	NO
$r_{m,0}$	(Å)	4.3	4.3	4.3	4.2	4.2	4.3	4.3	4.3
$r_{m,2}$	(Å)	0.7	0.7	0.7	0.5	0.5	1.0	1.1	1.1
ϵ_0	(K)	192	203	186	197	207	182	171	197
ϵ_2	(K)	68	82	-82	-89	-90	-94	-112	-105
ϵ_4	(K)			37	46	43	25	56	49
α		9.9	9.5	8.3	7.7	7.6	10.6	9.8	10
A_2		1	4	4	9	6	40	54	43
S_{fit}	$\times 10^3$	0.1	0.9	0.7	0.3	0.25	2.0	2.2	0.6

An indication of the interesting shape anisotropies for these systems is revealed in Figure 6.17. which shows the Barker potential contour plots for the CO and NO systems. The repulsive and attractive contours lines are depicted in same fashion as indicated in the previous contour plots. The left column shows the CO interactions. while the right column shows the NO results. The obvious differences in the global stabilities of the C_2H_2 systems compared to the C_2H_4 and C_3H_4 systems are easy to distinguish by the localization of the negative contours in the parallel and perpendicular regions. For all hydrocarbon cases. similar potential contours for the CO and NO interactions are observed. The weaker repulsive energies for the NO and CO-C_2H_4 interactions. compared to the results for the C_2H_2 and C_3H_4 cases. are indicated by the lower density of repulsive contours at short range. The sharper negative energy contours at perpendicular orientations for the CO and NO-C_3H_4 interactions indicate more rigid complexes for these systems compared to the smaller C_2H_4 and C_2H_2 systems. which show much broader contours that extend over greater angular range.

Similarly. the Barker potential contour plots for the N_2-C_2H_4 and C_3H_4 systems are shown in Figure 6.18. Similar features as discussed for the NO and CO interaction potentials are observed. Comparison of the well depths at the global minimum positions for all the determined diatom-hydrocarbon potentials indicate very similar interaction strengths of approximately 250-300 K. Given the quality of the experimental data. it is difficult to more accurately determine the potential shape anisotropies for these rather complex systems. Additional spectroscopic investigations of the corresponding van der Waals complexes would be invaluable for the better characterization of the size and shape anisotropies of the diatom-hydrocarbon molecule systems. Further theoretical and experimental work is necessary to substantiate the results for the multidimensional potential energy surfaces presented here.

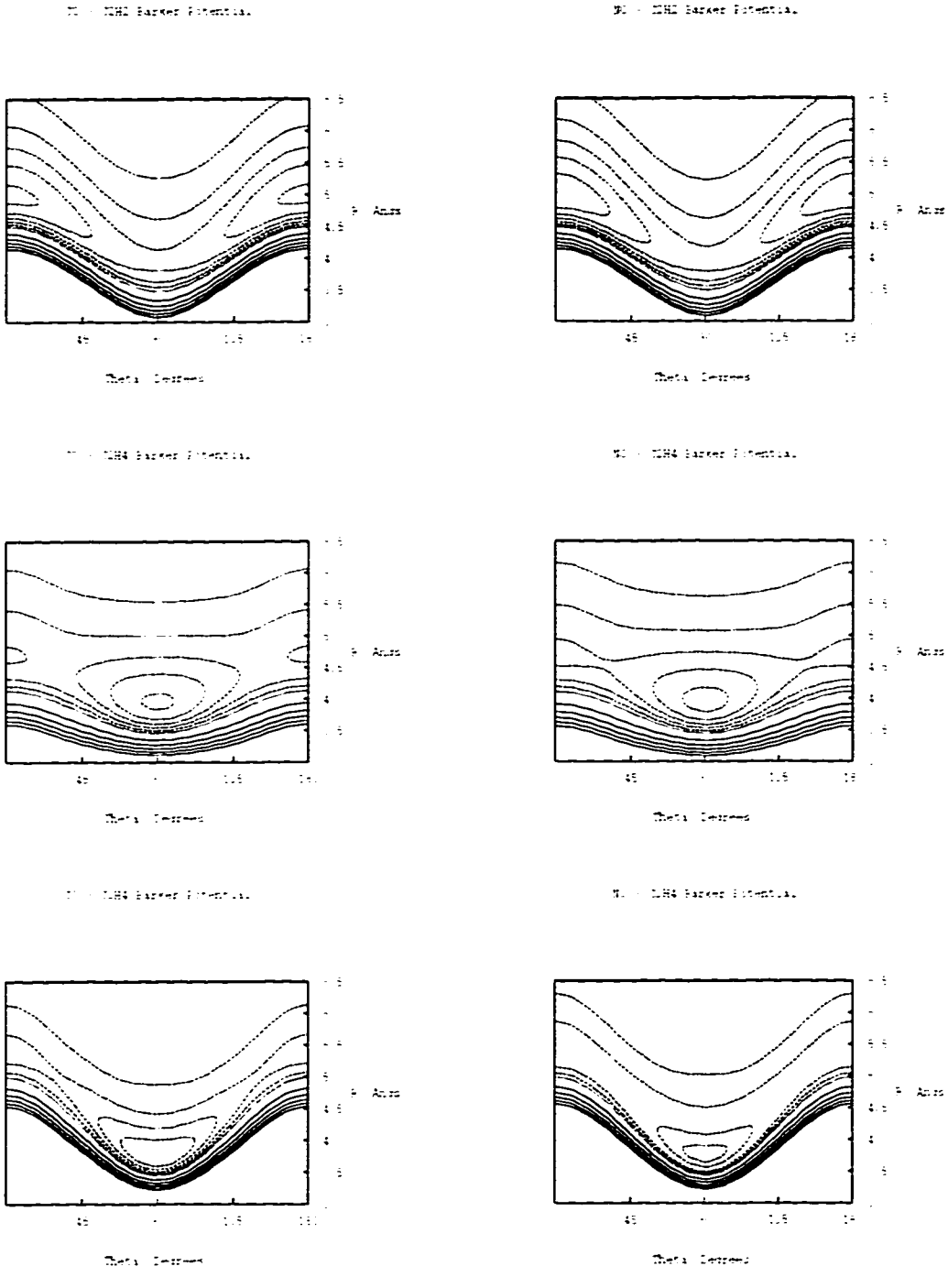

Figure 6.17: Contour Plots of Barker Potentials for CO and NOwith C_2H_2, C_2H_4, and C_3H_4 Interactions. Solid lines are repulsive contours 1000, 800, 600, 400, and 200 K, from innermost curve, respectively. Dotted line is the zero energy contour, and dashed lines are attractive contours -50, -100, -150, -200, -250, -300, -350 K, respectively, outward.

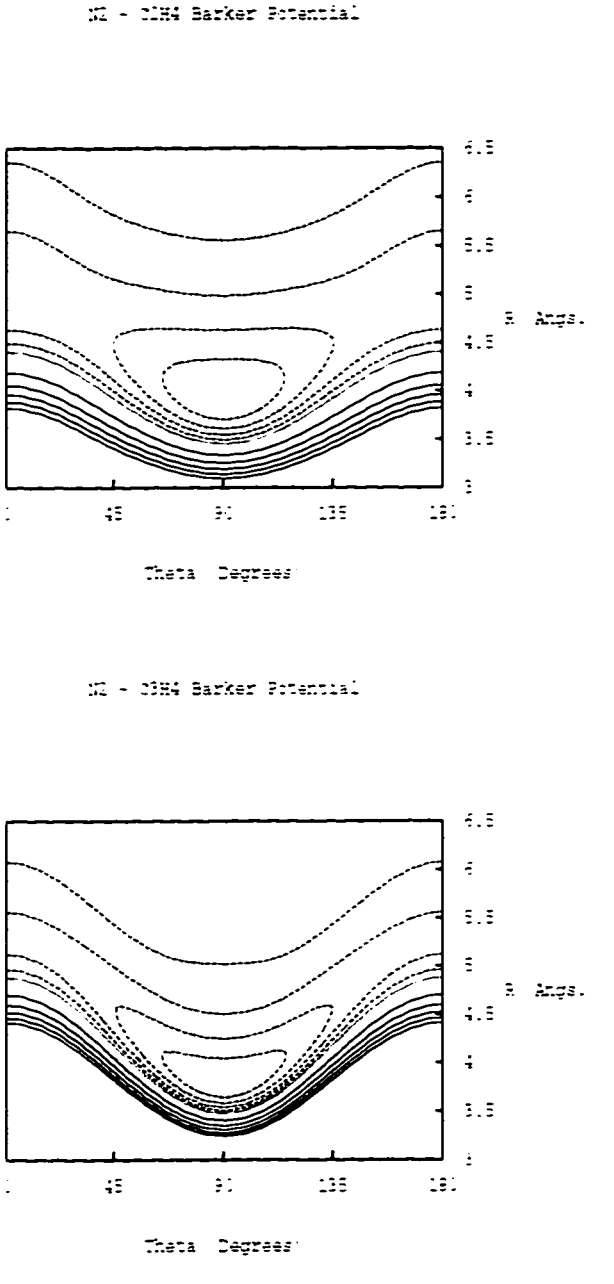

Figure 6.18: Contour Plots of Barker Potentials for N_2 with C_2H_4 and C_3H_4 interactions. Solid lines are repulsive contours 1000, 800, 600, 400, and 200 K, from innermost curve, respectively. Dotted line is zero energy contour, and dashed lines are attractive contours -50, -100, -150, -200, -250, -300, -350 K, respectively, outward.

Chapter 7

CONCLUSIONS

The intermolecular potential energy surfaces for several atmospheric gas - unsaturated hydrocarbon molecule systems were investigated using crossed molecular beam scattering experiments. The total differential scattering cross sections for He, Ne, Ar, H_2, N_2, CO, and NO with C_2H_2, C_2H_4, C_3H_4, and C_4H_2, presented Chapter 2, reveal damped quantum scattering features which provide sensitive information on the potential energy surface anisotropies for many of the systems. The light reduced mass scattering systems involving He and H_2 show primarily damped diffraction oscillations, while the heavy reduced-mass systems involving Ne, Ar, N_2, CO, and NO exhibit primarily damped rainbow oscillations. The measurement of the Ne scattering from C_2H_2, C_2H_4, and C_3H_4 under high angular resolutions showed both quantum scattering features.

To aid the analysis of the numerous scattering results, high quality TOF analysis of the molecular beams source gases was used to accurately characterize the relative collision energies of the scattering systems as well as the energy resolutions. The TOF spectra indicate qualitatively the initial rotational populations of the unsaturated hydrocarbon molecules.

To provide the basis for the theoretical calculation of the total differential scattering cross sections from an assumed model potential, the necessary classical, quantal, and semiclassical elastic scattering formulae were reviewed in Chapter 3. In particular, the infinite-order-sudden approximation to the multichannel scattering formalism for atom-symmetric top collisions was presented in order to reduce the complexity of the scattering calculations. The IOS approximation is a sufficient method for the

efficient calculation of total differential scattering cross sections from anisotropic intermolecular potentials. Essentially, the calculation reduces a one-dimensional elastic scattering problem, where the differential scattering cross section is determined by a sum over partial wave phase shifts which have been rapidly determined using the semiclassical JWKB approximation and the high energy Born approximations.

Chapter 4 described the development of anisotropic intermolecular potentials based on the analytical Lennard-Jones and Barker model potentials. The anisotropic dispersion series coefficients for the atom-molecule interactions were estimated using various molecular and atomic properties, combination rules, and a somewhat sophisticated method previously presented by Pack [93]. Based on previous presentations by Buckingham [30], the electrostatic and inductive contributions to the long range interaction potentials for the diatom-molecule systems were estimated. Using the same method as for the atom-linear molecules, the anisotropic dispersion series coefficients for the diatom-molecule systems were also determined.

A summary of the general scattering features in terms of spherical model interactions was described in Chapter 5, in order to qualitatively illustrate the presence of anisotropic features in the measured total differential scattering cross sections. Further, to distinguish between the damping in the total differential scattering data caused by the potential anisotropy rather that due to experimental resolutions, the full analysis and experimental averaging procedures were described. The calibration of the molecular beam apparatus parameters by measurement of the He-Ar differential scattering cross section gives confidence in the determined anisotropic potential energy surfaces for the more complex hydrocarbon molecular systems.

The actual determined anisotropic potentials for the light, heavy, and diatomic interactions were presented in Chapter 6. The He and H_2 systems showed significantly damped diffraction oscillations which provided sensitive measures of the potential size anisotropies and less information on teh potential shape anisotropies. Comparison of the parallel and perpendicular orientational contributions to the total IOS theoretical

calculations demonstrated the unique damping pattern of the diffraction oscillations for the larger hydrocarbon systems.

Analysis of the total differential scattering cross sections for Ne systems measured at high and low resolution showed consistent results for the determined potential energy surfaces from the two sets of scattering data. The relative size anisotropies for the Ne interaction potentials from the damped diffraction oscillations were consistent with those from the lighter He and H_2 systems. The rainbow positions proved to mostly sensitive to the isotropic well depth for these systems.

In contrast to the Ne results, the significantly damped rainbow oscillations in the Ar scattering systems were observed to provide much more detailed information on the shape anisotropies of these systems. Due to the lack of resolved diffraction oscillations, the potential size anisotropies for the Ar-C_2H_4 and Ar-C_4H_2 interactions were constrained to be in agreement with structural data obtained from high resolution near-IR spectroscopy. The Barker model potential results for well depth interactions in the T-shaped orientation for the Ar-C_2H_4 and Ar-C_4H_2 systems are in good agreement with the *ab initio* calculations of Miller [15] and Bemish [16].

The diatomic molecule-hydrocarbon scattering systems (N_2, CO, and NO with C_2H_2, C_2H_4, and C_3H_4) exhibited only damped rainbow oscillations as well. Due to the lack of the diffraction oscillations and pre-existing experimental information on these systems, the size anisotropies are more or less arbitrarily assigned. The analysis of the unique rainbow angle indicates strongly that the C_2H_2 interaction potentials have more stable linear configurations, in strict contrast to the C_2H_4 and C_3H_4 interaction potentials which show a preference for T-shaped geometries. The determined well depth interactions for the all the diatomic-hydrocarbon systems are generally the same, $\approx 250 - 300K$.

Overall the results of the IOS analysis of many total differential scattering cross sections give reasonable estimates for the anisotropic potential energy surfaces atmospheric gas-unsaturated hydrocarbon molecules. Further experimental and theoretical

investigations of the systems presented here are necessary. Both high resolution IR spectroscopy and accurate *ab initio* quantum calculations on the corresponding bimolecular dimers would provide valuable information for more accurate determination of the potential size and shape anisotropies in these systems. The validity of the IOS approximation needs to be tested against more accurate quantum scattering calculations in order to determine the role of rotationally inelastic scattering contributions in the damping of the total differential scattering cross sections. Nevertheless, the results presented here should provide the first step in the determination of multidimensional intermolecular potentials for larger molecular systems and van der Waals clusters.

BIBLIOGRAPHY

[1] American Petroleum Research Institute Research Prog. # 44. Catalog of mass spectral data. Technical report. National Bureau of Standards. 1970.

[2] M. Abramowitz and I. Stegun. *Handbook of Mathematical Functions.* Dover. New York. 1972.

[3] Y. T. Amos and J. A. Yoffee. *Chem. Phys. Lett.*, 39:53. 1976.

[4] J. B. Anderson. In P Wegner. editor. *Molecular Beams and Low Density Gas Dynamics.* Marcel Dekker. Inc.. 1974.

[5] J. B. Anderson and J. B. Fenn. *The Physics of Fluids.* 8:780. 1965.

[6] G. Arfken. *Mathematical Methods for Physicists.* Academic Press. New York. 1985.

[7] J. B. Armitage. E. R. H. Jones. and M. C. Whiting. *J. Chem. Soc.*, 9:44. 1951.

[8] A. M. Arthurs and A. Dalgarno. *Proc. Roy. Soc.*, A256:540. 1960.

[9] R. A. Aziz. In M. L. Klein. editor. *Inert Gases.* Springer-Verlag. Berlin. 1984.

[10] R. A. Aziz. P. W. Riley. U. Buck. G. Maneke. J. Schleusener. G. Scoles. and U. Valbusa. *J. Chem. Phys.*, 71:2637. 1979.

[11] J. A. Barker and M. V. Bobetic. *Phys. Rev. B.* 2:4169. 1970.

[12] J. A. Barker and A. Pompe. *Aust. J. Chem.*, 21:1683. 1968.

[13] R. D. Beck. A. G. Maki. S. Tseng. and R. O. Watts. *J. Mol. Spec.*. 158:306. 1993.

[14] R. J. Bemish. P. A. Block. L. G. Pedersen. W. Yang. and R. E. Miller. *J. Chem. Phys.*. 99:8585. 1993.

[15] R.J. Bemish. P. A. Block. L. G. Pedersen. W. Yang. and R. E. Miller. *J. Chem. Phys.*. 99:8585. 1993.

[16] R.J. Bemish. R. E. Miller. X. Yang. and G. Scoles. *J. Chem. Phys.*. 105:10171. 1996.

[17] R. B. Bernstein. *Chemical Dynamics via Molecular Beam Techniques.* Oxford University Press. New York. 1982.

[18] P. A. Block. L. G. Pedersen. and R. E. Miller. *J. Chem. Phys.*. 98:3754. 1993.

[19] M. P. Bogaard. A. D. Buckingham. R. K. Pierens. and A. H. White. *J. Chem. Soc. Faraday Trans. I.* 74:3008. 1978.

[20] A. Bondi. *J. Phys. Chem.*. 68:441. 1964.

[21] C. V. Boughton. R. E. Miller. and R. O. Watts. *Mol. Phys.*. 58:827. 1986.

[22] C.V. Boughton. *Thermal Differential Scattering of Some Weakly Important Aniostropic Molecules.* PhD thesis. Australian National University. 1987.

[23] G. W. Bryant. D. F. Eggers. and R. O. Watts. *J. Chem. Soc.. Faraday Trans. 2.* 84:1443. 1988.

[24] U. Buck. Elastic scattering ii: Differential cross sections. In G. Scoles. editor. *Atomic and Molecular Beams Methods. Vol. 1.* chapter 20. Oxford University Press. 1988.

[25] U. Buck. Inelastic scattering i: Energy loss methods. In G. Scoles, editor. *Atomic and Molecular Beams Methods. Vol. 1.* chapter 21. Oxford University Press, 1988.

[26] U. Buck, I. Ettischer, S. Schlemmer, M. Yang, P. Vohralik, and R. O. Watts. *J. Chem. Phys.*, 99:3494, 1993.

[27] U. Buck, K. H. Kohl, A. Kohlhase, M. Faubel, and V. Staemmler. *Mol. Phys.*, 55:1255, 1985.

[28] U. Buck, A. Kohlhase, T. Phillips, and D. Secrest. *Chem. Phys. Lett.*, 98:199, 1983.

[29] U. Buck, A. Kohlhase, D. Secrest, T. Phillips, G. Scoles, and F. Grein. *Mol. Phys.*, 55:1233, 1985.

[30] A. D. Buckingham. *Adv. Chem. Phys.*, 12:107, 1967.

[31] A. D. Buckingham, P. W. Fowler, and J. M. Hutson. *Chem. Rev.*, 88:963, 1988.

[32] M. P. Cassasa, D. S. Bomse, and K. C. Janda. *J. Chem. Phys.*, 74:5044, 1981.

[33] M. P. Cassasa, C. M. Western, F. G. Celii, D. E. Brinza, and K. C. Janda. *J. Chem. Phys.*, 79:3227, 1983.

[34] A. K. Chandra, S. Pal, A. C. Limaye, and S. R. Gadre. *Chem. Phys. Lett.*, 247:95, 1995.

[35] M. S. Child. *Molecular Collision Theory.* Academic Press, Loudon, 1974.

[36] R. C. Cohen and R. J. Saykally. *J. Phys. Chem.*, 94:7991, 1990.

[37] R. C. Cohen and R. J Saykally. *Annu. Rev. Phys. Chem.*, 42:369, 1991.

[38] C. Cohen-Tannoudji, B. Diu, and F. Laloe. *Quantum Mechanics*. John Wiley and Sons, Paris, 1977.

[39] D. R. Coulter, F.R. Grabiner, L. M. Casson, G. W. Flynn, and R. B. Bernstein. *J. Chem. Phys.*, 73:281, 1980.

[40] L. J. Danielson, M. Keil, and P. J. Dunlop. *J. Chem. Phys.*, 88:4218, 1988.

[41] L. J. Danielson, K. M. Mcleod, and M. Keil. *J. Chem. Phys.*, 87:239, 1987.

[42] G. O. Este, D. G. Knight, G. Scoles, U Valbusa, and F. Grein. *J. Phys. Chem.*, 87:2772, 1983.

[43] D. Flower. *Molecular Collisons in the Intersellar Medium*, volume 17 of *Cambridge Astrophysical Series*. Cambridge University Press, Cambridge, 1990.

[44] M. A. D. Fluendy and K. P. Lawley. *Chemical Applications of Molecular Beam Scattering*. Chapman and Hall, London, 1973.

[45] W. H. Flygare. *Molecular Structure and Dynamics*. Prentice Hall, New Jersey, 1978.

[46] P. W. Fowler and G. H. F. Diercksen. *Chem. Phys. Lett.*, 167:105, 1990.

[47] R. J. Gallager and J. B. Fenn. *J. Chem. Phys.*, 60:3492, 1974.

[48] T. C. Germann, S. L. Tschopp, and H. S. Gutowsky. *J. Chem. Phys.*, 97:1619, 1992.

[49] R. Goldflam, S. Green, and D. J. Kouri. *J. Chem. Phys.*, 67:4149, 1977.

[50] H. Goldstein. *Classical Mechanics*. Addison-Wesley Publishing Co., Reading, 1950.

[51] C. G. Gray and K. E. Gubbins. *Theory of Molecular Fluids*, volume 1. Oxford University Press, Oxford, 1984.

[52] S. Green. *J. Chem. Phys.*, 64:3463, 1976.

[53] S. Green. *J. Chem. Phys.*, 70:816, 1979.

[54] S. Green. *J. Chem. Phys.*, 103:1035, 1995.

[55] H. Haberland, U. Buck, and M. Tolle. *Rev. Sci. Instrum.*, 56:1712, 1985.

[56] S. R. Hair, J. A. Beswick, and K. C. Janda. *J. Chem. Phys.*, 89:3970.

[57] R. K. B. Helbing. *J. Chem. Phys.*, 48:472, 1968.

[58] E. R. Herbst. Interstellar molecules. *Ann. Rev. Phys. Chem.*, 199?

[59] J. O. Hirschfelder, C. F. Curtiss, and R. B. Bird. *Molecular Theory of Gases and Liquids*. Wiley, New York, 1954.

[60] J. M. Huston. *An Introduction to the Dynamics of van der Waals Molecules*, volume 1A of *Advances in Molecular Vibrations and Collision Dynamics*, chapter 1. Jai Press, Inc., London, 1991.

[61] J. M. Huston, D. C. Clary, and J. A. Beswick. *J. Chem. Phys.*, 81:4474, 1984.

[62] J. M. Hutson. *Annu. Rev. Phys. Chem.*, 41:123, 1990.

[63] A. V. Jones. Infra-red and raman spectra of diacetylene. *Proc. Roy. Soc.*, 211:285, 1952.

[64] I. G. Kaplan. *Theory of Molecular Interactions*. volume 42 of *Studies in Physical and Theoretical Chemistry*. Elsevier Science Publishers. Inc.. New York. 1986.

[65] M. Keil. J. T. Slankas. and A. Kuppermann. *J. Chem. Phys.*. 70:541. 1979.

[66] D. J. Kouri. Rotational excitation ii: Approximation methods. In R. B. Bernstein. editor. *Atom-Molecule Collision Theory*. chapter 9. Plenum Press. New York. 1979.

[67] A. Kupperman. R. J. Gordon. and M. J. Coggiola. *Faraday Discuss. Chem. Soc.*. 55:145. 1973.

[68] IR Laboratories. *Cryogenic Bolometer Instruction Manual*. 1989.

[69] J. D. Lambert. *Vibrational and Rotational Relaxation in Gases*. Oxford University Press. Oxford. 1977.

[70] L. D. Landau and E. M. Lifshitz. *Mechanics*. Pergamon Press. Oxford. 1976.

[71] L. D. Landau and E. M. Lifshitz. *Quantum Mechanics*. Pergamon Press. Oxford. 1976.

[72] D. Van Lerberghe. I. J. Wright. and J. L. Duncan. *J. Mol. Spec.*. 42:251. 1972.

[73] R. D. Levine and R. B. Bernstein. *Molecular Reaction Dynamics*. Oxford University Press. Oxford. 1974.

[74] G. C. Maitland. M. Rigby. E. B. Smith. and W. A. Wakeham. *Intermolecular Forces: Their Origin and Determination*. Oxford University Press. Oxford. 1981.

[75] A. G. Maki. A. S. Pine. and M. Dang-Nhu. *J. Mol. Spec.*. 112:459. 112.

[76] M. D. Marshall, D. G. Prichard, and J. S. Muenter. *J. Chem. Phys.*, 90:6049, 1989.

[77] K. Matsumura, F. J. Lovas, and R. D. Suenram. *J. Mol. Spec.*, 144:123, 1990.

[78] P. McGuire and J. Kouri. *J. Chem. Phys.*, 60:2488, 1974.

[79] D. McNaughton and D. N. Bruget. *J. Mol. Struct.*, 273:11, 1992.

[80] D. A. McQuarrie. *Statistical Mechanics*. HarperCollins Publishers, Inc., New York, 1976.

[81] A. Messiah. *Quantum Mechanics*. John Wiley and Sons, New York, 1966.

[82] D. R. Miller. Free jet sources. In G. Scoles, editor, *Atomic and Molecular Beams Methods*, *Vol. 1*, chapter 2. Oxford University Press, 1988.

[83] R. E. Miller. *J. Phys. Chem.*, 90:3301, 1986.

[84] R. E. Miller. *Acc. Chem. Res.*, 23:10, 1990.

[85] K. D. Moller. *Optics*. University Science Books, 1988.

[86] R. Moszynski, P.E.S. Wormer, and A. van der Avoird. *J. Chem. Phys.*, 102:8385, 1995.

[87] F. Mulder, G. F. Thomas, and W. J. Meath. *Mol. Phys.*, 41:249, 1980.

[88] J. N. Murrell and S. D. Bosanac. *Introduction to the Theory of Atomic and Molecular Collisions*. John Wiley and Sons, New York, 1989.

[89] D. J. Nesbitt. *Chem. Rev.*, 88:843, 1988.

[90] D. J. Nesbitt. *Annu. Rev. Phys. Chem.*, 45:367, 1994.

[91] D. J. Nesbitt, J. W. Nibler, A. Schiffman, W. B. Chapman, and J. M. Hutson. *J. Chem. Phys.*, 98:9513, 1993.

[92] G. C. Nielson, G. A. Parker, and R. T. Pack. *J. Chem. Phys.*, 64:2055, 1976.

[93] R. T. Pack. *J. Chem. Phys.*, 61:2091, 1974.

[94] R. T. Pack. *J. Chem. Phys.*, 60:633, 1974.

[95] R. T. Pack. *J. Chem. Phys.*, 64:1659, 1976.

[96] R. T. Pack. *Chem. Phys. Lett.*, 55:197, 1978.

[97] R. T. Pack, J. J. Valentini, and J. B. Cross. *J. Chem. Phys.*, 77:5486, 1982.

[98] K. F. Palmer, M. E. Mickelson, and R. Naharahi. *J. Mol. Spect.*, 44:131, 1972.

[99] G. A. Parker, M. Keil, and A. Kuppermann. *J. Chem. Phys.*, 78:1145, 1983.

[100] G. A. Parker and R. T. Pack. *J. Chem. Phys.*, 68:1585, 1978.

[101] H. Pauly. Elastic scattering cross sections i: Spherical potentials. In R. B. Bernstein, editor, *Atom-Molecule Collision Theory*, chapter 4. Plenum Press, New York, 1979.

[102] A. C. Peet, D. C. Clary, and J. M. Hutson. *J. Chem. Soc., Faraday Trans. 2*, 83:1719, 1987.

[103] A. J. Pertsin and A. I. Kitaigorodsky. *Atom-Atom Potential Method*, volume 43 of *Springer Series in Chemical Physics*. Springer-Verlag, Berlin, 1987.

[104] W. H. Press, B. P. Flannery, S. A. Teukolsky, and W. T. Vetterling. *Numerical Recipes: The Art of Scientific Computing.* Cambridge University Press, New York, 1989.

[105] Editor R. C. Weast. *CRC Handbook of Chemistry and Physics.* CRC Press, Inc., 1989.

[106] R. J. Saykally and G. A. Blake. *Science*, 259:1570, 1993.

[107] A. Schiffman, W. B. Chapman, and D. J. Nesbitt. *J. Phys. Chem.*, 100:3402, 1996.

[108] A. Schiffmann and D. W. Chandler. *Inter. Rev. Phys. Chem.*, 14:371, 1995.

[109] B. Schulz and P. Botschwina. *Chem. Phys. Lett.*, 243:378, 1995.

[110] H. F. Schuster and G. M. Coppola. *Allenes in Organic Synthesis.* Wiley, New York, 1984.

[111] D. Secrest. Rotational excitation i: The quantal treatment. In R. B. Bernstein, editor, *Atom-Molecule Collision Theory*, chapter 8. Plenum Press, 1979.

[112] T. Shimanouchi. Tables of vibrational frequencies consolidated vol. 1. Technical report, National Bureau of Standards, 1972.

[113] M. F. Shostakovskii. *The Chemistry of Diacetylenes.* Wiley, New York, 1974.

[114] J. T. Slankas, M. Keil, and A. Kuppermann. *J. Chem. Phys.*, 70:1482, 1979.

[115] B. Smith and R. Srivastava. *Thermodynamic Data for Pure Compounds: Part A-Hydrocarbons and Ketenes.* Elsevier, New York, 1986.

[116] Inc. SRS. *Application Note 3: About Lock-in Amplifiers.* Stanford Research Systems. Inc.

[117] D. E. Stogryn and A. P. Stogryn. *Mol. Phys.*, 11:371. 1966.

[118] A. J. Stone. *The Theory of Intermolecular Forces.* Oxford University Press. Oxford. 1996.

[119] A. Szabo and N. S. Ostlund. *Modern Quantum Chemistry.* McGraw-Hill. 1989.

[120] A. R. Tiller. A. C. Peet. and D. C. Clary. *J. Chem. Phys.*, 91:1079. 1989.

[121] P. F. Vohralik. *Structure and Dynamics from Molecular Beam Experiments.* PhD thesis. Australian National University. 1986.

[122] M. J. Weida. J.M. Sperhac. D. J. Nesbitt. and J. M. Hutson. *J. Chem. Phys.*, 101:8351. 1994.

[123] C. M. Western. M. P. Casassa. and K. C. Janda. *J. Chem. Phys.*, 80:4781. 1984.

[124] M. Yang. *Experimental and Theoretical Studies of Atom-Molecule Scattering.* PhD thesis. U. of Washington. 1994.

[125] M. Yang. M. H. Alexander. H. Werner. and R.J. Bemish. *J. Chem. Phys.*, 105:10462. 1996.

[126] M. Yang and R. O. Watts. *J. Chem. Phys.*, 100:3582. 1994.

[127] M. Yang and R. O. Watts. *J. Chem. Phys.*, 101:8784. 1994.

[128] X. Yang. R. Z. Pearson. K. K. Lehmann. and G. Scoles. *J. Chem. Phys.*, 105:10725. 1996.

[129] L. Zandee and J. Reuss. *Chemical Physics*. 26:327. 1977.

[130] L. Zandee and J. Reuss. *Chemical Physics*. 26:345. 1977.

[131] L. Zandee. J. Verbene. and J. Reuss. *Chemical Physics*. 26:1. 1977.

VITA

Kip Patrick Stevenson was born May 9, 1966 in Walla Walla, Washington. He graduated from Walla Walla High School 1985 and later attended the University of Puget Sound, graduating with a B.S. in Chemistry and minors in Mathematics and Economics in 1989. In the Fall of 1989, Kip entered graduate school in Bioengineering at the University of Washington, and later transferred into the Department of Chemistry in the Fall of 1991, after discovering that his interests concerned more fundamental science. Kip recieved his Ph.D.in Physical Chemistry from the University of Washington in 1997. He has accepted a post-doctoral position in the Chemical Structure and Dynamics Group of the Environmental Molecular Science Laboratory under the Pacific Northwest National Labs in Richland, Washington.